Fluorescence Lifetime Single Molecule Localisation Microscopy

Dissertation
for the award of the degree
"Doctor rerum naturalium"
of the Georg-August-Universität Göttingen

within the doctoral program
Physics of Biological and Complex Systems
of the Göttingen Graduate School of Neurosciences,
Biophysics, and Molecular Biosciences (GGNB)
of the Georg-August-University School of Science (GAUSS)

submitted by
Jan Christoph Thiele
from Hamburg, Germany

Georg-August-Universität
Göttingen, December 2020

THESIS ADVISORY COMMITTEE:

Prof. Dr. Jörg Enderlein (Referee)
III. Physikalisches Institut – Biophysik
Georg-August-Universität Göttingen

Prof. Dr. Thomas P. Burg (Co-referee)
Department of Electrical Engineering and Information Technology
Technical University of Darmstadt

Prof. Dr. Marcus Müller
Institute for Theoretical Physics
Georg-August-Universität Göttingen

FURTHER MEMBERS OF THE EXAMINATION BOARD:

Dr. Sarah Adio
Göttingen Center for Molecular Biology
Georg-August-Universität Göttingen

Prof. Dr. Timo Betz
III. Physikalisches Institut – Biophysik
Georg-August-Universität Göttingen

Dr. Andreas Neef
Bernstein Center for Computional Neuroscience Göttingen
Max Planck Institute for Dynamics and Self-Organization

Date of oral examination: 19th February 2021.

AFFIDAVIT

Hereby, I declare that the presented thesis has been written independently and with no other sources and aids than quoted.
Parts of this thesis and some figures have been published in:

> Jan Christoph Thiele, Dominic A. Helmerich, Nazar Oleksiievets, Roman Tsukanov, Eugenia Butkevich, Markus Sauer, Oleksii Nevskyi, and Jörg Enderlein, 'Confocal Fluorescence-Lifetime Single-Molecule Localization Microscopy', *ACS Nano* 2020, 14, 10, pp. 14190–14200. 10.1021/acsnano.0c07322.
>
> Nazar Oleksiievets,* Jan Christoph Thiele,* André Weber, Ingo Gregor, Oleksii Nevskyi, Sebastian Isbaner, Roman Tsukanov, Jörg Enderlein, 'Wide-Field Fluorescence Lifetime Imaging of Single Molecules', *J. Phys. Chem. A* 2020, 124, 17, pp. 3494–3500. 10.1021/acs.jpca.0c01513
>
> Narain Karedla, Jan Christoph Thiele, Ingo Gregor, and Jörg Enderlein, 'Efficient solver for a special class of convection-diffusion problems', *Physics of Fluids* 2019, 31, 023606. 10.1063/1.5079965
>
> Jan Christoph Thiele, Ingo Gregor, Narain Karedla, and Jörg Enderlein, 'Efficient modeling of three-dimensional convection-diffusion problems in stationary flows', *Physics of Fluids* 2020, 32, 112015. 10.1063/5.0024190

∗ These authors contributed equally to this work.

Göttingen, December 2020.

ABSTRACT

In conventional fluorescence microscopy, species are distinguished by colour. While these images provide an abundance of information about the sample, they are, in many aspects limited by artefacts and resolution, and some properties of the sample remain elusive. In fluorescence-lifetime imaging microscopy (FLIM), the characteristic lifetime of a fluorophore is measured in addition to intensity. This lifetime can depend on the local environment and may be altered by energy transfer to an acceptor. Therefore, FLIM allows for lifetime-based Förster resonance energy transfer (FRET), environment sensing inside cells, and lifetime-based multiplexing.

Due to the lack of single-molecule sensitive lifetime cameras, all single-molecule localisation microscopy (SMLM) techniques could not access the lifetime information so far. In this thesis, I present the implementation of SMLM based super-resolved FLIM with a confocal microscope. By rapid laser-scanning, pulsed excitation, and single photon detection, the lifetime is determined for all localised molecules. The technique provides optical sectioning and is compatible with two of the most important SMLM methods, direct stochastic optical reconstruction microscopy (dSTORM) and points accumulation for imaging in nanoscale topography (PAINT) imaging. Based on the lifetime information, two different fluorophores are distinguished in dSTORM measurements. This enables super-resolution microscopy with chromatic-aberration free multiplexing.

The recent development of single-photon sensitive lifetime cameras enables single-molecule wide-field FLIM which allows for higher frame rates over a larger field of view compared to confocal FLIM. In combination with metal-induced energy transfer (MIET), single molecules can be localised axially with nanometre precision.

Both methods can be readily employed for super-resolved environment sensing or 3D SMLM. The feasibility of super-resolved isotropic 3D imaging is shown in a proof of concept experiment.

CONTENTS

1 INTRODUCTION

With the invention of microscopy in the seventeenth century, the microcosm became visible for the first time. Robert Hooke observed structures of seeds, plants, insects, and many more, and his discoveries inspired the term *cell* in modern biology.[1] By developing single lens microscopes with high magnification, van Leeuwenhoek achieved a resolution of a few micrometres which enabled him to discover bacteria, single-celled eukaryotes, as well as blood and sperm cells. With advances in optics, such as achromatic and spherical aberration-corrected compound lenses, the resolution improved until reaching the so-called diffraction barrier. Ernst Abbe realised that the resolution is limited to approximately half of the wavelength due to the interference properties of light.[2] This wavelength dependency inspired the development of ultraviolet (UV) microscopes with the aim to increase the resolution by decreasing the wavelength. As first noticed by August Köhler, UV illumination can induce fluorescence in biological samples.[3] Soon, the potential of fluorescence to improve the weak image contrast of biological samples was discovered. With the introduction of highly specific and versatile immunolabeling by Albert Coons,[4] and the development of dichroic mirrors, fluorescence microscopy became popular in microbiology.

So far, microscopes relied on wide-field detection: The complete field of view was illuminated and the magnified images were observed by eye or captured on photographic film. A quantitative analysis of the images was tedious and had to be performed manually. Automatic analysis was enabled by the "flying-spot microscope", which was inspired by image generation in television. A light spot, created with a cathode-ray tube, was projected into the sample, and the transmitted light was focussed onto a photo-cell. To generate an image, the spot was scanned over the sample and the detected signal simultaneously reconstructed on a second cathode-ray tube monitor. Its main purpose was to generate sequential image data which could be analysed in real time even before the availability of powerful computers.[5] However, restricting the illumination to a spot in the focal plane had more advantages, as the existing wide-field microscopes were limited by scattering in the sample. This scattering reduced contrast, and small biological structures in tissue could not be imaged. Therefore, in one of the first attempts to study the connections between neurons in brain tissue, Marvin Minsky built the "double focusing" microscope. To avoid detecting the scattered light, the illumination light was focused into a tight spot in the sample and the transmitted light was focused on a pinhole in front of a point detector. This geometry rejected out-of-focus scattering and additionally provided optical sectioning.[6] While not achieving his ultimate goal, to create an Artificial Intelligence based on the observed neuronal connections, Minsky built the first confocal microscope.[7] Early implementations of confocal microscopy suffered from low illumination intensities, since the sharp focus was achieved by sending

the illumination light through a pinhole, which caused tremendous light losses and made image acquisition slow. With the invention of the laser, and the introduction of beam scanning instead of sample scanning, the acquisition speed could be increased.[8] Furthermore, with the high illumination intensities provided by lasers, confocal fluorescence microscopy became feasible.[9, 10] Today, confocal laser-scanning microscopy (CLSM) is one of the most commonly used microscopy techniques in biology and medicine, because it provides optical sectioning and background reduction that enables high contrast and 3D imaging.

Besides imaging, a confocal microscope is ideal for spectroscopic studies on a small number of molecules due to its tiny detection volume ($\sim$1 fL). In contrast to ensemble measurements, intensity fluctuations caused by molecular processes do not average out completely when only a few molecules are measured. Magde, Elson and Webb introduced fluorescence correlation spectroscopy (FCS) that analyses these fluctuations to retrieve diffusion coefficients or reaction rates.[11] Due to the point detection, it is straightforward to implement a spectral- or polarisation-resolved detection.[12] Even tough FCS observes fluctuations induced by single molecules, the early implementations were far from single-molecule sensitive.

Single molecules were first detected, albeit indirectly, by imaging the fluorescent product of an enzymatic reaction.[13] This approach, of biochemically amplifying the signal is the basis of modern techniques like PCR (polymerase chain reaction) and ELISA (enzyme-linked immunosorbent assay) that routinely detect single copies of DNA or other biomolecules. Following a similar idea to increase the signal, Hirschfeld detected single, diffusing biomolecules, by attaching a polymer chain with 80 – 100 bound fluorophores to single antibodies.[14] Direct, optical detection of single dye molecules using absorption was first demonstrated in a doped polymer crystal under cryogenic conditions by Moerner and Kador,[15] soon followed with fluorescence detection by Orrit and Bernard.[16] The first detection of single fluorophores at ambient conditions and in solution, by the group of Keller, required extensive efforts to reduce background signal:[17] In a modified flow cytometer, a defined jet of fluorophore solution was created by hydrodynamic flow focusing and transported through a focused excitation beam. The fluorescence was collected perpendicularly to the flow and excitation beam, and detected with a single-photon sensitive detector. The controlled transport of the molecules trough the relatively large detection volume ($\varnothing$ 10 µm) was designed to quantify the brightness of fluorophores in each detection event for applications like DNA sizing with intercalating fluorophores.[18] Soon after, FCS with single molecule concentrations was demonstrated by Rigler and Mets.[19] In their experimental conditions, each molecule diffusing through the focus created a burst of fluorescence. Instead of correlating the signal, analysis of single bursts enabled the classification of individual detection events.[20, 21]

To increase the observation time per molecule, single molecules can be immobilised on a surface. The increased observation time, in combination with a confocal single-photon detection, enabled the measurement

of orientation and spectra of single fluorophores, immobilised on a dry polymer surface.[22] The introduction of sensitive cameras allowed wide-field detection of single molecules in an aqueous environment: To reduce the background signal, the group of Yanagida combined wide-field detection with total internal reflection illumination to solely illuminate the sample close to the surface of a prism. This way, single ATP (adenosine triphosphate) turn-over events of immobilised myosin motors were observed.[23] The wide-field detection allowed for a faster imaging than confocal scanning and enabled the tracking of single diffusing lipids in a membrane. For this, the individual molecules were localised in sequential images with tens of nanometre precision.[24] Using single-molecule detection in combination with Förster resonance energy transfer (FRET), the dimerisation of single molecules became observable in live-cell experiments.[25]

Even before the first confocal and wide-field detections of surface-immobilised single molecules, single-molecule detection was achieved with near-field scanning optical microscopy (NSOM).[26] In this technique, the illumination was confined by a 100 nm aperture at the tip of a tapered optical waveguide which was scanned over the surface. The confinement of the illumination to a spot below the diffraction limit reduced the size of the detection volume and made NSOM the first optical super-resolution technique, even tough the requirement for the scanning probe to be in close proximity of the fluorophores limited its broad applicability. The first far-field super-resolution technique, which also decreased the effective size of the detection volume, was stimulated emission depletion (STED) microscopy by Klar and Hell.[27] Here, fluorophores are excited in a diffraction limited focus but are then immediately forced back to the ground state *via* stimulated emission within a "doughnut-shaped" region around the centre of the beam. In STED microscopy, the resolution is no longer limited by diffraction but by the intensity of the depletion beam used for inducing stimulated emission.

The first wide-field technique which significantly improved the image resolution was structured illumination microscopy (SIM): the sample is illuminated with a spatially modulated pattern and several images are recorded for different positions and orientations of this pattern. By combining the diffraction limit of both illumination and detection, SIM doubles the achievable resolution compared to wide-field microscopy.[28] As mentioned above, localising and even tracking single molecules with high precision was possible with camera-based wide-field methods. However, if the molecules were spaced by less than the diffraction limit, they could not be distinguished. This changed with the development of switchable fluorophores: In photoactivated localisation microscopy (PALM), Betzig et al. [29] and Hess, Girirajan and Mason [30] used photoactivatable proteins, while Rust, Bates and Zhuang [31] employed organic fluorophores, which could be switched on and off multiple times, in stochastic optical reconstruction microscopy (STORM). In both techniques, only a small fraction of fluorophores is in an on-state at any time. The fluorophores are switched on by illumination with a wavelength shorter than the fluorescence excitation wavelength and,

subsequently, imaged until they either photobleach or switch off. This cycle is repeated many times. Both techniques, PALM and STORM, were the first members of single-molecule localisation microscopy (SMLM) methods which all rely on localising a changing subset of single molecules in many frames. Since each localisation is more precise than the diffraction limit, the resulting reconstruction is *super-resolved*. With modern fluorophores, super-resolution microscopy routinely resolves structures of tens of nanometre size, which makes it possible to optically study sub-cellular structures, such as cell organelles and large protein complexes.

Besides the overall intensity, fluorescence conveys additional information about the sample. This is exploited by different fluorescence spectroscopy techniques which analyse, for example, the excitation or emission spectra, intensity fluctuations (FCS), or the fluorescence lifetime. The fluorescence lifetime is defined as the average time a fluorophore stays in its excited state until a photon is emitted. For organic fluorophores, the lifetime is typically on the order of a few nanoseconds. The first fluorometer, which could measure the average lifetime of a sample, was built by Gaviola.[32] It relied on an intensity-modulated excitation combined with a synchronised sensitivity-modulated detection, to measure the phase shift of the fluorescence light with respect to the excitation light. With this setup, it was demonstrated that the lifetime is specific for different fluorophores and depends on their environment. To extend this modulation-based spectroscopic approach to wide-field microscopy, sensitivity-modulated cameras were developed.[33, 34] These methods, also known as frequency-domain fluorescence-lifetime imaging microscopy (FLIM), enabled the wide-field acquisition of lifetime-resolved images. However, due to the modulation of the detection, the sensitivity of these methods is not sufficient for single-molecule detection. In contrast, time-domain FLIM typically uses a confocal microscope with a pulsed excitation, and a time-correlated single-photon counting (TCSPC) detection which records the arrival time of each photon. TCSPC detection thereby gives access to the full distribution of arrival times and hence directly reveals multi-component decays. This single-photon detection facilitates single-molecule sensitivity; in fact, the first single-molecule detection in solution by the group of Keller already relied on the arrival times to separate fluorescence from scattering.[17]

The lifetime information in FLIM provides a versatile, intensity-independent information about the sample. In cells, the lifetime of many endogenous fluorophores depends on their binding or oxidation state. This was exploited early on in imaging of metabolic states.[35, 36] In combination with environment-sensing fluorophores, the lifetime gives access to local ion concentration (pH, Ca^{2+}, Mg^{2+}, etc.), viscosity, or various membrane properties (order, potential, tension, etc.).[37] FLIM, together with FRET, can measure nanometre distances and conformational dynamics of proteins.[38]

So far, FLIM measurements have either been fast, i. e. when using a camera-based frequency-domain technique, or single-molecule sensitive, in the case of time-domain confocal FLIM. Therefore, the lifetime information was not accessible with SMLM. In this thesis, different

approaches to combine single-molecule localisation with fluorescent lifetime information were developed and evaluated. In chapter 3, we combined confocal laser-scanning microscopy with single-molecule localisation to implement super-resolved FLIM. In measurements on fixed cells, we validated our method by demonstrating lifetime-based multiplexing, which conceptually avoids any chromatic aberration that affects many current multi-colour super-resolution techniques. Since the publication of our implementation,[39] a second approach that combines single-molecule localisation with lifetime information was published, which relies on pulsed MINFLUX for localisation.[40]

In chapter 4, we performed single-molecule sensitive wide-field FLIM by employing a novel TCSPC camera. Despite a low photon detection efficiency, we succeeded in distinguishing different fluorophores based on their lifetime. In combination with metal-induced energy transfer (MIET), a distance-dependant lifetime quenching by a metal film, we demonstrated axial localisation of single molecules with nanometre resolution.

Both techniques might be utilised in other common applications of FLIM such as environment sensing or FRET. However, existing SMLM software was not compatible with TCSPC-data. Therefore, it was important to make the data analysis accessible to users without requiring that they are expert programmers. For this purpose, I created a software which directly reads the raw data and performs single-molecule detection, lifetime fitting, and reconstruction of super-resolved FLIM images. This software is presented in chapter 5, which contains details on the implementation and describes application examples.

2 FUNDAMENTALS

In this chapter, theoretical concepts and experimental techniques are introduced. An extensive introduction into fluorescence and fluorescence spectroscopy can be found in [41, 42], and into fluorescence microscopy and super-resolved methods in [43–45].

2.1 FLUORESCENCE

Luminescence is light emission from a material transiting from an excited electronic state back to its ground state. The excitation can have different sources, *e. g.* biochemical reactions (bioluminescence), electric current (electroluminescence) as in light emitting diodes, or photon-absorption (photoluminescence) as in fluorescence and phosphorescence. The Jablonski diagram in figure 2.1(a) illustrates the important transitions in the electronic system of a fluorescent molecule. The system rests in its electronic ground state S_0 until it is excited by the absorption of a photon with wavelength λ_{ex} (blue arrow). Depending on the photon energy, the transition occurs to any of the vibronic levels of the first excited electronic state S_1. The system quickly ($\sim 10^{-12}$ s) relaxes to the vibronic ground state of S_1. From here, different decay channels lead to the ground state: a non-radiative decay with rate k_{nr} can occur by internal conversion to a high vibronic level of S_0 followed

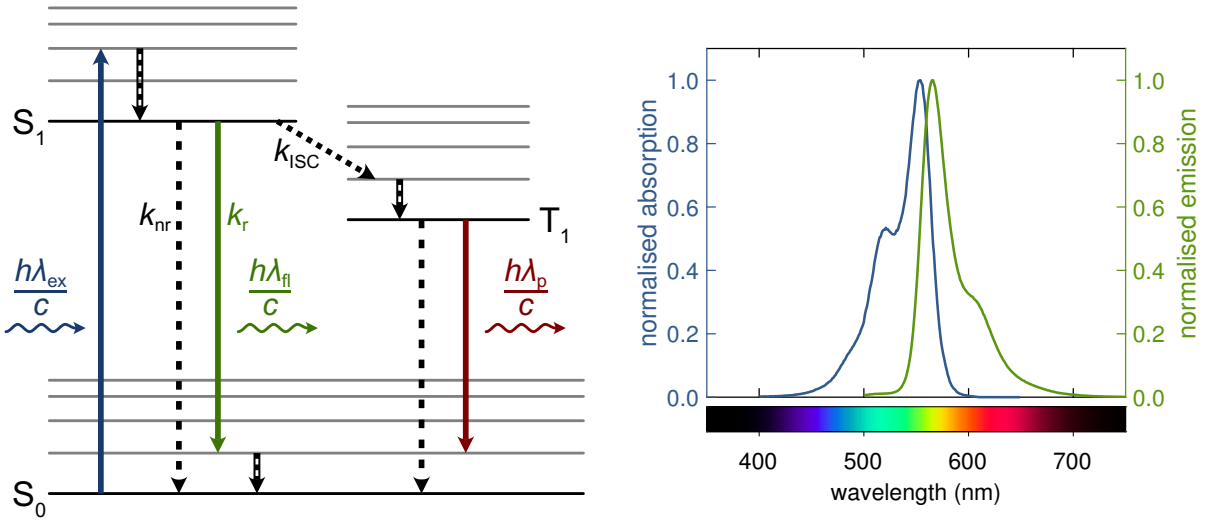

(a) simplified Jablonski diagram

(b) absorption and emission spectra

Figure 2.1: (a) Jablonski diagram showing molecular electronic transitions leading to fluorescence and phosphorescence. Radiative transitions are indicated by coloured, solid arrows, non-radiative transitions are dotted. (b) Absorption spectrum and emission spectrum of the organic fluorophore Cy3.[46]

by vibronic relaxation; the system can emit a fluorescence photon (green arrow) with radiative rate k_r; or it can pass to the triplet electronic state T_1 (inter system crossing) with rate k_{ISC}. The radiative decay $T_1 \rightarrow S_0$ is connected with phosphorescence. The transitions $S_1 \rightarrow T_1$ and $T_1 \rightarrow S_0$ are *forbidden* transitions because the spin of the excited electron has to be reversed. This typically leads to low transitions rates ($k_{ISC} \ll k_{nr} + k_r$) and a long triplet lifetime ($\gtrsim 10^{-7}\,\mathrm{s}$). Therefore, the system can be approximated as a two state system where the fluorescence lifetime τ of the excited state S_1 is determined by

$$\tau = \frac{1}{k_r + k_{nr}} \tag{2.1}$$

and is typically on the order of $10^{-9}\,\mathrm{s}$ for organic fluorophores. The ratio of radiative transitions to absorptions, called quantum yield, is given by

$$\mathrm{QY} = \frac{k_r}{k_r + k_{nr}}. \tag{2.2}$$

In the case of non-radiative transitions, the energy is dissipated to neighbouring molecules *via* collisions, therefore k_{nr}, and hence QY and τ, can be sensitive to the local environment.

How efficiently a photon with energy $h\lambda_{ex}/c$ can be absorbed depends on the overlap of the wave function of the initial S_0 vibronic state with the wave functions of the final S_1 vibronic states. Similarly, the probability of the radiative transition from S_1 to a vibronic state of S_0 is proportional to the overlap of the wave functions of the involved vibronic states. This so-called Franck–Condon principle manifests itself in the structures of absorption and emission spectra (figure 2.1(b)). Energy conservation demands $\lambda_{ex} \leq \lambda_{fl}$ for each excitation-emission cycle and, due to vibronic relaxation, the absorptions and emission maxima are several nanometres apart. This spectral shift, the Stokes shift, allows for the efficient separation of excitation and emission light by spectral filters.

2.2 FLUORESCENCE MICROSCOPY

Optical microscopes utilise multiple lenses to create a magnified image of a sample, which can be viewed by eye or captured by a camera. Contrast is generated through the interaction of the illumination light with the sample. Common microscopy techniques are based on absorption (bright field), scattering (dark field), phase shifts by refractive index variations (phase contrast), or fluorescence. Many biological samples absorb weakly and are non-fluorescent in the visible region. This facilitates the selective introduction of fluorescent markers which distinguishes fluorescence microscopy from other methods and allows for an exceptional contrast and high specificity. There are different options how to stain a structure of interest in a sample. For some targets, *e. g.* DNA, mitochondria, or membranes, there exist fluorophores that selectively target these structures. Alternatively, fluorophores can be

bound to selectively binding ligands like antibodies as in the case of immunolabelling. For live-cell experiments, the genetic information for fluorescent proteins, directly fused with its target, may be introduced into cells.

In a typical fluorescence microscope (figure 2.2), the sample is evenly illuminated by light suitable for exciting the used fluorophore (blue). This is achieved by focussing the excitation light into the back focal plane of the objective. The fluorescence light emitted by the sample (green) is collected by the same objective (epi-fluorescence setup) and, taking advantage of the Stokes shift, separated from the excitation light with a dichroic mirror. Finally, the fluorescence light is imaged on a camera by a tube lens. This type of illumination and detection, also called wide-field, allows for a simultaneous acquisition of an image over the whole field of view.

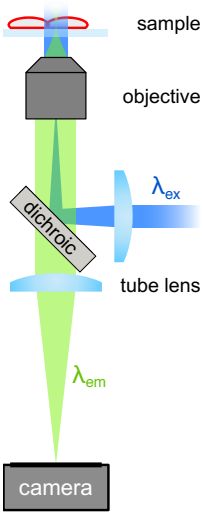

Figure 2.2: Schematic of a wide-field fluorescence microscope.

Biological samples are typically imaged in an aqueous buffer through a glass cover slide. By adding an immersion medium instead of air between sample and objective, the collection angle of the objective can be increased. In *total internal reflection* (TIR) illumination, the excitation light is limited to angles above the TIR angle of the glass-sample interface, so that only molecules within a range of ∼200 nm to the interface are excited by the exponentially decaying evanescent wave. TIR illumination thereby drastically decreases background from regions of the sample far away from the surface.

Especially for imaging deep inside thicker samples, background generated by fluorophores above and below the focal plane can become problematic. Confocal microscopy reduces the background by creating a confocal volume (figure 2.3): excitation is restricted to a tight spot in the focal plane, and fluorescent light from above and below the focal plane is blocked by a pinhole (optical sectioning). Fluorescence light passing the pinhole is detected by a point detector. To acquire an image, the desired field of view needs to be scanned one pixel at a time by either moving the sample or the excitation and detection volume. Since only fluorescence from the confocal volume is detected, the contrast is improved. 3D images can be generated by sequentially recording multiple planes.

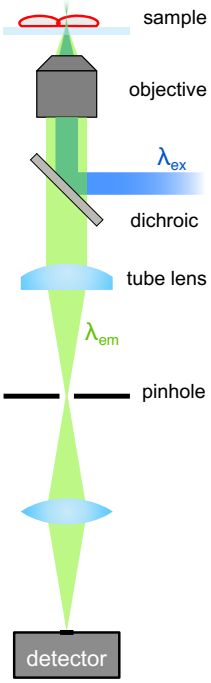

Figure 2.3: Schematic of a confocal fluorescence microscope.

Diffraction limit

There is no fundamental limit to how much an image can be magnified. However, due to the wave-nature of light, structures smaller than half the wavelength cannot be resolved. This is expressed in the famous equation for the diffraction limit first formulated by Ernst Abbe:[2]

$$d = \frac{\lambda}{2n \sin\theta} = \frac{\lambda}{2\mathrm{NA}} \tag{2.3}$$

Two lines separated by a distance less than d cannot be resolved. Here, λ denotes the wavelength of light, n the refractive index of the sample medium (assuming that an immersion medium with at least the same refractive index is used), and θ the collection half-angle of the objective. The numerical aperture NA, defined as $n \sin\theta$, is a property of the

objective. For conventional fluorescence microscopy, optical diffraction limits the resolution to $\gtrsim 200\,\mathrm{nm}$.

Closely related to the diffraction limit is the *point spread function* (PSF) of the microscope which describes the shape of the image of a point emitter. The PSF is often analytically described by the square of the Fourier transform of a circular aperture, resulting in the rotationally symmetric Airy pattern.[47, 48] The intensity I of the PSF in dependence of the lateral distance from the optical axis ρ is given by

$$I(\rho) = I_0 \left[\frac{2J_1(k\rho\mathrm{NA})}{k\rho\mathrm{NA}} \right]^2 \tag{2.4}$$

with I_0 being the peak intensity, NA the numerical aperture of the objective, $k = 2\pi/\lambda$ the vacuum wave vector, and J_1 denoting the Bessel function of the first kind. For many applications, the Airy pattern can be approximated by a Gaussian distribution:

$$I(\rho) \approx I_0 \exp\left(\frac{-\rho^2}{2\sigma^2}\right) \quad \text{with} \quad \sigma \approx 0.21\frac{\lambda}{\mathrm{NA}}. \tag{2.5}$$

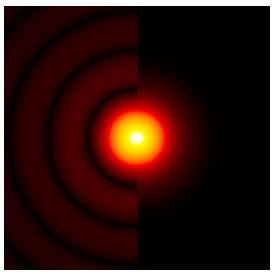

Figure 2.4: Airy disk (left) and Gaussian approximation (right). To highlight the higher orders, $\sqrt{I}$ is plotted.

In figure 2.4, it is evident that the Gaussian distribution approximates the central peak well. To make the difference visible, the absolute field amplitude $\sqrt{I}$ is plotted instead of the intensity I. For a confocal microscope, the equations are more complex but result in a similar pattern. In the limit of an infinitesimal small pinhole, the PSF is ~ 1.4 fold smaller than for a wide-field microscope.[49]

Since objects much smaller than the diffraction limit can be treated like point sources, the PSF can be used to describe the image of a single fluorophore. However, the exact experimental PSF depends on additional parameters including molecule orientation, and it can be distorted by aberrations of the imaging optics.

2.2.1 *Super-resolution microscopy*

In conventional microscopy (wide-field, confocal), it is not possible to capture an image with a resolution below the diffraction limit. However, multiple super-resolution techniques have been developed, circumventing the diffraction limit. All methods ensure that only a subset of the fluorophores can be detected at any time and vary this subset over the course of the measurement. There are two main groups of methods: In the first group, a patterned illumination is scanned over the sample. In its most popular version, *stimulated emission depletion* (STED) microscopy, the fluorophores are excited within a diffraction-limited spot but are then immediately stimulated to emission in a "doughnut-shaped" region around the centre. The laser light used for inducing the stimulated emission has a longer wavelength than most of the unstimulated fluorescence. By detecting only the remaining fluorescence after stimulated de-excitation of all fluorophores in the doughnut-shaped region around the centre, the size of the detection volume is effectively decreased. This is illustrated in figure 2.5. The final resolution of

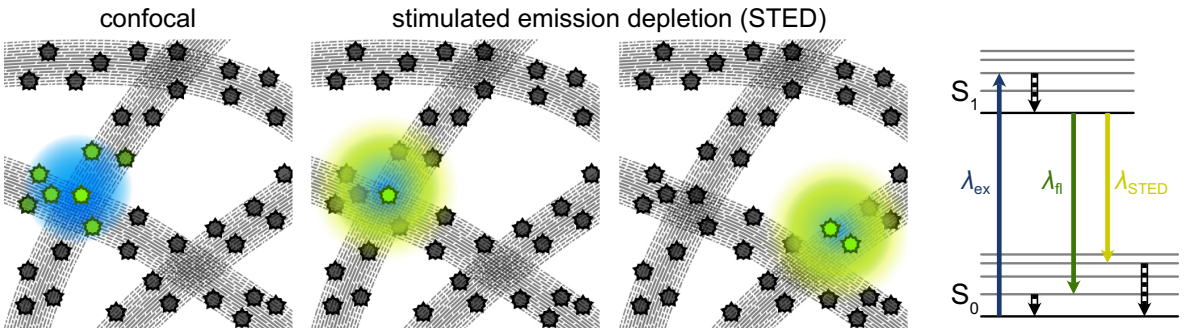

Figure 2.5: In confocal fluorescence microscopy (left), molecules are exited and detected within a diffraction limited spot. STED microscopy (centre) decreases the effective size of the detection volume by stimulating excited molecules to emission by a doughnut-shaped beam co-aligned with the excitation beam. The stimulated emission (right) has a longer wavelength than most of the unstimulated emission and is filtered out. As in confocal microscopy, scanning is required to generate an image.

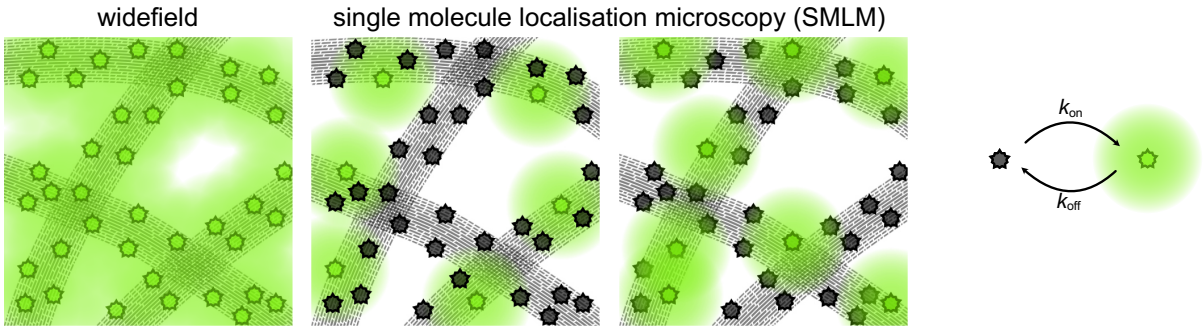

Figure 2.6: In wide-field fluorescence microscopy (left), all labels are in the on-state, rendering it impossible to distinguish individual, overlapping emitters. In single-molecule localisation microscopy (SMLM), most of the labels are in the off-state and only a few are switched on stochastically. By iterating over many subsets and localising the emitters in each, an image can be reconstructed from the individual PSF centre positions.

STED microscopy depends on the power of the depletion beam.[50] The concept of STED to optically switch off a defined region to decrease the size of the detection volume can also be implemented with different molecular transitions. This was demonstrated with stable dark states of switchable fluorescent proteins [51] and organic fluorophores,[52] where the slower switching allowed for a lower power of the depletion beam compared to conventional STED.

In the second group, *single-molecule localisation microscopy* (SMLM), the stochastic on and off switching of single molecules is exploited. The position of the labels is localised in wide-field images by determining the centre of their PSFs. This localisation can be done at much higher precision than the diffraction limit but requires that most labels are in their off-state. The concept of SMLM is depicted in figure 2.6. STED and SMLM put very different requirements on the label: STED needs fluorophores which are stable enough for many excitation (stimulated) emission cycles, while SMLM requires a mechanism to switch the label. Some of the most common switching approaches are discussed in the next section.

Switching mechanisms

Photoswitching & photoactivation One of the first labels employed for localisation-based super-resolution were semi-conductor quantum dots, exhibiting a long photo-induced off-state.[53] Later it was discovered that some organic fluorophores can be switched with a high level of control in specific environments.

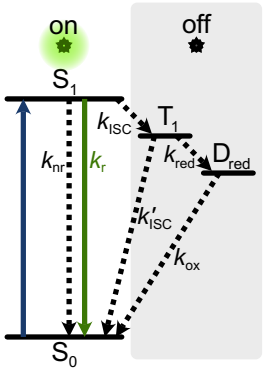

Figure 2.7: Simplified Jablonski diagram showing transitions in photoswitchable fluorophores.

Many cyanine, rhodamine and oxazine derivatives are photoswitchable. The typically involved states and transitions are illustrated in the Jablonski diagram in figure 2.7. The triplet state T_1 is reduced with rate k_{red} leading to a stable dark state D_{red}. The reduction is facilitated by primary thiols or phosphines, like β-mercaptoethanol (BME), β-mercaptoethylamine (MEA), or tris-2-carboxyethyl phosphine (TCEP) added to the buffer. The underlying reactions differ, but in all cases the conjugated π-electron system is disrupted.[54, 55] The fluorophore switches back to the excitable ground state S_0 *via* oxidation by an oxidising species. The rate of this process k_{ox} is increased by energy transfer from a near by fluorophore (the activator) which was the basis of the initial implementation of *stochastic optical reconstruction microscopy* (STORM).[31] However, the transition also takes place without activator and can be accelerated by illumination with ∼400 nm light, as demonstrated by direct STORM (dSTORM).[56] Some oxazines, *e. g.* Atto 655, can be further reduced, leading to multiple long-living off-states.[55]

Typically, the first step in SMLM experiments with photoswitchable fluorophores is to switch most of the fluorophores to the off-state. This is commonly done by exciting the fluorophores with sufficient intensity. Alternatively, chemical reducing agents may be used.[57]

Besides organic fluorophores, many fluorescent proteins can be photoswitched. In general, fluorescent proteins emit less photons than organic fluorophores before bleaching or off-switching. However, their unique advantage of being genetically encodable makes them attractive for live-cell experiments.[58] A special variant of photoswitching is irreversible photoactivation of an initially non-fluorescent molecule. Photoactivatable fluorescent proteins were the basis of two of the earliest SMLM implementations, the closely related *photoactivated localisation microscopy* (PALM) [29] and *fluorescence photoactivation localisation microscopy* (fPALM).[30] Many photoactivated fluorophores stay in the on-state until they are irreversibly photobleached. However, variants exist which can be repeatedly switched between on- and off-states after initial activation.

Spontaneous switching Some fluorophores are in a chemical equilibrium between a fluorescent and a dark form and switch spontaneously at room temperature. An example for this class of *self-blinking* fluorophores are silica-rhodamine derivatives [59] and rhodamine derivatives [60] that can undergo a reversible intramolecular spiro-ring formation with a pH-dependant equilibrium. Typically, SMLM with self-blinking fluorophores requires a lower illumination power than used for photo-switching, which reduces the photo-induced damage to

the sample, especially in live-cell measurements. Another advantage is that no special buffer is required and that derivatives with different pH-dependencies exist.[59]

Transient labelling A completely different approach to generate switching events is transient binding of a fluorophore to the structure of interest. In the original version of *points accumulation for imaging in nanoscale topography* (PAINT), Nile red, which is weakly fluorescent in aqueous buffer and becomes much brighter in a less polar environment, was employed to image lipid membranes.[61] During the measurement, the fluorophore is present at a low concentration in the imaging buffer. After binding to the target, the fluorophore is, depending on its unbinding kinetics, either photobleached or unbinds after a short time. In general, the free diffusion is fast enough to create a uniform background, while the bound fluorophores can be localised.

To introduce specific binding to a wide variety of targets, antibodies [62] or specific binding peptides (*e. g.* lifeact),[63, 64] labelled with organic fluorophores or fluorescent proteins, are utilised.

An extension of PAINT, allowing the fine-tuning of the binding kinetics, is DNA-PAINT.[65] Here, the target is labelled with a short single stranded DNA-oligomer (docking strand). In the imaging buffer, a fluorophore-labelled, complementary DNA-strand (imager strand) is provided. As illustrated in figure 2.8, the imager strand transiently binds to the docking strand. The sequence of the DNA and the concentration of the imager strand determine the on- and off-times for each binding site, respectively.

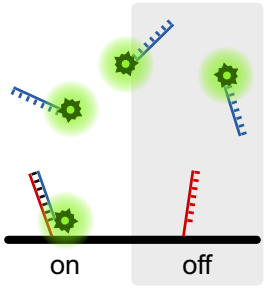

Figure 2.8: DNA-PAINT: Fluorophore-labelled imager strand transiently binds to a complimentary docking strand.

In PAINT-like methods, the measurement time is not limited by photobleaching, since the fluorophores are replenished from solution. For some implementations, such as DNA-PAINT, this comes at the cost of an elevated background fluorescence from the solution.

Localisation precision & resolution

In SMLM, the resolution of the reconstructed image depends on the localisation precision and the quality of the labelling. The localisation precision of a PSF depends on the number of detected photons N and the width of the PSF σ as $\sigma/\sqrt{N}$. However, in reality additional error sources such as background, the finite pixel size, noise from the camera, or errors introduced by fitting need to be considered. If the recorded intensities can be converted to photons, best results are achieved by using a maximum likelihood estimator (MLE) due to the Poissonian nature of photon detection. Based on the Cramér-Rao lower bound, Mortensen et al. [66] derived an expression for the uncertainty of the lateral position which was later modified by Rieger and Stallinga [67] to cover MLE methods:

$$\Delta x|^2_{\mathrm{MLE}} = \frac{\sigma^2 + a^2/12}{N}\left(1 + 4\chi + \sqrt{\frac{2\chi}{1+4\chi}}\right) \tag{2.6}$$

Here, a denotes the pixel size and χ denotes approximately the ratio of background-to-peak signal defined as

$$\chi = \frac{2\pi b \left(\sigma^2 + a^2/12\right)}{Na^2} \tag{2.7}$$

with b being the average background per pixel. It can be seen that in the limit of small pixels and a high signal-to-background ratio, equation (2.6) converges to σ^2/N, making it obvious that both increasing the number of photons N and decreasing the width of the PSF σ improve the localisation precision.

Another important aspect that influences the final image resolution is the labelling with fluorophores. Based on the Nyquist-Shannon-Theorem, the spatial resolution is limited to twice the mean label distance.[68] An insufficient label density can lead to artefacts such as gaps in continuous structures. Further connected to the labelling is the so-called linkage error, the distance between target and actual fluorophore position. Depending on the geometry of the structure, this can have different effects, *e. g.* cylindrical microtubules having an apparently larger diameter. While their outer diameter is 25 nm, primary and secondary immunolabeling lead to an apparent diameter of ∼60 nm. This linkage error, caused by the size of the antibodies, can be reduced using nanobodies instead.[69]

Further super-resolution techniques

In the past years, a large variety of super-resolution techniques were developed which deserve to be mentioned. However, discussing all of them is beyond the scope of this thesis.

The statistical switching of fluorophores provides information, even if the fluorophores are too dense to be localised individually. This is employed in *super-resolution optical fluctuation imaging* (SOFI) [70] and the closely related technique *super-resolution radial fluctuations* (SRRF),[71] which statistically analyse the local intensity fluctuations in a fit-free manner.

The combination of single-molecule localisation microscopy with other techniques can increase the achievable image resolution even further. The combination of SIM with DNA-PAINT or STORM (called SIM-FLUX) does approximately double the resolution.[72] Although the details are more complicated, the structured illumination results in an approximately two-fold improvement of the localisation precision.

Highest resolutions have been achieved by localising single molecules with a doughnut-shaped excitation beam: In MINFLUX, the central minimum of the beam is moved around a position estimate of the molecule to minimise its excitation and therefore align the beam with the molecule.[73]

Finally, there are also non-optical ways to circumvent the diffraction limit: A conceptually simple but technically challenging method is to physically expand the sample prior to imaging (expansion microscopy). By embedding the sample into a gel and swelling this gel, structures

originally smaller than the diffraction limit can be resolved with a conventional microscope.[74] To resolve even smaller structures, expansion microscopy can be combined with other super-resolution techniques such as STED [75] or dSTORM.[76]

Multicolour super-resolution techniques

For answering many biological questions, the relative organisation of multiple targets is relevant. To simultaneously image multiple targets in conventional fluorescence microscopy, each target is labelled with a fluorophores of a distinct colour. This approach can be applied in dSTORM by using fluorophores of different colours that are switchable under the same buffer conditions.[77] However, this needs careful subpixel alignment of the colour-channels and calibration to compensate inevitable chromatic aberrations.[78]

For STORM, using one switching fluorophore but different activators for each target eliminates chromatic aberration but leads to some cross talk.[79] Chromatic aberrations can be reduced substantially by relying on only one excitation wavelength and using spectrally overlapping fluorophores. For subsequent classification, either spectral splitting [80, 81] or a spectrally resolved detection[82] can be utilised.

In confocal microscopy, STED, and MINFLUX, the position information is encoded by the position of the excitation (or depletion) focus. Thus, spectrally resolved detection does not suffer from chromatic aberration.[83, 84] In the case of STED, even multiple excitation wavelengths can be combined without introducing chromatic aberration as long as the same depletion wavelength is used for all fluorophores.[85]

Conceptually similarly free of chromatic aberration is monochromatic DNA-PAINT. Each target is labelled with a different docking strand. In exchange-PAINT, the corresponding imager strand for one target is added to the imaging buffer, and the buffer is exchanged sequentially for each target.[86] Because all imager strands are labelled with the same fluorophore, there are no chromatic aberration-induced mismatches between different targets. Alternatively, the detection of multiple targets can be parallelised by distinguishing targets based on their sequence-dependent blinking kinetics.[87]

Axial localisation

All methods discussed so far provide super-resolution along the lateral direction (focal plane). For imaging along the optical axis, a similar diffraction limit exists as for imaging along the lateral direction, and it is given by [44, 48]

$$d_z = \frac{\lambda}{n(1-\cos\theta)} = \frac{\lambda}{2n\sin^2\frac{\theta}{2}} \approx \frac{2\lambda}{n\sin^2\theta} = \frac{2\lambda n}{\mathrm{NA}^2}. \tag{2.8}$$

The approximation on the right hand side is valid for small angle θ. The ratio between the lateral resolution limit d (equation (2.3)) and the

axial resolution limit d_z is therefore given by

$$\frac{d_z}{d} = \frac{\lambda}{2n \sin^2 \frac{\theta}{2}} \frac{2n \sin \theta}{\lambda} = \frac{\sin \theta}{\sin^2 \frac{\theta}{2}} > 2 \tag{2.9}$$

which becomes 2 when the collection half-angle θ reaches its theoretic maximum value of 90°. In practice, typically ratios of 3 – 4 are encountered.[88]

In a wide-field microscope, the lateral size of the PSF increases when moving above or below the focal plane. In SMLM, this enables the selection of localisations close to the focal plane based on the PSF size. However, the symmetry of the PSF around the focal plane makes axial localisation based on the PSF size ambiguous in all other cases. Therefore, it is not possible to determine whether a molecule is above or below the focal plane. This symmetry is broken in PSF engineering techniques, as illustrated in figure 2.9. PSF engineering for axial localisation was first demonstrated by introducing astigmatism by placing a cylindrical lens in the detection path. The aspect-ratio of the lateral cross-sections of the astigmatic PSF changes monotonically, and the axial position can be determined, after calibration, from the shape of the PSF.[89] By using spatial light modulators or phase masks, more complicated PSF shapes can be engineered, for example the double helix PSF [90] or the tetrapod PSF [91] which both extend the accessible axial range.

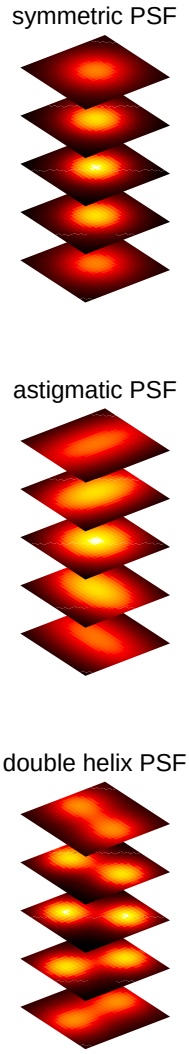

Figure 2.9: Illustration of PSF shapes.

Alternatively, the fluorescence light may be split into two or more images with different focal planes, which allows to determine the axial position of a fluorophore using a 3D PSF model.[92, 93] A detailed comparison of these approaches and their axial ranges can be found in reference [94]. In all of theses approaches, the lateral size of the PSF increases, which thus leads to a reduced lateral localisation precision. Increasing the PSF size is avoided when using self-interference to add high-frequency modulations to an otherwise unchanged PSF.[95] This only requires a smaller pixel size and therefore allows for 3D localisation without a significant decrease in lateral resolution. The axial localisation precision for astigmatism, biplane imaging, and the double helix PSF was derived by Rieger and Stallinga.[67] It depends on the desired axial range but is always several times larger than the lateral localisation precision.

Unlike the methods discussed above, interferometric methods provide an axial resolution that is larger than the lateral resolution. In these methods, fluorescence is collected with two objectives from both sides of the sample, brought into interference twice, and imaged as three or four corresponding images. Due to self-interference, the brightness of a molecule in the different images depends on its axial position. This principle is experimentally very demanding but has been successfully applied to the SMLM methods PALM (iPALM) [96] and dSTORM (4Pi-SMS).[97] Similarly, the interference of two depletion beams entering the sample from opposite directions is exploited in isoSTED to create an isotropic detection volume.[98]

Near field effects, such as the evanescent wave above a glass surface in TIR illumination, exhibit a strong distance dependence. In variable

angle TIRF, the penetration depth of the evanescent wave is varied by scanning the illumination angle. The distance to the surface is than calculated from the intensity changes.[99] This method achieves high axial resolutions but is, due to the limited speed, difficult to combine with lateral super resolution techniques.

In *supercritical angle fluorescence* (SAF), light emitted from a fluorophore above the critical angle couples into the cover glass. The efficiency of this coupling decreases approximately exponentially with increasing distance to the surface.[100] By comparing the supercritical to the undercritical intensity for each localisation, the axial position of an emitter can be determined.[101, 102] Due to the limited range of the near field, these techniques are typically limited to less than one wavelength distance to the surface. Since each localisation is determined relative to the glass surface, these techniques are not affected by axial sample drift.

Conventional STED is not super-resolving along the axial direction. To improve the axial resolution of STED as well as MINFLUX, a beam with maxima above and below the focus is created with a phase mask. This type of beam provides a lower lateral resolution but can be combined with a conventional doughnut-shaped beam to achieve 3D super-resolution.[84, 103]

2.3 METAL-INDUCED ENERGY TRANSFER

In section 2.1, the fluorescence lifetime τ and its relation to the radiative rate k_r and non-radiative rate k_{nr} was introduced. If an excited fluorophore can transfer its energy to another acceptor, an additional decay channel with rate k_{et} needs to be considered. This energy transfer reduces the lifetime, and equation (2.1) becomes

$$\tau = \frac{1}{k_r + k_{nr} + k_{et}}. \tag{2.10}$$

In general, the energy transfer exhibits a strong dependence on the distance between the excited fluorophore and the energy acceptor. Different molecules or materials can serve as acceptor, *e.g.* a second fluorophore, a non fluorescent organic molecule (dark quencher), or a metal surface.

At extremely short distances (<1 nm) between the fluorophore and the acceptor, the molecular orbitals can overlap. This enables Dexter energy transfer or *photoinduced electron transfer* (PET), the exchange or transfer of one electron between the molecules. These quantum mechanical interactions are extremely efficient but require direct contact.[41]

At distances of several nanometres, the dipole moments of the excited fluorophore (donor) and an acceptor fluorophore interact, leading to *Förster resonance energy transfer* (FRET).[104] The transfer rate for the donor-acceptor distance r is given by

$$k_{fret} = \frac{1}{\tau_d}\left(\frac{R_0}{r}\right)^6, \tag{2.11}$$

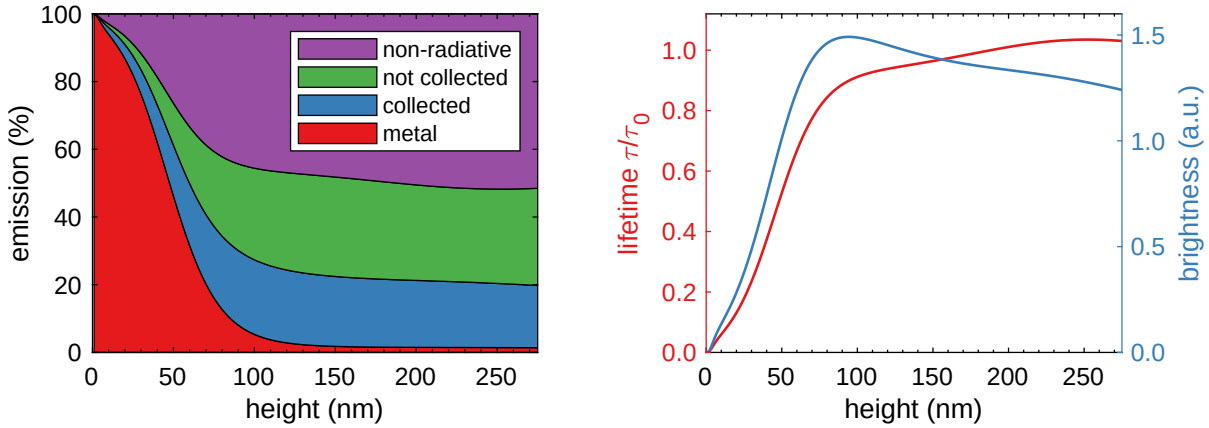

(a) emission channels (b) MIET curve

Figure 2.10: MIET distance-lifetime curve calculated for the fluorophore Alexa 647 ($\lambda_{em} = 671\,nm$, $QY = 0.33$) and a random orientation of the fluorophore. The MIET substrate consists of a 10 nm gold film on glass. (a) After excitation, the energy is either transferred to the metal, or emitted as fluorescence into the far-field, or dissipated non-radiatively. From the emitted fluorescence, only some part is collected by the objective ($NA = 1.49$). (b) The distance dependence of the transfer affects the lifetime and brightness of the fluorophore. Adapted from [109].

where τ_d is the initial donor fluorophore lifetime. The Förster radius R_0 depends on the spectral overlap between donor emission and acceptor absorption spectra, and the angle between the interacting dipol moments. This angle is difficult to measure and is therefore often assumed to be random. The distance r can be determined by either measuring the intensity ratio of donor and acceptor fluorescence or the lifetime of the donor. Typically, distances of $\sim 2-10\,nm$ can be measured.[41]

Instead of a molecule, a conducting particle or surface can serve as an acceptor. In *metal-induced energy transfer* (MIET), a thin metallic film modulates the fluorophore's brightness and lifetime. The energy transfer from the excited molecule to the metal can be modelled semi-classically by describing the fluorophore as an oscillating electric dipole that generates an electromagnetic wave. This wave interacts with the metal: it is partially transmitted and partially reflected which creates interference with direct emission of the dipole. This self-interference is a general dipol phenomenon also found close to a dielectric mirror.[105] At small distances, the excited state energy of the fluorophore can be transferred to surface electron density waves (plasmons) in the metal, which are attenuated due to a non-zero extinction coefficient (imaginary part of the refractive index of the metal). In practice, MIET is observable as a change of the radiative rate k_r. Similar to FRET, the energy transfer between the fluorophore and the metal depends on the orientation of the former. In solution, it is usually acceptable to assume that the free rotation of the flurophore's orientation is faster than its excited state lifetime. A detailed introduction into the theory behind MIET, starting from Maxwell's classical equations, is given by Karedla [107] and Ruhlandt [108].

Actually, it does not even need to be an electric dipol: Self-interference also has been demonstrated for acoustic dipols.[106]

In figure 2.10(a), an example of the distance-dependent contributions of the different excited-to-ground-state transition channels are shown. The resulting lifetime curve (figure 2.10(b)) has a steep rise within the first 100 nm. To determine the absolute height of a fluorophore above the surface, its lifetime is measured and converted using the distance-lifetime curve. This method has been employed to measure the height of the basal membrane of living cells of different types,[110] and was later extended to multiple colours.[111] In single molecule experiments, the position of individual molecules was determined with an axial localisation accuracy below 2.5 nm.[112] Using step-wise bleaching, multiple molecules on one nanostructure were co-localised axially.[109, 113] The axial resolution can be increased to the sub-nanometre range by utilising graphene instead of a metal film.[114, 115] Methods to determine the lifetime, which is needed in MIET experiments, are explained in the next section.

2.4 FLUORESCENCE SPECTROSCOPY

Fluorescence spectroscopy denotes a variety of methods to characterise the fluorescence emission of a sample, including spectra, polarisation, lifetime, and intensity fluctuations. In this thesis, the fluorescence lifetime τ, introduced in section 2.1, and its measurement on the single molecule level are essential.

After a fluorophore has been excited at time $t = 0$, the probability of finding it still in its excited state decays exponentially. The probability of fluorescence emission, being a first order process, is always proportional to the occupancy of the exited state and is described by

$$I(t) = I_0 \exp\left(-\frac{t}{\tau}\right). \tag{2.12}$$

As this is an exponential distribution, the average time $\langle t \rangle$ spent in the excited state as well as its standard deviation $\sqrt{\langle (t - \langle t \rangle)^2 \rangle}$ are equal to τ. This is sometimes used as fast lifetime estimator. In reality, fluorophores can exist in multiple states or experience different interactions with their environment causing a more complex excited-state decay behaviour and potentially a change of their quantum yields. Therefore, the fluorescence decay is often more accurately described by a weighted sum of exponential decays with different lifetime values.

To measure the fluorescence lifetime, a temporally modulated excitation is required. In frequency-domain techniques, the excitation is modulated sinusoidally. Both the phase shift and demodulation of the fluorescence signal are converted to a lifetime value. To disentangle a multi-experiential decay behaviour, the modulation frequency needs to be varied.[41, 116]

Time-correlated single-photon counting (TCSPC)

Time-domain techniques employ a pulsed excitation and record the fluorescence signal with a time resolution much smaller than the fluor-

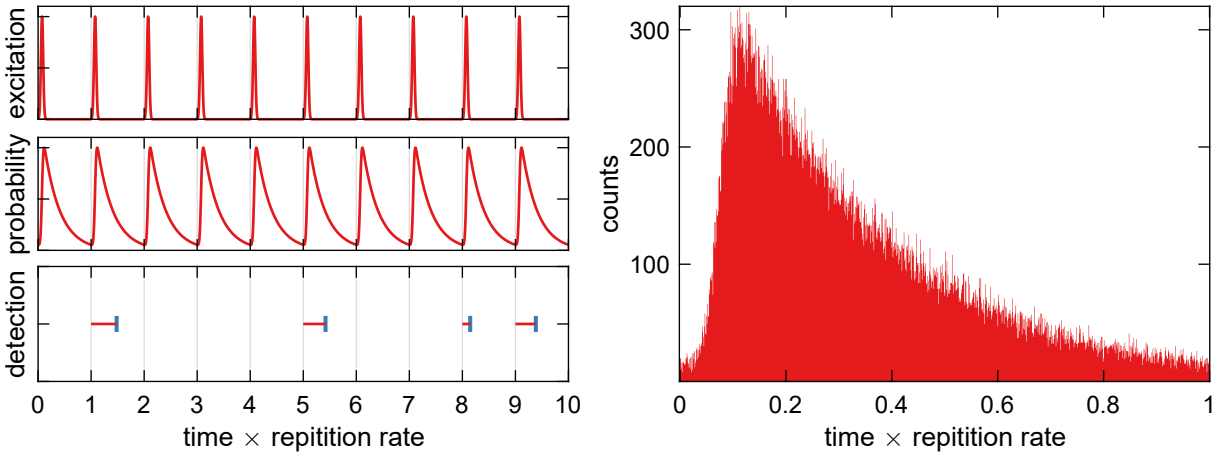

Figure 2.11: Schematic of TCSPC detection for lifetime measurements. The fluorophores are excited with a pulsed laser (top left). The probability of fluorescence emission is given by the convolution of the excitation with an exponential decay of the excited state (centre left). Whenever a photon is detected, indicated by a blue marker in the bottom left panel, the number of the cycle (macrotime) and the time since the sync signal (microtime) is recorded. The microtimes are illustrated by the short red horizontal lines and the sync signal by the grey vertical lines. On the right, a simulated histogram of the microtime of 10^5 photons is plotted.

escence lifetime one wants to measure. A common implementation of such a technique is *time-correlated single-photon counting* (TCSPC), schematically shown in figure 2.11. Fluorophores are excited with short ($\ll \tau$) laser pulses with a repetition period a few times longer than the lifetime. The emission probability is given by the convolution of the decay function of the fluorophore with the excitation pulses. When a fluorescence photon is detected, its arrival time is recorded on two timescales: the macrotime is the number of pulses since the start of the measurement, and the microtime is the time since the last sync signal. The sync signal is typically triggered by the excitation laser and synchronises the timing electronics with the excitation pluses. In most excitation cycles, no photon is detected.[117] This detection scheme, also known as time-tagged time-resolved (TTTR) detection due to its two timescales, is useful for many application including lifetime measurements, FCS, anti-bunching, photon counting histograms and more.

To determine the lifetime, a TCSPC histogram is constructed from the microtimes of the detected photons and is then fitted with an appropriate model. The model usually needs to include a background component caused by thermal noise, detector after-pulsing, or uncorrelated light. The shape of the excitation pulses, combined with the accuracy of the detection and timing electronics, determine the *instrument response function* (IRF). If the IRF is narrow compared to the lifetime, it is sufficient to consider only the tail of the TCSPC histogram starting a short time (cut-off time) after the maximum. However, such tail fitting does not use all the detected photons and does not retrieve the correct amplitudes for multi-exponential decays. To take the IRF into account, the calculated decay is convolved with the IRF before comparing it to the measured TCSPC histogram.

Similar to the fitting of PSF positions in SMLM, the TCSPC histogram is

best fitted with a *maximum likelihood estimator* (MLE) due to Poissionian statistics of the photon detections. Least square methods assume a Gaussian statistics and typically overestimate the background while underestimating the lifetime for measurements with low photon counts,[118] see section 5.2.2 for a comparison of different fitting approaches. When neglecting background, photon-detection shot noise limits the precision of the lifetime determination to $\tau/\sqrt{N}$.

Fluorescence lifetime spectroscopy is an important tool in FRET studies. By measuring the donor lifetime instead of only donor and acceptor intensities, a static mixture of different states can be disentangled from a dynamic conversion between states.[119]

Fluorescence-lifetime imaging microscopy

Fluorescence lifetime measurements can be done in a spatially resolved manner with a microscope, which is called *fluorescence-lifetime imaging microscopy* (FLIM). For wide-field detection, time-gated cameras with a varying time gate or special frequency-domain cameras can be used. As discussed in detail in chapter 4, wide-field lifetime cameras are, in general, not sensitive enough to detect single molecules. For single-molecule sensitive FLIM, typically confocal microscopes with pulsed excitation and TCSPC detection are employed. An exemplary setup is described in chapter 3.

FLIM adds the lifetime dimension to microscopy. By using specifically designed fluorophores, various parameters of the local environment can be determined non-invasively. With this local sensitivity, temperature, pH, ion concentration, viscosity, and various parameters of membranes (viscosity, order, potential) have been measured in living cells.[37, 120, 121]

MIET measurements discussed in section 2.3 employ FLIM to measure 3D maps and to axially localise single molecules. Due to the exceptional axial localisation precision of a few nanometres, the combination of MIET and FLIM can be considered an axial super-resolution technique.

Fluorescence correlation spectroscopy

In *fluorescence correlation spectroscopy* (FCS), fluorescence intensity fluctuations, observed from a tiny confocal detection volume, are analysed by calculating their temporal correlation. Because correlations can be accumulated over arbitrarily long times, even weak fluctuations can be detected. FCS is typically measured with a confocal microscope. Observed processes include the diffusion of molecules, or triplet state dynamics, but any process that dynamically changes the brightness of the fluorophore can be observed.[122] In combination with electron or energy transfer processes like PET or FRET, contact rates or distance fluctuations can be measured.[123, 124]

The FCS correlation curve $G_{\text{diff}}(t)$ of a freely diffusing species is given by

$$G_{\text{diff}}(t) = \frac{1}{N}\left(\frac{1}{1+t/\tau_{\text{diff}}}\right)\left(\frac{1}{1+\omega^2 t/\tau_{\text{diff}}}\right) \tag{2.13}$$

where N is the average number of molecules in the confocal volume, and ω is the aspect ratio (ratio of long axis to short transversal axis) of the confocal detection volume. The diffusion time depends on the lateral detection volume size s (distance where confocal detection efficiency has fallen off to e^{-2}) and is given by

$$\tau_{\text{diff}} = \frac{s^2}{4D} \tag{2.14}$$

with the diffusion coefficient D. An additional fast process that can be modelled as a two state system with fixed rates, such as triplet state dynamics, adds an exponential decay:

$$G(t) = G_{\text{diff}}(t) \left(1 + \frac{T}{1-T} \exp\left(-t/\tau_{\text{triplet}}\right)\right) \tag{2.15}$$

Here, T denotes the average fraction of molecules in the triplet state, and τ_{triplet} is the triplet lifetime.[41] In a uniform lateral flow, the dwell time of the molecules in the confocal volume is decreased by drift. This decrease modifies the correlation curve $G(t)$ to

$$G(t) = G_{\text{diff}}(t) \exp\left(-\left(t/\tau_{\text{flow}}\right)^2 N\, G_{\text{diff}}(t)\right) \tag{2.16}$$

with $\tau_{\text{flow}} = s/u$ and the flow velocity u.[125]

To observe processes slower than the diffusion-limited dwell time in the confocal volume, the molecules can be immobilised and then slowly scanned.[126] To model the corresponding correlation, the uniform scanning can be treated as a uniform flow without diffusion ($D = 0$).

CONFOCAL FLUORESCENCE-LIFETIME SINGLE-MOLECULE LOCALISATION MICROSCOPY

3

All single molecule localisation techniques introduced in chapter 2 are based on wide-field detection. Here, a method is presented that employs instead a confocal microscope with single photon detection to achieve super-resolved FLIM.
This chapter is based on the following publication:
Jan Christoph Thiele, Dominic A. Helmerich, Nazar Oleksiievets, Roman Tsukanov, Eugenia Butkevich, Markus Sauer, Oleksii Nevskyi, and Jörg Enderlein, 'Confocal Fluorescence-Lifetime Single-Molecule Localization Microscopy', *ACS Nano* 2020, 14, 10, pp. 14190–14200. 10.1021/acsnano.0c07322

Contribution In this project, I contributed to the design of the experiments, maintained the confocal setup and, together with Oleksii Nevskyi, performed the confocal SMLM measurements. I developed the software for data analysis, performed most of the analysis, and co-wrote the manuscript.

3.1 INTRODUCTION

Confocal laser-scanning microscopy (CLSM) is one of the most important microscopy techniques for biology and medicine. Its fundamental purpose is to provide so-called *optical sectioning* and to thus enable the recording of three-dimensional images, which is impossible to achieve with conventional wide-field microscopy. Its disadvantage, compared to wide-field microscopy, is its inherently slow image acquisition speed because the image formation is realised by sequentially scanning single or multiple foci over a sample. This also limits its overall light throughput (small dwell time per scan position), which is one reason why CLSM was nearly never used for single-molecule localisation based super-resolution microscopy (SMLM), such as *photoactivated localisation microscopy* (PALM),[29] (*direct*) *stochastic optical reconstruction microscopy* (dSTORM),[56, 89] or *points accumulation for imaging in nanoscale topography* (PAINT).[61, 127]

There are only a few exceptions, all using faster alternatives to a CLSM and a camera-based detection. One of them used a spinning-disk CLSM for PAINT, exploiting the superior out-of-plane light rejection of a CLSM that is so important for reducing background from freely diffusing dyes in PAINT.[128] Another method employed a spinning-disk CLSM for STORM with self-blinking dyes, where it was used for reducing excitation intensity.[59] A third method used a custom line-scan confocal microscope for dSTORM deep inside a sample.[129] Besides efficient out-of-plane signal rejection which enhances contrast and facilitates

deep-tissue imaging,[130] CLSM offers several additional advantages that make it attractive for SMLM. Firstly, single-focus CLSM uses single-point detectors which can be operated in single-photon counting mode (Geiger mode) and thus provides shot-noise limited detection, in contrast to emCCD or sCMOS cameras used in conventional wide-field SMLM that are affected by read-out, thermal, and electronic noise. Secondly, when using Geiger mode detectors for light detection, CLSM records the positions of single-photon detection events in a quasi-continuous, non-pixelated way, thus preventing pixel size from affecting the single-molecule localisation accuracy.[66] Thirdly, and most interestingly, it allows for measuring fluorescence lifetimes, thus allowing us to combine *fluorescence-lifetime imaging microscopy* (FLIM) with SMLM.

FLIM is widely used for lifetime-based FRET and environment sensing applications.[121, 131] Although single-molecule wide-field FLIM has been demonstrated recently, the implementation is still a trade-off between lifetime-resolution and acquisition speed.[132, 133]

In FLIM, the lifetime information introduces the option to co-localise different molecular species that differ only by their lifetime while having similar excitation and emission spectra,[134] thus efficiently circumventing all problems connected with chromatic aberration that trouble many multicolour SMLM methods.[77] Especially for state-of-the-art SMLM, which now routinely achieves a lateral resolution of only a few nanometres, chromatic aberration is a serious issue,[135] in particular when trying to study biological interactions or the relative arrangement of different cellular structures with respect to each other.

Several solutions to the chromatic aberration problem have been proposed in the past. For example, activation-based multicolour STORM entirely removes chromatic aberrations at the cost of relatively high crosstalk.[79] Recently, an aberration-free multicolour method of SMLM called spectral-demixing dSTORM was presented that is based on splitting the emission into two detection channels with different colours.[80, 81] This method works well for fluorophores showing good switching performance in the same imaging buffer. The fluorescence signal of the different molecules is separated spectrally, and ratiometric fluorescence measurements are used for spectral demixing and (co)localising different kinds of molecules. One step further in this direction was the implementation of spectrally resolved SMLM, where full spectra are measured and used for sorting of different molecules and their localisations.[82] A very fascinating approach is multicolour SMLM that combines PSF engineering with deep learning for identifying and sorting different molecular species without the need of spectrally resolved imaging.[136] In frequency-based multiplexing STORM/DNA-PAINT,[137] one uses frequency-encoded multiplexed excitation and colour-blind detection to circumvent chromatic-aberration problems. Another clever solution is exchange-PAINT,[86] which sequentially images different targets with the same dye but uses different DNA-tags for directing the dye to different targets decorated with complementary DNA-strands. Similarly, barcoding PAINT [87] exploits the different binding kinetics of imager and docking strands for distinguishing between different target sites. Because one uses the same dye for all the different struc-

tures, chromatic aberrations do not impact the SMLM results, but the prize is an increased image acquisition time, which is approximately linearly increasing with the number of different targets one wants to resolve. Finally, the recently introduced MINFLUX [73] allows for super-resolution imaging with a few nanometers accuracy and can be used for chromatic-aberration free multicolour imaging.[84] Similar to the confocal laser-scanning SMLM that is presented here, it is also based on scanning, but in an asynchronous manner, so that it can currently localise only one individual molecule at any time.

In this work, we present a realisation of SMLM with a time-resolved CLSM using *single-photon avalanche-diodes* (SPADs) for detection, and a rapid laser-scanning unit for excitation beam scanning. This unit enables us to record images with reasonable acquisition speed as required for efficient SMLM. Our approach combines all the advantages of CLSM with those of SMLM: axial sectioning, shot-noise limited single-photon detection, pixel-free continuous position data, and fluorescence lifetime information acquired by CLSM with the exceptional spatial resolution and single-molecule identification of SMLM. At first, we demonstrate the feasibility of using CLSM for fluorescence lifetime SMLM (FL-SMLM) by imaging labelled, fixed cell samples by combining CLSM with two of the most widely used variants of SMLM, dSTORM (for imaging microtubules in human mesenchymal stem cells) and DNA-PAINT (for imaging chromatin in COS-7 cells). To demonstrate the fluorescence lifetime multiplexing capability of FL-SMLM, we record images of polymer beads that are surface-labelled with two different dyes, and two cellular targets (microtubules and clathrin in COS-7 cells). Our results show that confocal laser-scanning FL-SMLM has great potential for many applications, extending the dimensions of fluorescence super-resolution microscopy by fluorescence lifetime.

3.2 METHODS

3.2.1 *Confocal Microscopy*

Fluorescence lifetime measurements were performed on a custom-built confocal setup. For the excitation a 640 nm 40 MHz pulsed diode laser (PDL 800-B driver with LDH-D-C-640 diode, PicoQuant) was utilised. The linear polarisation was converted to circular polarisation by a quarter-wave-plate in the excitation path. The laser beam was coupled into a single-mode fiber (PMC-460Si-3.0-NA012–3APC-150-P, Schäfter + Kirchhoff) with a fiber-coupler (60SMS-1-4-RGBV-11-47, Schäfter + Kirchhoff). After the fiber, the output beam was collimated by an air objective (UPlanSApo 10×/0.40 NA, Olympus). After passing thought a cleanup filter (MaxDiode 640/8, Semrock), an ultraflat quad-band dichroic mirror (ZT405/488/561/640rpc, Chroma) was used to direct the excitation light into a laser scanning system (FLIMbee, PicoQuant) and then into a custom side port of the microscope (IX73, Olympus). The three galvo mirrors in the scanning system were deflecting the beam

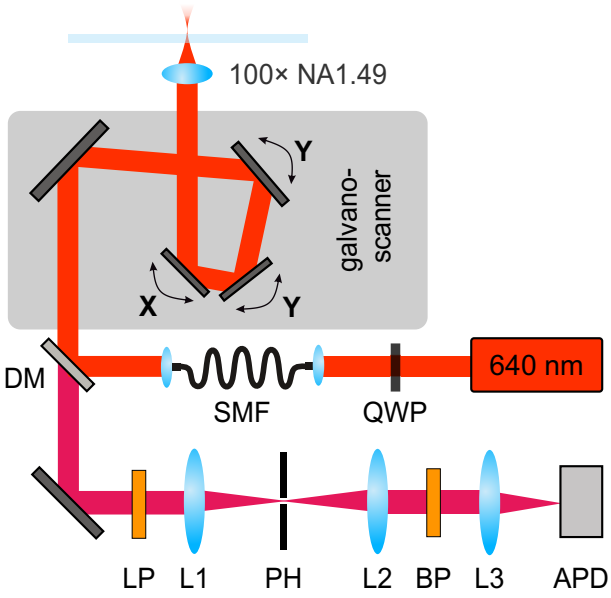

Figure 3.1: Schematic of the confocal setup: The pulsed 640 nm excitation light is converted to circular polarisation with a quarter wave plate (QWP), passes through a single mode fiber (SMF), is reflected by a dichroic mirror (DM) into a galvometeric laser scanner and focused by the objective. The collected fluorescent emission from the sample is descanned, passes the DM, and is focused on the pinhole (PH) then on the single-photon detector (APD) using the lenses (L1, L2 and L3). The long pass filter (LP) and the band-pass filter (BP) are blocking scattered excitation light. Adapted with permission from *ACS Nano* 2020, 10.1021/acsnano.0c07322. Copyright 2020 American Chemical Society.

while preserving the beam position in the back focal plane of the objective (UApo N 100×/1.49 NA oil, Olympus). The sample position was adjusted with a manual xy-stage (Olympus) and a z-piezo stage (Nano-ZL100, MadCityLabs). Emission fluorescence light was collected by the same objective and descanned in the scanning system. Subsequently, the achromatic lens (TTL180-A, Thorlabs) was used to focus the beam onto the pinhole (100 µm P100S, Thorlabs). The excitation laser light was blocked in the emission path by a long-pass filter (647 LP Edge Basic, Semrock). Then, the emission light was collimated by a 100 mm lens. A band-pass filter (BrightLine HC 679/41, Semrock) was used to reject scattered excitation light. Finally, the emission light was focused onto a single-photon avalanche-diode (SPAD)-detector (SPCM-AQRH, Excelitas) with an achromatic lens (AC254–030-A-ML, Thorlabs). The output signal of the photon detector was recorded by a TCSPC system (HydraHarp 400, PicoQuant) which was synchronised with the triggering signal from the excitation laser. Measurements were acquired with the software (SymPhoTime 64, PicoQuant), which controlled both the TCSPC system and the scanner system. Typically, 100 000 sample scans with a virtual pixel size of 100 nm, a dwell time of 2.5 µs/pixel, and a TCSPC time resolution of 16 ps were recorded.

To evaluate the performance of the laser scanner, TetraSpeck microspheres were measured with the same parameters as used in the dSTORM measurements (10×10 µm region of interest, 100 nm pixel size

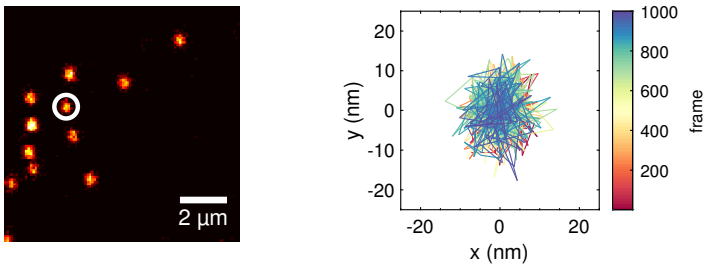

(a) first frame (b) track of single bead

Figure 3.2: Scanning confocal measurement of TetraSpeck microspheres. (a) First frame of the stack. (b) Drift corrected position of the highlighted bead. Adapted with permission from *ACS Nano* 2020, 10.1021/acsnano.0c07322. Copyright 2020 American Chemical Society.

and 2.5 µs dwell time). For the evaluation, 10 scans were binned to one frame in the same fashion as for the dSTORM measurement. For the analysis, the spheres were independently localised in each frame with TrackNTrace. The lateral drift was corrected by subtracting the moving average over 100 frames of the centre of gravity of all localisations. Figure 3.2 shows the sample (a) and an exemplary track (b). The average standard deviation of the tracks was 4.0 nm in x and 5.2 nm in y. Thus, the standard deviation along the fast scanning axis (x) was slightly lower than along the slow axis (y).

3.2.2 *Wide-Field Microscopy*

Measurements were performed with the same custom-built optical setup used in chapter 4 and described in section 4.2.1. However, a different laser and only the emCCD camera were used.

The excitation was performed with a 638 nm, continuous-wave laser (PhoxX+ 638-150, Omicron). The laser beam was coupled into a single-mode optical fiber (P1-460B-FC-2, Thorlabs) with a typical coupling efficiency of 50 %. The collimated laser beam was expanded by a factor of ~3.6× with telescope lenses after the fiber. The beam was focused onto the back focal plane of the TIRF objective (UApo N 100×/1.49 NA oil, Olympus) using an achromatic lens ($f = 200$ mm, AC508-200-A-ML, Thorlabs). Switching between the *epi* and *total internal reflection* (TIR) illumination schemes was achieved by mechanical shifting of the beam with respect to the objective lens using a translation stage (LNR50M, Thorlabs). Fluorescence emission light was collected using the same objective lens. Samples were placed onto the xy-translation stage (M-406, Newport). An independent one-dimensional translation stage (LNR25/M, Thorlabs) was equipped with a differential micrometer screw (DRV3, Thorlabs) for focusing by movement of the objective lens. Emission fluorescence light was spectrally decoupled from the scattered excitation laser light using a multiband dichroic mirror (Di03

R405/488/532/635, Semrock) and a band-pass filter (BrightLine HC 692/40, Semrock). With the tube lens (AC254–200-A-ML, Thorlabs), an image plane was formed on an adjustable slit aperture (SP60, OWIS). The latter was employed to select a region of interest within the field of view. Two Lenses (AC254-100-A, Thorlabs) and (AC508–150-A-ML, Thorlabs) were used to form the image the on an emCCD camera (iXon Ultra 897, Andor). The total magnification for imaging was 166.6×, resulting in an effective pixel size in sample space of 103.5 nm.

Image stacks of 20000 frames were acquired with an exposure time of 10 ms. The recorded images then were analysed with the ImageJ plugin ThunderSTORM [138] for determining the positions of single emitters. In all the experiments, the same localisation parameters were used for super-resolution image reconstruction. Localisations containing more than 500 photons and less than 5000 photons were taken into account.

3.2.3 *dSTORM Imaging*

For wide-field/confocal dSTORM imaging of samples solely labelled with Alexa 647, an enzymatic oxygen scavenging buffer (GLOX, 0.5 mg/mL glucose oxidase, 40 µg/mL catalase, 10 % w/v glucose in PBS pH 7.4) with addition of thiol (20 mM β-mercaptoethylamine, MEA) was used. For multiplexed confocal dSTORM imaging of beads, a switching buffer containing only 5 mM MEA in PBS was used. Multiplexed confocal dSTORM imaging of fixed cells was performed in a switching buffer containing 5 mM MEA in D_2O.

3.2.4 *Points Accumulation for Imaging in Nanoscale Topography (PAINT) Imaging*

The DNA docking strands (Biomers GmbH, Ulm, Germany) were functionalised with an azide group at the 5′-terminus. The coupling of the docking strands to unconjugated nanobodies FluoTag-Q anti-TagBFP (NanoTag Biotechnologies GmbH, Göttingen, Germany, Cat. No: N0501) was performed according to the procedure described by Schlichthärle and co-workers.[139] The imager strand (Eurofins Genomics) was labelled with Atto 655 fluorophore at the 3′-terminus. It was aliquoted in TE buffer (Tris 10 mM, EDTA 1 mM, pH 8.0) at a concentration of 1 µM and stored at −20 °C. Prior to the experiment, the strands were diluted to the final concentration of 0.25 nM in PBS buffer, containing 500 mM NaCl. The imager strand solution in PBS (500 µL) was added to the sample chamber and incubated for 5 min before the acquisition. The following acquisition settings were used: area 20 × 20 µm, virtual pixel size 100 nm, dwell time 2.5 s/pixel and a TCSPC time resolution 16 ps. Ten scans were combined as for the dSTORM measurements and analysed by the TrackNTrace software.

Table 3.1: DNA sequences and their modifications

name	sequence 5′ → 3′	5′ modification	3′ modification
bead strand 1	GCAGCCACAACGTCTATCATCGATT	–	Alexa 647 / Atto 655
bead strand 2	AATCGATGATAGACGTTGTGGCTGC	biotin	–
PAINT imager	GTAATGAAGA	–	Atto 655
PAINT docking	TCTTCATTAC	nanobody	–

3.2.5 *Polymer Beads Labelling*

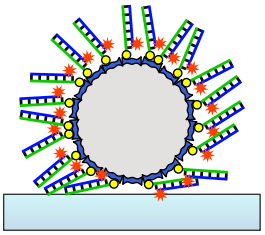

Figure 3.3: Schematic of the surface labelled beads.

The preparation of surface labelled polystyrene microspheres employed a similar approach to the single molecule surface immobilisation in section 4.2.3. Polystyrene microspheres ($d = 3.0 - 3.9\,\mu m$), coated with streptavidin (Kisker Biotech, PC-S-3.0), were labelled with a fluorescent dye according to the following procedure: 500 µL of water, 500 µL of PBS, 100 µL of microsphere solution, and 0.5 µL of biotinylated dsDNA labelled with either Alexa 647 (1 mM in PBS) or Atto 655 (1 mM in PBS) were mixed and centrifuged for 30 min at 15 krpm. The DNA sequences are listed in table 3.1. The supernatant was then removed and replaced with 100 µL of PBS, and the pellet was dissolved by vortexing. A 50 µL portion of the final solution was placed on a cover glass and incubated for 20 min, protected from light and evaporation. Finally, 300 µL of dSTORM imaging buffer were added.

3.2.6 *Antibody Labelling*

The antibodies for the multiplexed dSTORM measurements were custom modified and labelled. Goat-antirabbit IgG (Invitrogen, 31212) was used as secondary antibody for alpha-tubulin and clathrin samples. Goat-antimouse IgG (Sigma-Aldrich, SAB3701063–1) was used as secondary antibody for beta-tubulin staining. Antibody labelling *via* *N*-hydroxysuccinimidyl esters was performed at RT for 4 h in labelling buffer (100 mM sodium tetraborat, Fluka 71999, pH 9.5), following the manufacturers standard protocol. Briefly, 100 µg antibody was reconstituted in labelling buffer using 0.5 mL spin-desalting columns (40K MWCO, ThermoFisher, 87766). Goat-antirabbit IgG (Invitrogen, 31212) was modified with *N*-hydroxysuccinimidyl ester–PEG4–*trans*-cyclooctene (JenaBioscience, CLK-A137-10), using a 5× excess of NHS-PEG4-TCO. After purification by spin-desalting columns (40K MWCO) in PBS (Sigma-Aldrich, D8537-500 ML), modified goat-antirabbit IgG (Invitrogen, 312121) was incubated with a 10× excess of Tetrazine-Atto655 (ATTO-TEC, AD 655–2505) at RT and purified again after 15 min. Goat-antimouse IgG was incubated with a 5× excess of *N*-hydroxysuccinimidyl ester–Alexa647 (LifeTech, A20106) for 4 h and purified using spin-desalting columns (40K MWCO) in PBS (Sigma-Aldrich, D8537-500 ML) to remove excess dyes. Finally, antibody con-

centration and degree of labelling (DOL) were determined by UV–vis absorption spectrometry (JASCO V-650).

3.2.7 *Cell Culture and Fluorescence Labelling*

Human mesenchymal stem cells (PT-2501), used for proof-of-principle dSTORM imaging, were purchased from Lonza Group. Cells were plated on glass-bottom Petri dishes (VWR) and cultured in DMEM supplemented with 10 % FCS, 2 mM L-glutamine, 1 mM sodium pyruvate, 100 U/mL penicillin–streptomycin in a humidified 5 % CO_2 atmosphere at 37 °C. 48 h after plating, cells were rinsed with PBS and fixed in 4 % (v/v) paraformaldehyde/PBS for 15 min. After that, they were permeabilised with 0.5 % Triton-X 100 in PBS for 10 min. For labelling of tubulin, permeabilised cells were incubated with blocking solution (3 % BSA in PBS) for 30 min at room temperature and then incubated with monoclonal mouse-antialpha-tubulin antibody (T6199, clone DM1A, Sigma-Aldrich) diluted at 1:200 in 3 % (w/v) BSA/PBS for 1 h. Cells were washed with PBS containing 0.005 % Triton X-100, incubated 1 h with Alexa Fluor 647-conjugated cross-adsorbed goat-antimouse IgG F(ab')2 (A-21237, Invitrogen), diluted at 1:1000 in 3 % BSA/PBS, and washed with PBS.

COS-7 cells, used for DNA-PAINT measurements, were transfected and immunostained as described previously.[140] Prior to immunostaining *ca.* 20 000 cells/chamber were plated in 8 chambered cover glass (155411PK, Thermo Fisher Scientific). Fixed cells were stored in PBS at 4 °C.

COS-7 cells, used for lifetime-based multiplexed dSTORM imaging, were seeded at a concentration of 2.5×10^4 cells/well into 8 chambered cover glass systems with high performance cover glasses (Cellvis, C8-1.5H-N), and immunostained after 3 h of incubation at 37 °C and 5 % CO_2. For microtubule and clathrin immunostaining, cells were washed with prewarmed (37 °C) PBS (Sigma-Aldrich, D8537-500 ML) and permeabilised for 2 min with 0.3 % glutaraldehyde (GA) + 0.25 % Triton X-100 (EMS, 16220 and ThermoFisher, 28314) in prewarmed (37 °C) cytoskeleton buffer (CB), consisting of 10 mM MES ((Sigma-Aldrich, M8250), pH 6.1), 150 mM NaCl (Sigma-Aldrich, 55886), 5 mM EGTA (Sigma-Aldrich, 03777), 5 mM glucose (Sigma-Aldrich, G7021) and 5 mM $MgCl_2$ (Sigma-Aldrich, M9272). After the permeabilisation, cells were fixed with a prewarmed (37 °C) solution of 2 % GA for 10 min. Cells were washed twice with PBS. After fixation, samples were treated with 0.1 % sodium borohydride (Sigma-Aldrich, 71320) in PBS for 7 min. Cells were washed three times with PBS before blocking with 5 % BSA (Roth, no. 3737.3) in PBS for 30 min. Subsequently, microtubule samples were incubated with 2 ng/µL rabbit-anti-alpha-tubulin primary antibody (Abcam, no. ab18251) or 2 ng/µL mouse-anti-beta-tubulin primary antibody (Sigma-Aldrich, T8328), the clathrin samples were incubated with 2 ng/µL rabbit-anticlathrin primary antibody (Abcam, no. ab21679) in blocking buffer for 1 h. After incubation, cells were rinsed with PBS and washed twice with 0.1 % Tween20 (ThermoFisher,

28320) in PBS for 5 min. Cells were incubated with 4 ng/µL of custom labelled goat-antirabbit IgG-PEG4-Atto655 (DOL 1.7) secondary antibodies (Invitrogen, 31212) or custom labelled goat-antimouse IgG-Alexa647 (DOL 1.1) secondary antibodies (Sigma-Aldrich, SAB3701063-1) in blocking buffer. After secondary antibody incubation, cells were rinsed with PBS and washed twice with 0.1 % Tween20 in PBS for 5 min. After washing, cells were fixed with 4 % formaldehyde (Sigma-Aldrich, F8775) for 15 min and washed three times with PBS.

3.2.8 *Data Analysis with TrackNTrace*

The data analysis was performed with the extended version of TrackNTrace,[141] described in detail in chapter 5. For the dSTORM/PAINT data analysis, the following plugins and parameters were used: Artefacts from bidirectional scanning were compensated by enabling the automatic correction in the PTU file import plugin. The candidate detection and refinement were performed with the Cross correlation and TNT Fitter plugin using the default parameters. The localisations were tracked with the TNT NearestNeighbor plugin a minimum track length of 1 frame, a maximum tracking radius of 1 pixel, and no gap closing. The lifetime fitting was performed with the plugin fit lifetime. First, the position of each localisation was refitted in a sum image of each frame of the track using a Gaussian MLE fit. For the TCSPC extraction, a mask radius of 2× the PSF size σ_{PSF} and summing over all frames of the track was chosen. The lifetime was fitted for all TCSPC histograms with at least 100 photons, using the monoexponential MLE with a cutoff of 0.3 ns, a lifetime range of 0.5 – 5.5 ns, and 100 fit attempts. For super-resolved FLIM images, the localisations were filtered and only localisations with a χ^2 of the lifetime fit between 0.9 and 1.1 were selected for the final reconstruction with a Gaussian PSF ($\sigma = 10\,\text{nm}$).

3.2.9 *Pattern Matching Analysis*

Our pattern matching classification is a Bayesian model comparison, assuming equal prior probabilities for all species.[142] It is based on a maximum likelihood approach, previously applied to burst analysis of diffusing single molecules.[21] The analysis relies on the full TCSPC curve of each localisation given by $\{m(n)\}$ with m denoting the number of photons in time bin n. The probability P of obtaining $\{m(n)\}$, provided that the localisation is of species α, is given by

$$P_\alpha\{m(n)\} = M! \prod_{n=1}^{N} \frac{(p_\alpha(n))^{m(n)}}{m(n)!}, \tag{3.1}$$

where N is the number of time bins, $M = \sum_{n=1}^{N} m(n)$, and $p_\alpha(n)$ is the normalised probability distribution of species α. After this is computed for all considered species, a molecule is classified as belonging to the species with the highest probability. To make the calculation more

The largest factorial that can be stored in a double precision floating point number with 10 bit encoding the exponent is 170!

efficient, the logarithm of P is used and the term $M!$ and $m(n)!$ are, due to their independence of α, treated as constant:

$$Q_\alpha\{m(n)\} = \ln P_\alpha\{m(n)\} - \text{const} = \sum_{n=1}^{N} m(n) \ln p_\alpha(n) \tag{3.2}$$

The relative probability f_α of species α is given by

$$\begin{aligned} f_\alpha &= \frac{P_\alpha\{m(n)\}}{\sum_{\beta=1}^{A} P_\beta\{m(n)\}} = \frac{\exp Q_\alpha\{m(n)\}}{\sum_{\beta=1}^{A} \exp Q_\beta\{m(n)\}} \\ &= \frac{1}{\sum_{\beta=1}^{A} \exp\left(Q_\beta\{m(n)\} - Q_\alpha\{m(n)\}\right)}, \end{aligned} \tag{3.3}$$

provided that a number of A species are considered. This relative probability f_α corresponds to the posterior probability of the model for species α in the Bayesian sense and can be used to reject localisations that cannot be classified with sufficiently high likelihood. Unlike the often used Bayes factor, probabilities can be averaged over multiple localisations, enabling the reconstruction of probability maps. A prerequisite for pattern matching is the knowledge of the separate TCSPC curves of each species as references $p_\alpha(n)$. These were obtained by measuring a sample including only one species under the same conditions, summing the TCSPC histograms of all localisations, and normalising. The localisations were filtered based on their fitted Gaussian PSF and rejected if its standard deviation was not between 110 and 190 nm.

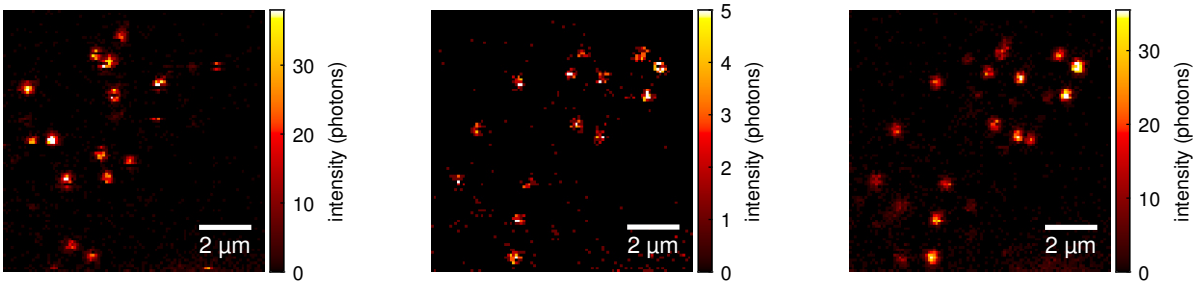

(a) 2.7 Hz, no frame binning (b) 27 Hz, no frame binning (c) 27 Hz, 10× frame binning

Figure 3.4: Single frame from a measurement of the same ROI at a scanning frame rate of (a) 2.7 Hz and (b,c) 27 Hz. In (c), 10 subsequent scans were summed (binned) to create one frame. The intensity scale in each panel was adjusted to cover 0 to the 0.999 quantile. Sample: Alexa 647 labelled β-tubulin (COS-7 cell) in D_2O with 20 mM MEA.

3.3 RESULTS & DISCUSSION

Confocal laser-scanning SMLM measurements were carried out on a custom-built, time-resolved confocal microscope, equipped with a fast laser scanner, as described in section 3.2.1. For dSTORM measurements, a region of interest of 10 × 10 µm was scanned with an image scan rate of ∼27 Hz. For excitation a pulsed laser with 640 nm wavelength, a repetition rate of 40 MHz, and a pulse width of ∼50 ps was employed. Single fluorescence photons were detected with a single-photon avalanche-diode (SPAD), and photon detection events were correlated in time to excitation pulses (time-correlated single-photon counting or TCSPC) with high-speed electronics. For data analysis, the recorded photons were converted into a stack of intensity images, always combining 10 subsequent scans into one image to minimise distortions from switching events during scanning. As shown in figure 3.4, slow scanning leads to many incomplete PSFs, whereas fast scanning without frame binning does not provide enough photons for precise localisation. Only the combination of fast scanning and frame binning results in complete PSFs with sufficient brightness. The stack of intensity images is then used to localise single molecules and to identify switching events. These localisations were subsequently reconstructed to obtain a super-resolved image (similar to conventional wide-field dSTORM). Taking full advantage of our TCSPC detection, fluorescence lifetimes of each localised molecule were determined by pooling all photons associated with it and fitting the resulting lifetime histogram with a monoexponential decay function. To increase the number of photons per localisation, identical localisations in subsequent frames were merged. Using this lifetime information, super-resolved fluorescence lifetime images were reconstructed.

To make the data analysis for confocal laser-scanning FL-SMLM widely available, the complete data processing pipeline was integrated into a Matlab-based graphical user interface (GUI) app. This app builds on the existing open-source framework TrackNTrace [141] and was now

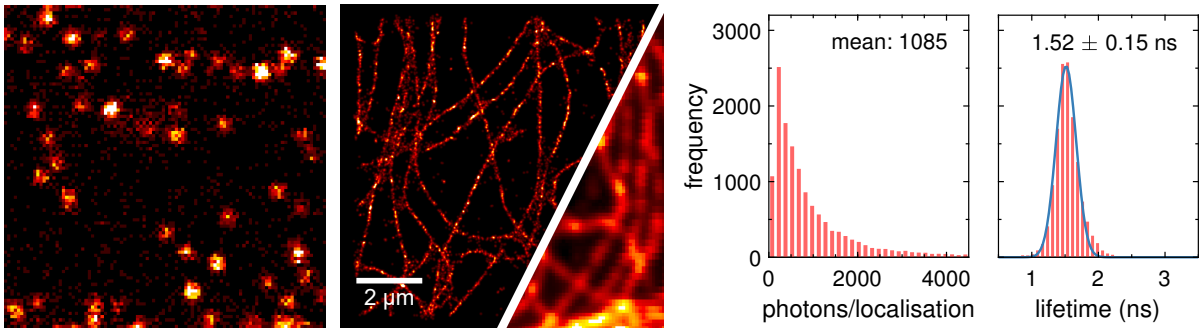

(a) single frame (b) reconstruction / confocal (c) number of photons (d) lifetime

Figure 3.5: Confocal laser-scanning dSTORM images of microtubules in hMS cells labelled with Alexa 647. (a) Example of a single frame during acquisition. (b) Corresponding super-resolved and diffraction-limited images. (c) Number of photons and (d) lifetime histograms, based on individual single-molecule localisations.

extended to process TCSPC data. The app supports FLIM data and comes with a dedicated plugin that pools photon detections for each localised molecule and executes lifetime fits. The data visualiser offers filtering of localisations, drift correction with *redundant cross-correlation* (RCC),[143] and reconstruction of super-resolved lifetime images. A detailed description can be found in chapter 5.

3.3.1 *Confocal dSTORM*

To demonstrate the applicability of confocal laser-scanning SMLM to biological samples, we performed dSTORM on microtubules in fixed, immunolabelled hMS cells. Alexa 647 is a benchmark dye for dSTORM, due to its outstanding photostability, brightness, and optimised blinking behavior. The key properties are the high number of photons per switching event (typically ∼4000 photons in wide-field imaging), and the possibility to tune the switching kinetics through the composition of the imaging buffer and a suitable adjustment of excitation power (typical on-time is 10 ms in wide-field imaging).[144] Conventional confocal laser-scanning dSTORM and CLSM images are presented in figure 3.5(b). A Gaussian fit of the fluorescence lifetime histogram obtained from the fitted lifetime values of all identified molecules in the region of interest gives a mean value of 1.52 ns for the fluorescence lifetime of Alexa 647-labelled antibodies, which is in agreement with literature data.[145] Moreover, the width of the obtained lifetime distribution (see figure 3.5(d)) is close to being shot-noise limited, so that multiplexing by fluorescence lifetime seems a very promising prospect for FL-SMLM. The average number of detected photons per switching cycle was 1085 photons (see figure 3.5(c)), which is lower than for imaging with a wide-field setup.[144] We attribute this lower photon count to light losses in the detection pathway (due to dichroic mirrors, pinhole and emission filters).

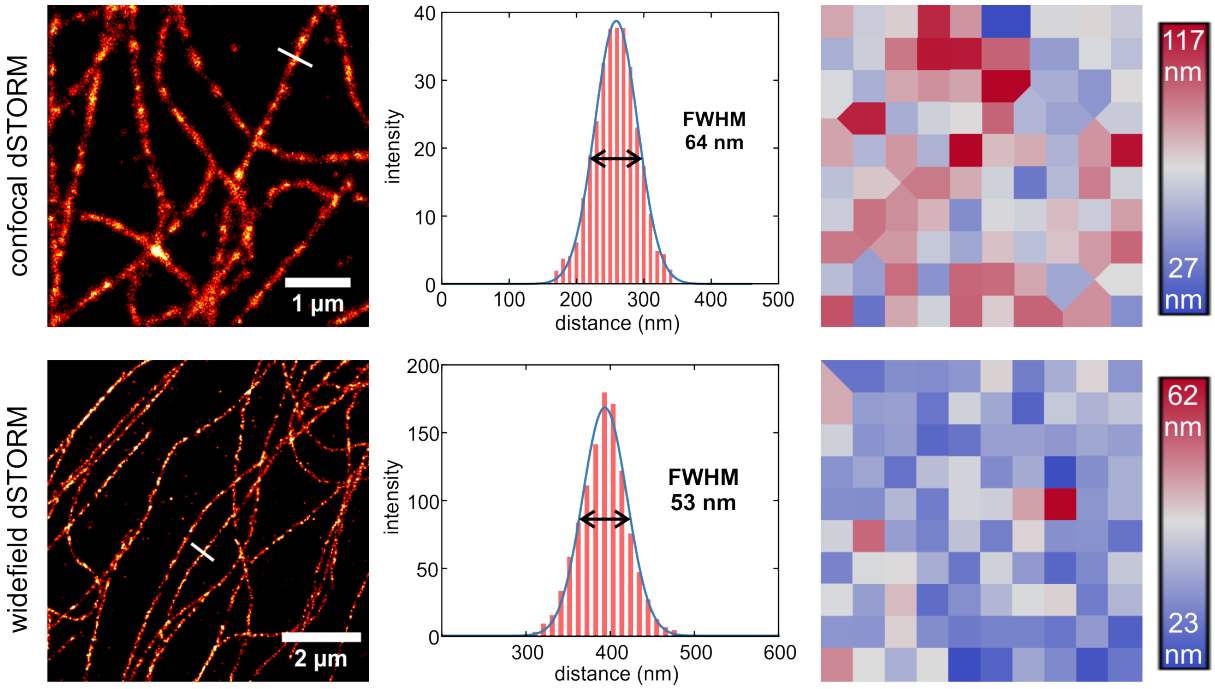

Figure 3.6: Comparison of confocal dSTORM (top row) and conventional, wide-field dSTORM (bottom row. Super-resolved Reconstruction (left) and line profile across a single microtubule (middle). The FRC map of the corresponding region (right) was generate with NanoJ-SQUIRREL.[146] Adapted with permission from *ACS Nano* 2020, 10.1021/acsnano.0c07322. Copyright 2020 American Chemical Society.

To better compare the performance of confocal laser-scanning dSTORM with conventional wide-field dSTORM, we imaged the same sample that we used for FL-SMLM with a custom-built wide-field setup. The comparison is shown in figure 3.6. To quantify the relative performance of both techniques, we determined single microtubule cross sections, and we estimated their diameter to be 64 nm full width at half maximum (FWHM) for confocal laser-scanning dSTORM, and 53 nm FWHM for conventional wide-field dSTORM. The apparent size of the microtubules in both cases is larger than their actual value, which we attribute to the size of the secondary immunolabels. We calculated *Fourier ring correlation* (FRC) maps using the NanoJ-SQUIRREL plugin (see figure 3.6),[146] and found that the average resolution for both images was 50 and 48 nm for confocal laser-scanning dSTORM and conventional wide-field dSTORM, respectively. The localisation precision was estimated with a modified Mortensen's equation [66, 67, 147] to be, on average, 8.6 and 9.2 nm, respectively. In summary, we find that both approaches show a similar performance, which demonstrates that confocal laser-scanning dSTORM is a promising and versatile super-resolution technique, adding the important fluorescence lifetime dimension to the picture. Furthermore, the sectioning capabilities of the confocal imaging system offer the possibility to image dense 3D structures. To illustrate this, we recorded a z-stack of images of Alexa 647 labelled tubulin in fixed COS-7 cells (see figure 3.7).

In a typical measurement, a $10 \times 10\,\mu m$ area was scanned 100 000 times with an image scan rate of $\sim$27 Hz, leading to a measurement

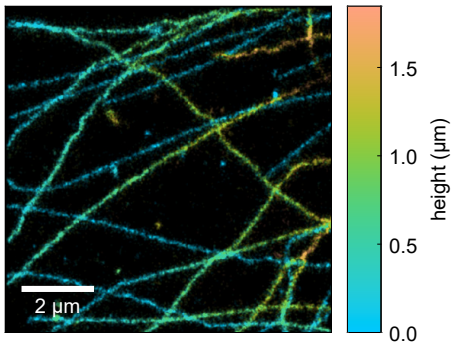

Figure 3.7: Confocal sectioning. 3D dSTORM image of Alexa647 labelled microtubules in fixed COS-7 cells. The localisations are colour-coded according to their z-position. The image was generated from a 2.1 µm z-stack with a step size of 300 nm.

time of *ca.* 1 h. As shown in figure 3.8, a shorter measurement can be sufficient for well performing fluorophores like Alexa 647.

3.3.2 *Confocal DNA-PAINT*

We applied confocal laser-scanning to DNA-PAINT which is a recently developed alternative to dSTORM. DNA-PAINT circumvents the inherent photobleaching limitations of dSTORM by labelling the targets of interest with single stranded docking DNA-strands and employing complementary, dye-labelled imager DNA-strands that reversibly bind to the docking DNA-strands. For DNA-PAINT (and PAINT in general), optical sectioning is critical to efficiently suppress fluorescent background from freely diffusing imager strands. To demonstrate confocal laser-scanning DNA-PAINT, we imaged histone H2B, which is part of chromatin, in COS-7 cells (figure 3.9). For this, H2B was fused to mTagBFP which was subsequently labelled with docking DNA-strands by FluoTag-Q anti-TagBFP nanobodies.[140] Using nanobodies for labelling minimises the distance between dye and target, thus significantly reduces so-called linkage errors and thereby increases localisation accuracy. Atto 655 was used for DNA-PAINT because of its high brightness and low unspecific binding to both, cover glass surface and cell organelles. Although we reduced the concentration of imager strands by an order of magnitude (to 0.25 nM), as compared to conventional DNA-PAINT,[86] we registered a sufficiently large number of single-molecule localisations due to the dense packing of histone targets inside the nucleus. A typical single frame from a recorded movie is shown in figure 3.9(a), and the corresponding super-resolved reconstruction is shown in figure 3.9(b). A comparison with conventional, wide-field DNA-PAINT is given in figure 3.10. The average localisation precisions were 18 and 26 nm for confocal DNA-PAINT and conventional DNA-PAINT, respectively. The FRC maps had average resolutions of 45 and 41 nm, respectively.

The corresponding lifetime distribution for all localised molecules is shown in figure 3.9(d). The average lifetime of Atto 655 was longer than

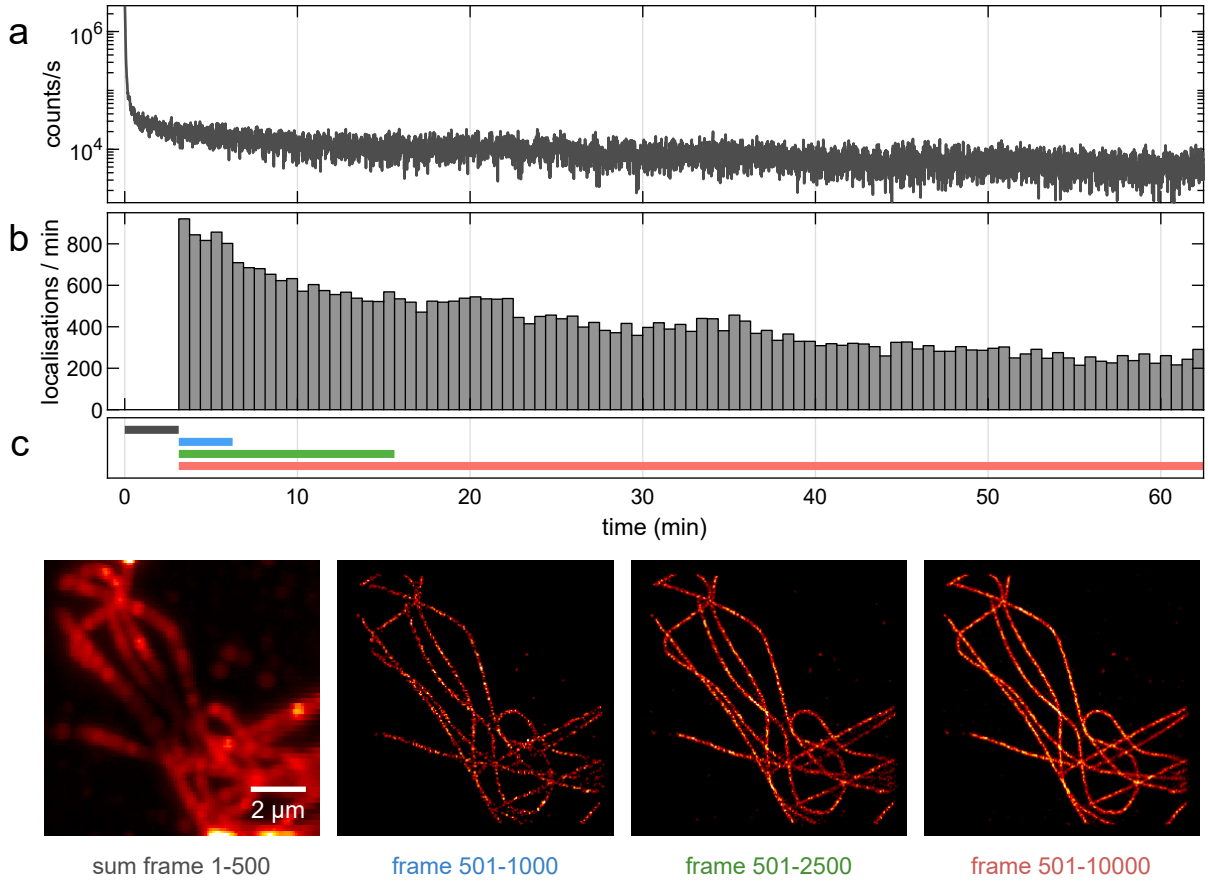

Figure 3.8: Reconstructions for different dSTORM measuring durations, evolution of count rate and number of localisations over time. (a) Photon count rate over the course of the measurement. (b) Number of localisations over time. During the first several minutes, the fluorophores are switched off. Therefore, the first 500 frames are excluded from further analysis. (c) Sum of the first 500 frames and reconstructions including localisations from an increasing number of frames. The intensity scale in each panel was adjusted to cover the 0 to 0.999 quantile. Sample: Alexa 647 labelled β-tubulin (COS-7 cell) in D_2O with 20 mM MEA, analysed with 10× frame binning.

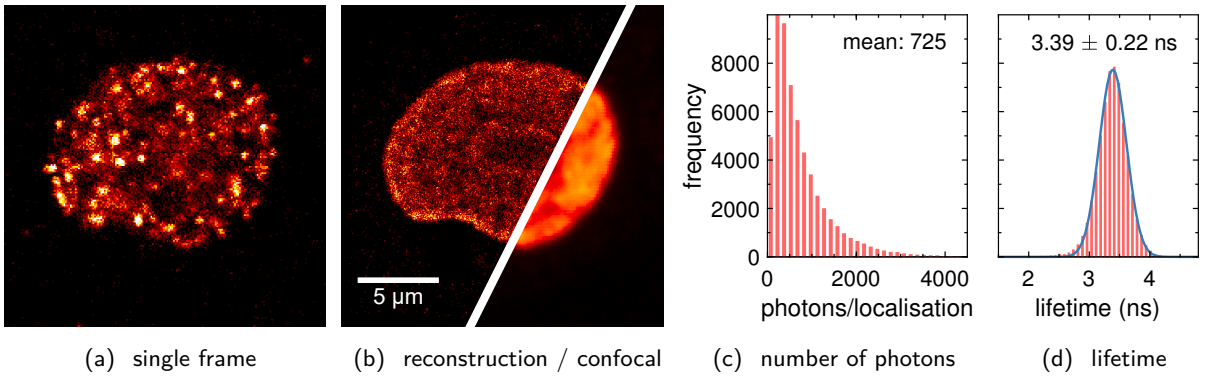

Figure 3.9: Confocal laser-scanning DNA-PAINT imaging of chromatin in COS-7 cells, utilising DNA-labelled Atto 655. Imaging was performed at a height of ∼6 µm above the cover glass surface. (a) Example of a single frame during acquisition. (b) Corresponding super-resolved and diffraction-limited images. (c) Number of photons and (d) lifetime histograms, based on individual single-molecule localisations.

the value reported for free dye, which we attribute to its conjugation to single-stranded imager DNA and the environment inside the nucleus. This trend was also observed in solution measurements: while non-conjugated Atto 655 had a lifetime of (1.83 ± 0.01) ns, the lifetime increased to (2.69 ± 0.01) ns when bound to DNA and to (3.44 ± 0.30) ns when attached to its complementary docking strand inside the nucleus. This confirms the sensitivity of Atto 655 for its local environment.[148]

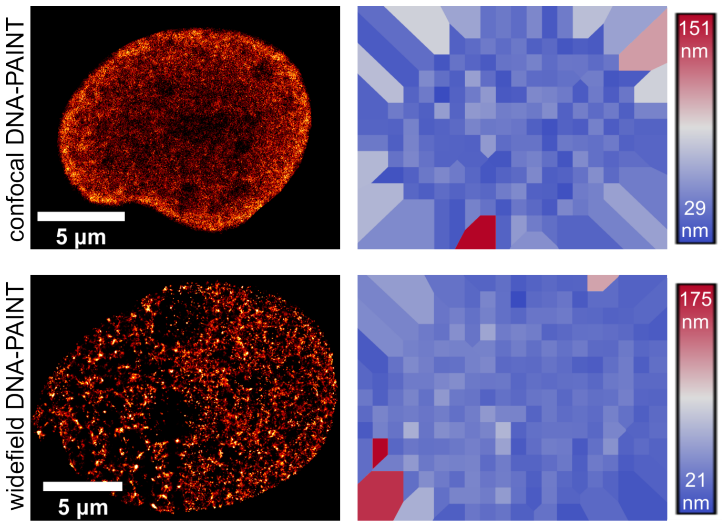

Figure 3.10: Comparison of confocal DNA-PAINT (top row) and conventional, wide-field DNA-PAINT (bottom row). Super-resolved reconstruction (left) of chromatin in COS-7 cells. The FRC map of the corresponding region (right) was generated with NanoJ-SQUIRREL.[146] Adapted with permission from *ACS Nano* 2020, 10.1021/acsnano.0c07322. Copyright 2020 American Chemical Society.

3.3.3 *Multiplexed confocal dSTORM*

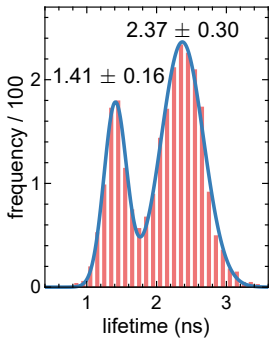

Figure 3.12: Lifetimes histogram for the localisations in figure 3.11.

To demonstrate the sectioning as well as multiplexing capabilities of confocal laser-scanning SMLM, we imaged polymer beads ($\varnothing$ 3 µm), labelled with two different fluorophores (Alexa 647 and Atto 655), each bound to DNA. On our wide-field microscope, we could not detect single switching events when focusing on the centre of the beads. In contrast, it was possible to localise switching molecules (figure 3.11a) with CLSM, to determine their fluorescence lifetimes, and to reconstruct a fluorescence-lifetime dSTORM image (figure 3.11c). The image shows two beads that are labelled with two different dyes, namely Alexa 647, having an average fluorescent lifetime of 1.4 ns, and Atto 655 with 2.4 ns. The resulting lifetime histogram (figure 3.12) has two distinct maxima.

To enable fluorescence-lifetime multiplexing dSTORM, it is crucial to use buffer conditions which are compatible with all fluorophores. This includes control over appropriate on- and off-switching rates while guaranteeing high dye brightness. Typically, a primary thiol is used to enhance off-switching rates. The standard buffer for Alexa 647 additionally contains GLOX to create an oxygen-depleted environment which

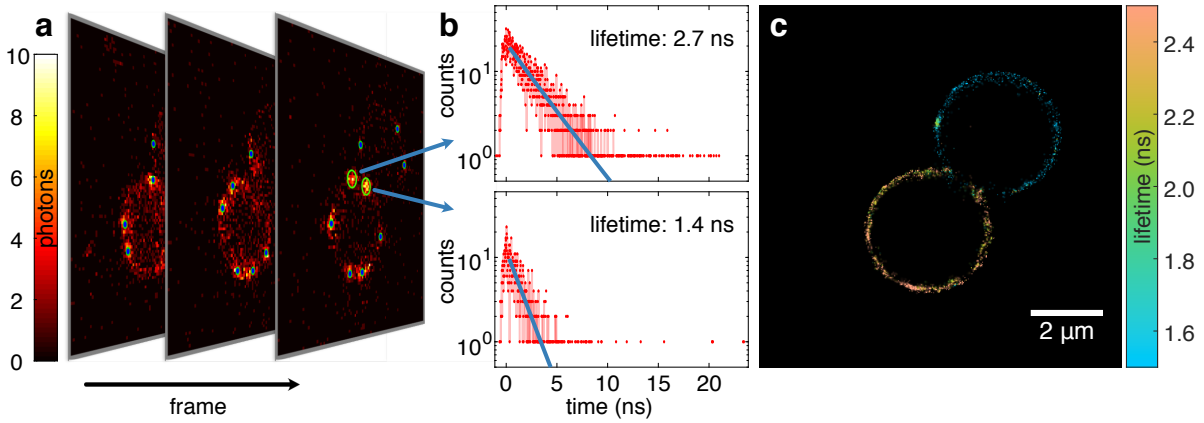

Figure 3.11: Lifetime-based multiplexed dSTORM imaging of polymer beads labelled with two different dyes. (a) Typical frames from a recorded movie including single-molecule localisations. (b) Histogram of photon arrival times (TCSPCs) for two indicated localisations. Lifetime is determined with a monoexponential fit (blue line). (c) Super-resolved image reconstruction including lifetime information. The two different lifetime values for molecules on both beads reveal that the beads are labelled with different fluorophores (Alexa 647 and Atto 655). The obtained "ringlike" structures reflect the optical sectioning capability of confocal imaging. Adapted with permission from *ACS Nano* 2020, 10.1021/acsnano.0c07322. Copyright 2020 American Chemical Society.

reduces permanent photobleaching. We found that an oxygen-depleted environment results in low on-switching rates for Atto 655, probably due to a long-lived nonfluorescent, reduced form.[55] However, using a buffer that only contains thiol (MEA) was sufficient for dSTORM measurements with both fluorophores.

To validate fluorescence-lifetime multiplexing SMLM on biological samples, we performed dSTORM imaging of Alexa 647 labelled β-tubulin and Atto 655 labelled clathrin in COS-7 cells. Thus, two different targets are labelled with two spectroscopically similar dyes with different fluorescence lifetimes. To improve lifetime contrast and brightness of both dyes, all dual-label dSTORM cell images were acquired in D_2O instead of PBS buffer and with the same thiol concentration as for the bead imaging.[149, 150] Additionally, a short PEG-4 linker was inserted between the secondary antibody and Atto 655 to reduce local environment effects that could bias its lifetime value.[151] To classify localisations, pattern matching was applied as an alternative to lifetime fitting. For this, the likelihood that the TCSPC histogram of a single localised molecule originates from the probability distribution of the reference species was calculated and the molecule classified according to the reference that yielded the highest likelihood. The two reference patterns for each sample, shown in figure 3.13a, were obtained by measuring samples containing only one species and normalising the compounded single molecule TCSPC curves. Bayesian pattern matching is, from a statistical point of view, the optimal method for classification and has several advantages: it uses all the detected photons, it does not assume that fluorescence decays are monoexponential, and it is fit-free and therefore fast and stable.[21, 142] From figure 3.13b and figure 3.14b, it can be seen that the lifetime distributions of both species overlap. Nevertheless, it is possible to identify species 1 with less than 5 % false

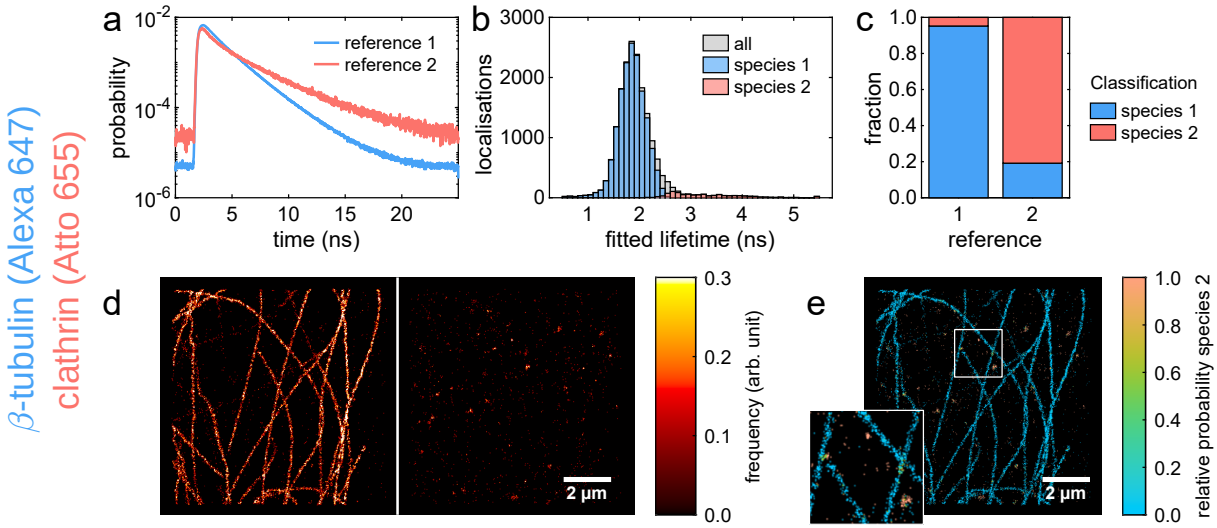

Figure 3.13: Lifetime-based multiplexed dSTORM imaging of Alexa 647 labelled β-tubulin and Atto 655 labelled clathrin in fixed COS-7 cells. All dSTORM images are $10 \times 10\,\mu m$ and reconstructed with a 10 nm Gaussian PSF. (a) Reference TCSPC histograms, measured with samples labelled only with one dye (reference 1, Alexa 647; reference 2, Atto 655). (b) Histogram of the fitted single-molecule lifetimes of all localisations, localisations classified as species 1 (Alexa 647), and localisations classified as species 2 (Atto 655). (c) Calculated cross-talks for the wrong species assignment by classifying the reference samples. Species 1 represents Alexa 647, species 2 represents Atto 655 dye. (d) Super-resolved confocal dSTORM images of localisations classified Alexa 647 β-tubulin (left)/Atto 655 clathrin (right). Both images share the same intensity scale which is proportional to the local number of localisations. (e) Super-resolved probability images obtained by the pattern matching analysis. Species 2 represents Atto 655. The intensity was exponentiated with a γ of 0.7. Adapted with permission from *ACS Nano* 2020, 10.1021/acsnano.0c07322. Copyright 2020 American Chemical Society.

classifications and species 2 with less than 20 %, as shown figure 3.13c, by rejecting classifications that have a relative probability below 99 % (see section 3.2.9). Corresponding dSTORM images for both targets are shown in figure 3.13d. The resulting, super-resolved probability image, based on the pattern matching analysis, is shown in figure 3.13e, where the colour encodes the weighted local average of the relative probabilities for species 2, with weights given by a Gaussian at the position of the localisations.

One of the biggest advantages of confocal scanning SMLM is the possibility to avoid chromatic aberration artifacts in co-localisation measurements. To demonstrate this, we labelled α-tubulin and β-tubulin, which are co-localised in microtubules, with Atto 655 and Alexa 647, respectively. For the probability analysis, corresponding reference TCSPC curves were measured (figure 3.14a) of separate Atto 655 labelled α-tubulin and Alexa 647 labelled β-tubulin samples. To verify correct co-localisation between the two species, we calculated the cross-correlation (shown in figure 3.14c) between corresponding images (figure 3.14d). Its maximum was at a shift of 5 nm, which was smaller than the average localisation precision and indicates that there was a negligible shift between the channels. This can also be seen in the super-resolved probability image presented in figure 3.14e: gaps in Atto 655 labelling appear in blue (0 probability for species 2), whereas a good overlap between both channels appears green (similar probability for both species). No

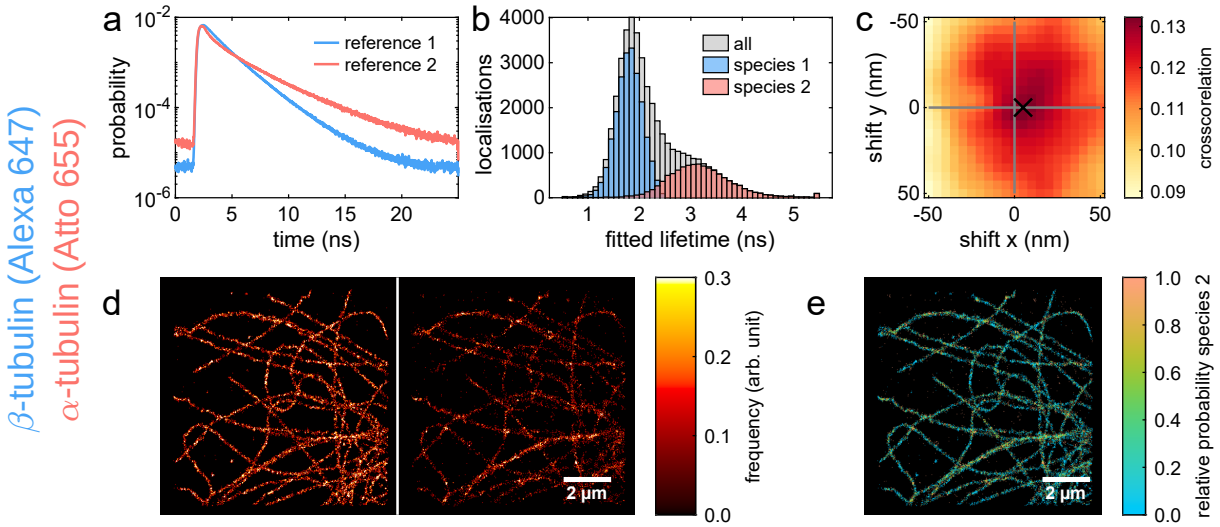

Figure 3.14: Lifetime-based multiplexed dSTORM imaging of fixed COS-7 cells. The panels (a,b,d,e) are equivalent to figure 3.13 but with Alexa 647 labelled β-tubulin and Atto 655 labelled α-tubulin. (a) Reference TCSPC histograms, measured with samples labelled only with one dye (reference 1, Alexa 647; reference 2, Atto 655). (b) Histogram of the fitted single-molecule lifetimes of all localisations, localisations classified as species 1 (Alexa 647), and localisations classified as species 2 (Atto 655). (c) Cross-correlation, calculated between super-resolved images of species 1 and species 2 to estimate a possible shift. The underlying images were reconstructed with 5 nm pixel size and a 5 nm Gaussian PSF. (d) Super-resolved confocal dSTORM images of localisations classified as Alexa 647 β-tubulin (left)/Atto 655 α-tubulin (right). Both images share the same intensity scale which is proportional to the local number of localisations. The less bright appearance of the Atto 655 images reflects the lower number of localisations for this dye. (e) Super-resolved probability images obtained by the pattern matching analysis. Species 2 represents Atto 655. The intensity was exponentiated with a γ of 0.7. Adapted with permission from *ACS Nano* 2020, 10.1021/acsnano.0c07322. Copyright 2020 American Chemical Society.

spatial shift between both channels is expected since our method is conceptually free of chromatic aberrations. The generated image depends solely on the excitation PSF, provided the pinhole is sufficiently large. This holds even true for multicolour detection as exploited in a recent implementation of multicolour MINFLUX.[84]

3.4 CONCLUSION

In summary, we presented confocal laser-scanning FL-SMLM which combines sectioning and lifetime information with super-resolution imaging. The technique is straightforward to implement on a commercial CLSM with TCSPC capability and fast laser scanning. As light exposure is limited only to the scanned area, it is possible to sequentially image different regions of interest without prior photobleaching of other regions. We demonstrated FL-SMLM with both, dSTORM and DNA-PAINT, which are the most commonly used SMLM modalities. The high lifetime resolution enables lifetime-based multiplexing within the same spectral window, distinguishing different fluorescent labels solely by their lifetimes. In combination with the optical sectioning of a CLSM, this allows for chromatic aberration-free super-resolution imaging of mul-

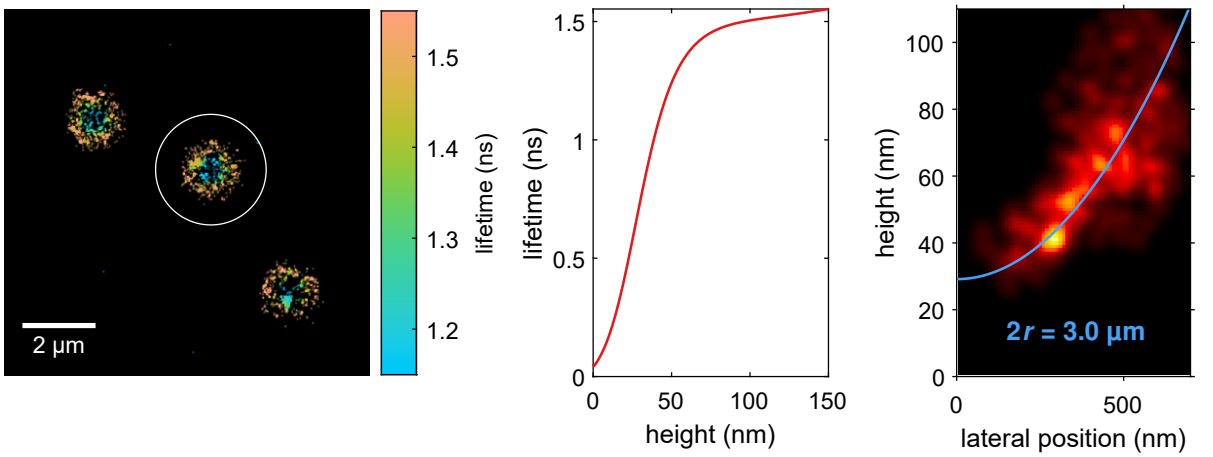

(a) super-resolved FLIM (b) MIET curve (c) azimuthally integrated profile

Figure 3.15: Confocal MIET-STORM of Alexa 647 labelled beads (⌀ 3 µm) above a 5 nm gold layer. The sample was prepared and measured as described in section 3.2. The lifetime of the localisations of the highlighted bead in (a) were converted into heights utilising the MIET curve (b). A sphere with 3 µm diameter was fitted to the 3D localisations. (c) Localisation density of an azimuthal integration and the fitted sphere (blue line). The lateral position is relative to the fitted centre of the sphere.

tiple cellular structures. The additional lifetime information in FL-SMLM also offers the fascinating prospect of lifetime-based super-resolution FRET imaging,[131, 152] thus providing the possibility to disentangle fast dynamics from stationary intermediate states.[119] Another potential application is to use the lifetime information for combining lateral super-resolution of SMLM with the superior axial super-resolution of *metal-induced energy transfer* (MIET) imaging.[110, 113] This could enable 3D super-resolution imaging with exceptionally high isotropic resolution and is briefly demonstrated in the following outlook.

3.5 OUTLOOK – MIET-SMLM

The lifetime-resolved SMLM presented here provides the lifetime for each localisation. When measuring above a gold-coated substrate, quenching by MIET turns the lifetime into a measure of height above the surface. In this case, the lateral localisation from SMLM can be augmented to 3D and, due to the high axial localisation precision of MIET, isotropic 3D localisation becomes feasible.

As first proof-of-concept, surface labelled beads were immobilised on a cover glass coated with a 5 nm gold and 10 nm SiO_2 layer, and a confocal dSTORM measurement was performed, while focussing on the surface. In the super-resolved FLIM reconstruction in figure 3.15(a), it is evident that the lifetime in the centre of the bead is lowest and increases outwards. The lifetimes were converted to axial positions with the MIET curve (figure 3.15(b)) and the 3D localisations were fitted with a sphere. In figure 3.15(c), it is apparent that the fit agrees well with data, which confirms the precision of the 3D localisation. The precision decreased

with increasing height due to the decreasing slope of the MIET curve. The bead seemed to have a minimal distance to the surface of ∼30 nm which was larger than expected. In future, the lifetime fitting might be extended to take the IRF and scattering from the gold into account and hence to avoid systematic bias.

Instead of the CLSM setup employed here, MIET-SMLM may also be implemented with a TCSPC camera. It was demonstrated in section 4.5, that the utilised TCSPC camera is capable of dSTORM. The axial range of MIET-SMLM is limited to the MIET range (∼150 nm). Other methods providing a high resolution and isotropic 3D localisations (*e. g.* iPLAM, MINFLUX) are less restricted in the axial range, but require technically challenging setups. MIET-SMLM by contrast is comparatively simple to implement. It only requires CLSM with TCSPC detection and gold coated cover glasses. The MIET range is ideal to investigate large protein complexes in 3D, making it attractive for structural biology.

4 WIDE-FIELD LIFETIME IMAGING OF SINGLE MOLECULES

Fluorescence lifetime imaging of single molecules is commonly performed with a confocal microscope, similar to the setup presented in chapter 3. In this chapter, an alternative method using a novel single-photon sensitive camera is presented.
This chapter is based on the following publication:
Nazar Oleksiievets,* Jan Christoph Thiele,* André Weber, Ingo Gregor, Oleksii Nevskyi, Sebastian Isbaner, Roman Tsukanov, Jörg Enderlein, 'Wide-Field Fluorescence Lifetime Imaging of Single Molecules', *J. Phys. Chem. A* 2020, 124, 17, pp. 3494–3500. 10.1021/acs.jpca.0c01513

∗ These authors contributed equally to this work.

Contribution In this project, I contributed to the experimental design, developed the data analysis routines, and contributed to the writing of the manuscript.

4.1 INTRODUCTION

Fluorescence microscopy has revolutionised our understanding of biological processes. One of its variants is *fluorescence-lifetime imaging microscopy* (FLIM) which has become a valuable microscopy technique in medicine and biology.[38, 153, 154] The most important applications of FLIM are local environment sensing (*e. g.* pH, oxygen, polarity, viscosity),[120] distinguishing between different fluorophores with similar emission spectra based on their fluorescence lifetime (thus allowing multiplexing),[145] and Förster resonance energy transfer (FRET) imaging by measuring the lifetime of the donor.[155, 156]

One of the big technical challenges of FLIM is to achieve high image acquisition speed without compromising sensitivity. There are two fundamentally different technical approaches to FLIM. The first approach is based on *confocal laser-scanning microscopy* (CLSM), where one scans a field of view point by point and usually measures the fluorescence lifetime (and intensity) by *time-correlated single-photon counting* (TCSPC) at each scan position.[157] This approach assures highest sensitivity, but comes with the trade-off of reduced image acquisition speed. The second approach uses camera-based phase-fluorometry,[158, 159] which allows fast image acquisition at the cost of tremendously reduced sensitivity. Wide-field phase-fluorometry is, for example, much too insensitive for being capable of single-molecule imaging. Only recently, new single-photon counting wide-field detectors were developed but they are still in their infancy and not widely available.[160, 161] Other, more particular FLIM techniques, are based on gated optical image intensifiers,[162] electro-optical modulators,[132] electron multiplying

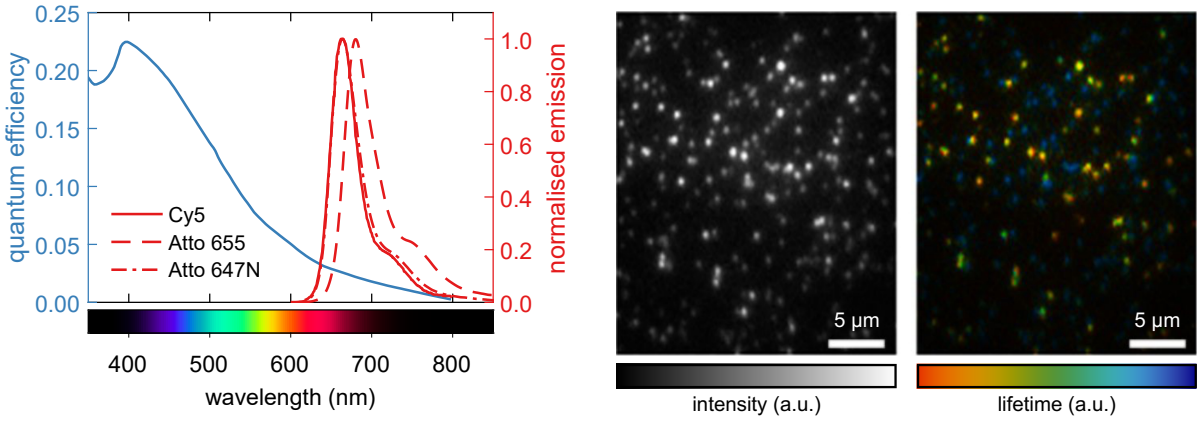

(a) quantum efficiency and fluorophore spectra (b) intensity image (left) and lifetime image (right)

Figure 4.2: (a) Typical quantum efficiency of the TCSPC camera LINCam and emission spectra of the used flurophores.[167–170] (b) Illustration of intensity and lifetime images of single molecules with different lifetimes as generated by the Photonscore preview software. Adapted with permission from *J. Phys. Chem. A* 2020, 124, 17, 3494–3500. Copyright 2020 American Chemical Society.

Figure 4.1: The TCSPC camera LINCam25. Adapted with permission from J. Phys. Chem. A *2020, 124, 17, 3494–3500. Copyright 2020 American Chemical Society.*

micro-channel plates (MCP),[163, 164] or wide-field time-gated SPAD arrays.[165] However, all these approaches are currently too insensitive for genuine single-molecule applications.

Here, we investigate the applicability of a novel, commercially available wide-field single-photon counting camera (figure 4.1, LINCam, Photonscore GmbH, a spin-off from Leibniz Institute for Neurobiology, Magdeburg) for FLIM with single-molecule sensitivity. The TCSPC-based lifetime camera is designed for photon detection from the UV to the visible spectrum. It employs a Micro-Channel-Plate Photo-Multiplier Tube and uses a capacity-coupled imaging technique (charge image), combined with a charge division anode for positional readout. The position of an incident photon is reconstructed by means of an artificial neural network computation model as precise as 20 µm over the active detection area of ⌀ 25 mm.[164] Therefore, the resulting image is comparable to that of a conventional megapixel charge-coupled device (CCD) camera and allows for TCSPC-FLIM with a regular fluorescence wide-field microscope.[166] The detector is equipped with a multi-alkali photo-cathode, optimised for UV light. However, its quantum efficiency of detection drops significantly towards the red spectral region: from ∼20 % quantum efficiency for blue light to below 5 % for red light (figure 4.2(a)). Nonetheless, due its nearly absent noise and dark counts, it is possible to achieve single-molecule sensitivity, even in the red spectrum. To demonstrate the single-molecule sensitivity, we perform wide-field FLIM of three widely used fluorophores, Cy5, Atto 655, and Atto 647N, which have similar emission spectra (figure 4.2(a)) but differ in their lifetimes, see figure 4.2(b).

We determine fluorescence lifetimes of individual molecules by fitting the recorded TCSPC data on a molecule-by-molecule basis. Based on these fitted lifetime values, we successfully distinguish between dif-

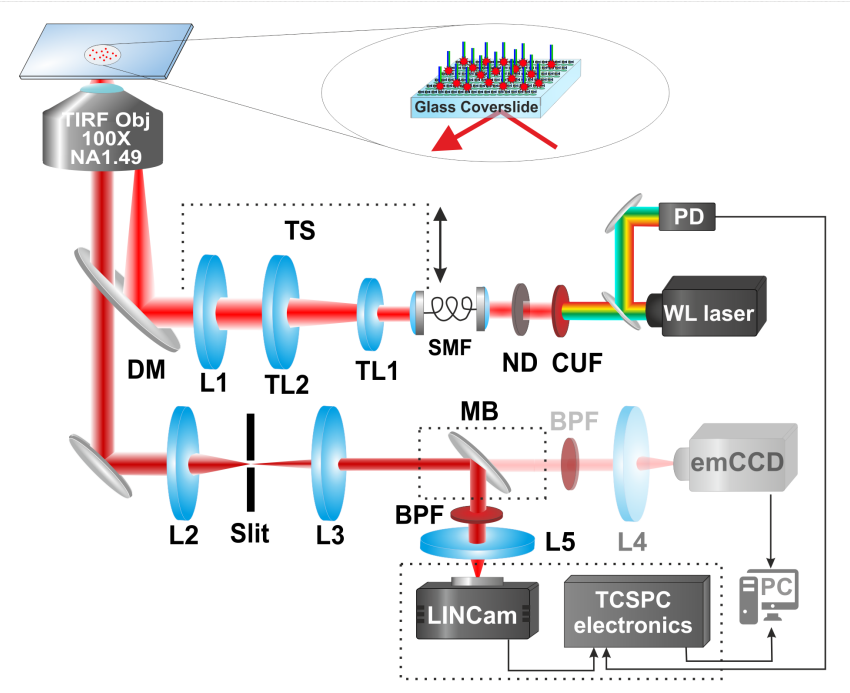

Figure 4.3: Detailed schematic of the custom-built optical setup used for wide-field lifetime imaging with the TCSPC camera LINCam. The elements are described in text below. Adapted with permission from *J. Phys. Chem. A* 2020, 124, 17, 3494–3500. Copyright 2020 American Chemical Society.

ferent molecular species in a mixed sample of all three fluorophores. Finally, we perform wide-field FLIM in combination with *metal-induced energy transfer* (MIET),[110] which allows us to determine the axial position of individual molecules above a surface.[107, 112–114, 171–173]

4.2 METHODS

4.2.1 *Experimental setup*

Measurements were performed using a custom-built setup (figure 4.3). A pulsed super-continuum white-light laser (Fianium WhiteLase SC450, NKT Photonics) with a repetition rate of 20 MHz was used for excitation. A custom photodiode (PD) optically triggered the TCSPC camera (LINCam25 with S20BB photocathode, Photonscore). A narrow excitation spectrum was selected with a clean-up filter (CUF) (ZET 640/10, Chroma). The laser excitation power was adjusted by neutral density filters (NE10A-A, NE20A-A, Thorlabs) and a variable neutral density filter (ND) (NDC-50C-4-A, Thorlabs). The laser beam was coupled into a single-mode optical fiber (SMF) (P1-460B-FC-2, Thorlabs) with a typical coupling efficiency of 40 – 50 %. After the fiber, the beam was expanded by a factor of 3.6 with two telescopic lenses (TL1 and TL2). The collimated laser beam was focused into the back focal plane of the

objective (UAPON 100× oil, 1.49 NA, Olympus) using lens L1 (AC508-180-AB, Thorlabs). In order to switch between different illumination schemes (Epi-, HILO-, or TIR), the beam was mechanically shifted perpendicular to the optical axis with a translation stage TS (LNR50M, Thorlabs). A high-performance two-axis linear stage (M-406, Newport) was used for smooth lateral sample positioning. For focusing, the objective was moved along the optical axis with an independent translation stage (LNR25/M, Thorlabs), equipped with a differential micrometer screw (DRV3, Thorlabs). Collected fluorescence was spectrally separated from the excitation path with a multi-band dichroic mirror (DM) (Di03 R405/488/532/635, Semrock), which transmitted the fluorescence light towards the tube lens L2 (AC254-200-A-ML, Thorlabs). The region of interest within the field of view was selected with an adjustable slit aperture (SP60, OWIS) which was positioned in the image plane. Lenses L3 (AC254-100-A, Thorlabs) and L4 (AC508-150-A-ML, Thorlabs) re-imaged the fluorescence light from the slit onto an emCCD camera (iXon Ultra 897, Andor). Alternatively, lens L5 (AC508-250-A-MC, Thorlabs) re-imaged the light onto the TCSPC camera. For the switching between the two cameras, a dielectric mirror (BB1-E02, Thorlabs) was positioned on a magnetic base plate MB (KB50/M, Thorlabs) with removable top. Scattered excitation light was removed with a band-pass filter BP (BrightLine HC 692/40, Semrock). The magnification with the emCCD was 166.6×, resulting in an effective pixel size of 103.5 nm in sample space. Magnification for imaging with LINCam was 222×, so that for a partitioning of the sensor into 1024 × 1024 pixels, the effective pixel size in the sample space was 96 nm.

4.2.2 *Buffer solutions*

The following buffer solutions were used: DNA annealing buffer included 10 mM Tris, pH 8.0, 1 mM EDTA and 100 mM NaCl. Buffer A (used for surface immobilisation) included 10 mM Tris, pH 8.0, 50 mM NaCl. DNA storage buffer included 10 mM Tris, pH 8.0, 1 mM EDTA. As imaging buffer solutions, we used either DNA storage buffer with 500 mM NaCl, or alternatively GLOX buffer (enzymatic oxygen scavenging system) consisting of 0.5 mg/mL glucose oxidase, 40 mg/mL catalase, and 10 %w/v glucose in PBS at pH 7.4. The GLOX buffer was crucial for enhancing photostability and to increase the number of emitted photons, especially for Cy5.

4.2.3 *Sample preparation*

Cover glasses were sonicated in 1 M KOH for 15 min, rinsed with deionised water and dried using air flow. Four-well silicone inserts (Ibidi 80469, Germany) were attached to the cover glass to form four measurement chambers. BSA-biotin (A8549, Sigma-Aldrich) was diluted in buffer A to a concentration of 0.5 mg/mL and incubated in the chambers overnight at 4 °C. The next day, the chambers were washed at least

3 times the volume of a chamber with buffer A. Neutravidin (31000, Thermo Fisher Scientific) was diluted in buffer A to a concentration of 0.5 mg/mL and then added to one chamber for 5 min. Next, the chamber was rinsed at least 3 times. DNA-fluorophore constructs were immobilised to the surface using biotin-avidin chemistry.

We designed the double-stranded DNA-construct as follows: Primary single-stranded DNA (strand 1) was biotinylated at its 5′ end, while the complementary DNA (strand 2) was labelled at its 3′ end with a single fluorophore (either Cy5, Atto 655, or Atto 647N), see table 4.1 for the DNA sequences. The binding of the fluorophores to DNA increased their photostability and decreased blinking. The fluorophore was attached close to the surface anchor of the DNA. This design is similar to the one used in DNA-PAINT.[65] The two DNA strands were hybridised at high concentration (200 nM) using the following protocol: The mixture of the two DNA strands was heated to 94 °C in annealing buffer for 5 min and then gradually cooled to room temperature over the course of 30 min. The resulting dsDNA solution was diluted by a factor of $\sim 10\,000\times$ to reach single-molecule concentration, before addition to the sample chamber. After 5 – 10 min incubation time, the chamber was rinsed with imaging buffer by exchanging the liquid in the chamber (80 µL) at least 3 times. For the mixed fluorophores sample, we mixed the diluted stock solution with a stoichiometry of Atto 647N:Atto 655:Cy5 = 1:3:10. The much higher Cy5 concentration was necessary to compensate photobleaching before the start of the acquisition (*e. g.* during focusing).

Table 4.1: DNA sequences and their modifications

name	sequence 5′ → 3′	5′ modification	3′ modification
strand 1	GCAGCCACAACGTCTATCATCGATT	–	fluorophore
strand 2	AATCGATGATAGACGTTGTGGCTGC	biotin	–

4.2.4 *Data acquisition*

Experiments were performed with the custom-built wide-field microscope described in section 4.2.1. The excitation was adjusted to TIR illumination with an average laser power of 10 – 20 W/cm^2 and neutral density filters were employed for fine adjustment of the laser power. A supplemental emCCD camera with a much higher detection quantum efficiency than the TCSPC camera was used for focusing. Typical acquisition times per image were 3 – 5 min. Images of several regions of interest (3 – 6) of each sample were acquired. The image acquisition software was provided by Photonscore. All experiments were carried out at a constant temperature of (22 ± 1) °C, which was crucial for the mechanical stability of the optical setup.

For solution measurements, a drop of diluted stock solution was placed on a cover glass. The illumination was adjusted to epi-illumitation and the focus was set several micrometres above the cover glass surface.

Confocal measurements

Confocal measurements were performed on the TCSPC-CLSM setup described in section 3.2.1. Instead of the dichroic beamsplitter, a non-polarising 90:10 beamsplitter (90 % of the emission transmitted) was placed. In the emission path, a long pass filter (647 LP Edge Basic, Semrock) and a band-pass filter BP (BrightLine HC 692/40, Semrock) were used.

The imaging parameters for the TCSPC-CLSM area measurement were as following: virtual pixel size 100 nm, area of interest 40×40 µm, dwell time 100 µs. We used bidirectional scanning with the shift correction explained in section 5.2.1 to increase the measurement speed and photon efficiency, as compared to a monodirectional scan.

4.2.5 *Data analysis*

The data analysis was performed using custom-written MATLAB routines which relied on the Photonscore Software Kit to read photon arrival times and positions from the raw data files. The details for the lifetime fitting of the TCSPC histograms, single molecule detection, and on-/off-state detection are described in the following.

Lifetime fitting

To determine the fluorescence lifetime, the TCSPC histogram was constructed either from all photons (solution/surface measurements) or from photons detected at a molecule position (single molecule lifetime). The tail, starting 0.2 ns after the maximum, of the TCSPC curves was fitted with a monoexponential decay by minimising the negative log-likelihood function with a Nelder–Mead simplex algorithm.[113, 174] For some solution measurements, the TCSPC curve exhibited a biexponential decay and was therefore fitted with the sum of two exponential decays.

Single molecule detection & lifetime determination

First, an intensity image was generated from the raw photon data, rejecting photons arriving outside a 10 ns time gate, starting 0.25 ns after the maximum intensity. For this, the detector was usually divided into 1024×1024 pixels of 96 nm size. Based on the resulting image, single molecules were detected utilising a wavelet algorithm as implemented for the initial version of TrackNTrace.[141] The intensity time traces and TCSPC curves of each identified molecule were extracted from the raw data using a time binning of 1 s. For this, all photons within a 3×3 pixel region around the centre position of each molecule ($\sim 1.4\sigma_{\mathrm{PSF}}$) were collected. Based on the intensity time traces, an on-/off-state detection was applied (see description on the following page) and a TCSPC curve was accumulated, including only time points where the molecule was in its fluorescent on-state. The TCSPC curves were fitted to obtain a lifetime

as described above. TCSPC curves with less than 100 photons in the tail or with a χ^2 of the fit below 0.9 or above 1.1 were rejected.

FLIM images were generated by colour-coding each identified molecule according to its fitted lifetime, while the pixel brightness reflected the true pixel intensity. The lifetime histograms were fitted with a single Gaussian distribution or, for the mixed sample, a sum of three Gaussians, using a Nelder–Mead simplex algorithm.

On-/off-state detection

We used an on-/off-state detection algorithm to identify on-states in intensity time traces of individual molecules. The algorithm is very similar to the burst-detection by Enderlein et al.[175] First, the intensity time trace recorded from one molecule was smoothed by applying a moving Lee-filter, and a step (switching from off- to on-state or *vice versa*) was identified if the smoothed signal exceeded a pre-set threshold. This threshold was defined as twice the background level, and it was scaled for each molecule to the maximum intensity in its time trace divided by the average of the maximum intensities of all molecules. The scaling of the threshold was required to compensate for inhomogeneous illumination. The background level was estimated as the median of all intensities in all time traces below the average intensity level.

MIET

For MIET experiments, samples were prepared on cover glasses coated with (from bottom to top) 2 nm titanium, 10 nm gold, 1 nm titanium and a silicon dioxide spacer of 30, 50 or 70 nm.

The lifetime height dependency (MIET curve, see figure 4.16) was calculated for the given layers using MIET theory.[173] The spacer was omitted to avoid the discontinuity of the lifetime at the spacer surface close to the expected height of the fluorophore and to simplify the calculation by using the same MIET curve for all samples. The single molecule lifetimes were determined as described on the previous page and converted to heights above the metal layer using the MIET curve.

4.3 RESULTS

First, the results validating the accuracy of lifetime determination and single-molecule sensitivity of the wide-field FLIM system are presented. This is followed by the demonstration of two potential applications, lifetime based multiplexing and 3D localisation using MIET.

4.3.1 *Ensemble lifetime measurements*

Fluorescence lifetimes of freely diffusing fluorophores

To evaluate the TCSPC capabilities of the LINCam, we investigated the lifetimes of freely diffusing DNA-fluorophore constructs at high con-

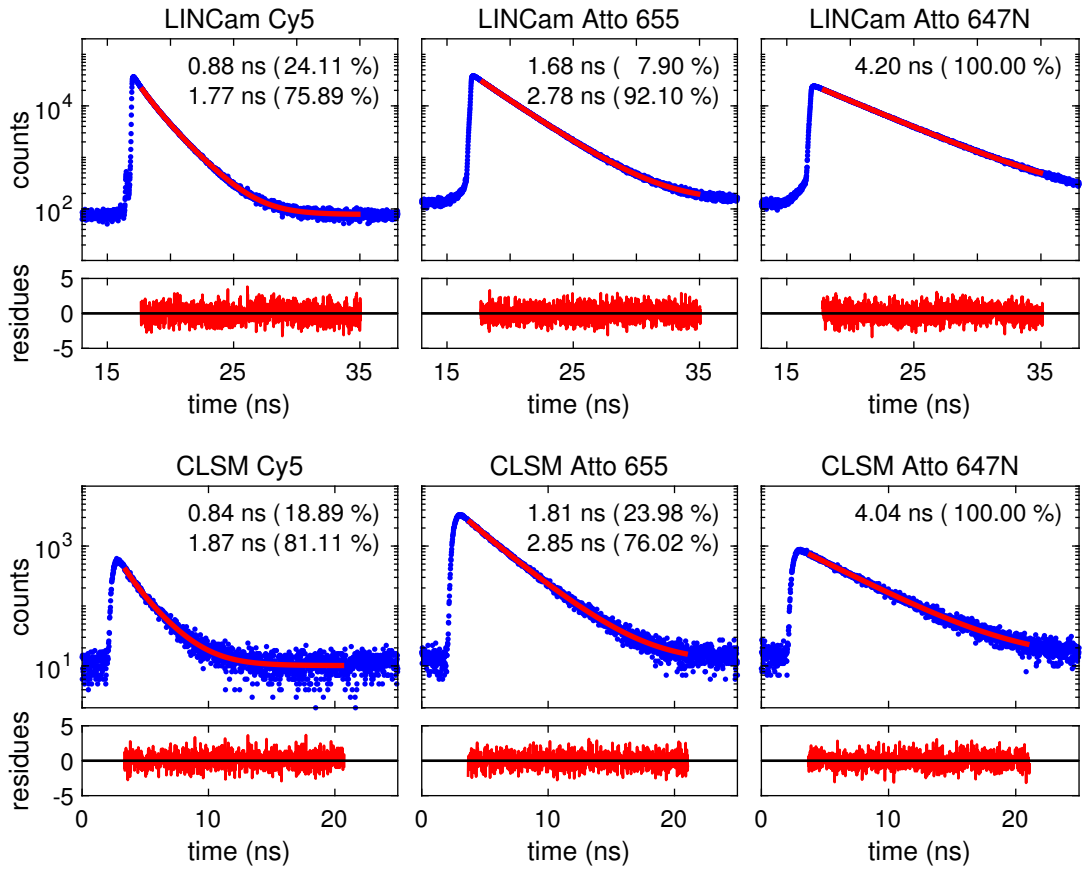

Figure 4.4: Lifetime measurements of freely diffusing fluorophores using either the TCSPC camera LINCam (top row) or TCSPC-CLSM (bottom row). The TCSPC curves and the corresponding single- or double-exponential fits are shown for: Cy5 (left), Atto 655 (middle), Atto 647N (right). For convenience, all lifetime values are summarised in table 4.2

centration (10 nM) and compared the results to lifetimes measured on a TCSPC-CLSM setup. To minimise the influence of different IRFs of both setups (mainly caused by the different excitation lasers) we used a long cutoff of 0.6 ns after the maximum when fitting the TCSPC curves. As shown in figure 4.4, the lifetimes for both setups were in good agreement. We found that for Cy5 and Atto 655, the single exponential function does not describe the experimental TCSPC curves well. Therefore, these curves were fitted with a biexponential decay function. In both cases, an additional faster lifetime component ($\tau_{\text{free-dye}}$) is explained by the presence of fluorophores that were not bound to DNA. The faster lifetime values agree well with the lifetimes of the non-conjugated Cy5 and Atto 655 (data not shown).[168, 169] We attribute the longer lifetime component to the DNA-dye constructs. The fit results are summarised in table 4.2, where the errors denote the standard deviation of three consecutive measurements for each case.

While immobilising the DNA-dye construct on the surface, free dye is washed from the sample and therefore does not affect the measurements of surface-immobilised molecules. As expected, we find that

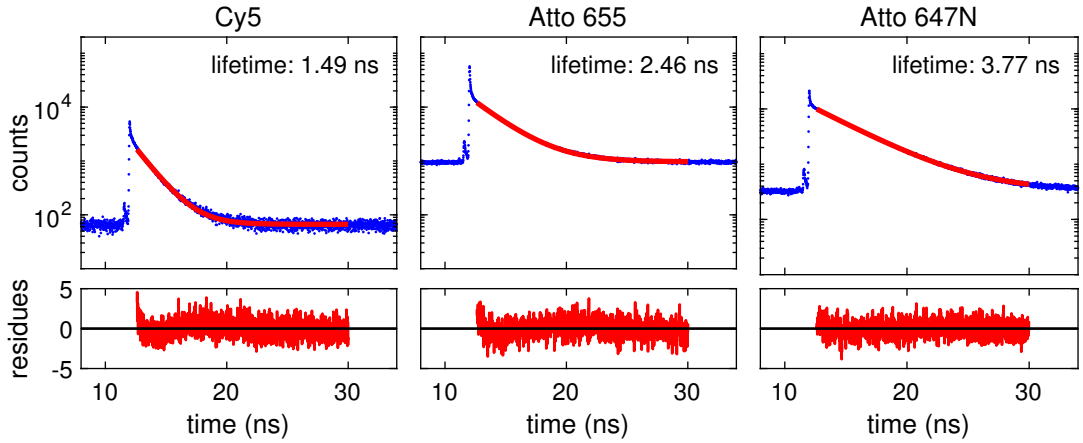

Figure 4.5: Cumulative TCSPC curves measured with the TCSPC camera for the three types of the fluorophores immobilised on a surface, together with the corresponding single-exponential fits: Cy5 (left), Atto 655 (middle), Atto 647N (right).

Table 4.2: Lifetime values of freely diffusing molecules ($\tau_{\text{free-dye}}$ and $\tau_{\text{DNA-dye}}$) and immobilised DNA-constructs (τ_{surface}) measured with the LINCam and with the TCSPC-CLSM setup. The errors are the standard deviation of three consecutive measurements.

Fluorophore	Setup	$\tau_{\text{free-dye}}$ (ns)	$\tau_{\text{DNA-dye}}$ (ns)	τ_{surface} (ns)
Cy5	LINCam	0.88 ± 0.01	1.77 ± 0.01	1.49 ± 0.01
	confocal	0.84 ± 0.04	1.87 ± 0.02	1.94 ± 0.03
Atto 655	LINCam	1.68 ± 0.09	2.78 ± 0.02	2.46 ± 0.01
	confocal	1.81 ± 0.10	2.85 ± 0.09	2.55 ± 0.03
Atto 647N	LINCam	–	4.20 ± 0.01	3.77 ± 0.01
	confocal	–	4.04 ± 0.01	3.92 ± 0.08

the lifetimes of freely diffusing fluorophores are 5 – 10 % longer than the values of the same molecules immobilised on cover glasses (figure 4.5 and table 4.2). This can be explained by surface-fluorophore interactions.[113]

4.3.2 *Single-molecule FLIM*

Three separate samples of surface-immobilised fluorophores, one Cy5, one Atto 655, and one Atto 647N sample, were prepared, utilising a DNA-assisted strategy for immobilisation. The binding to the DNA provided a homogenous environment and increased the photostability of the fluorophores. A precise control of the coverage density was achieved by diluting the stock solutions to concentrations of 100 – 500 pM and varying the incubation time. Exemplary lifetime images are shown in figure 4.6 A1, B1, and C1. To enhance brightness and photostability of the fluorophores, oxygen-scavengers (GLOX) were added to the imaging buffer. Representative intensity time traces of single molecules are shown in figure 4.6 A2, B2, and C2. On average, 196 photons were de-

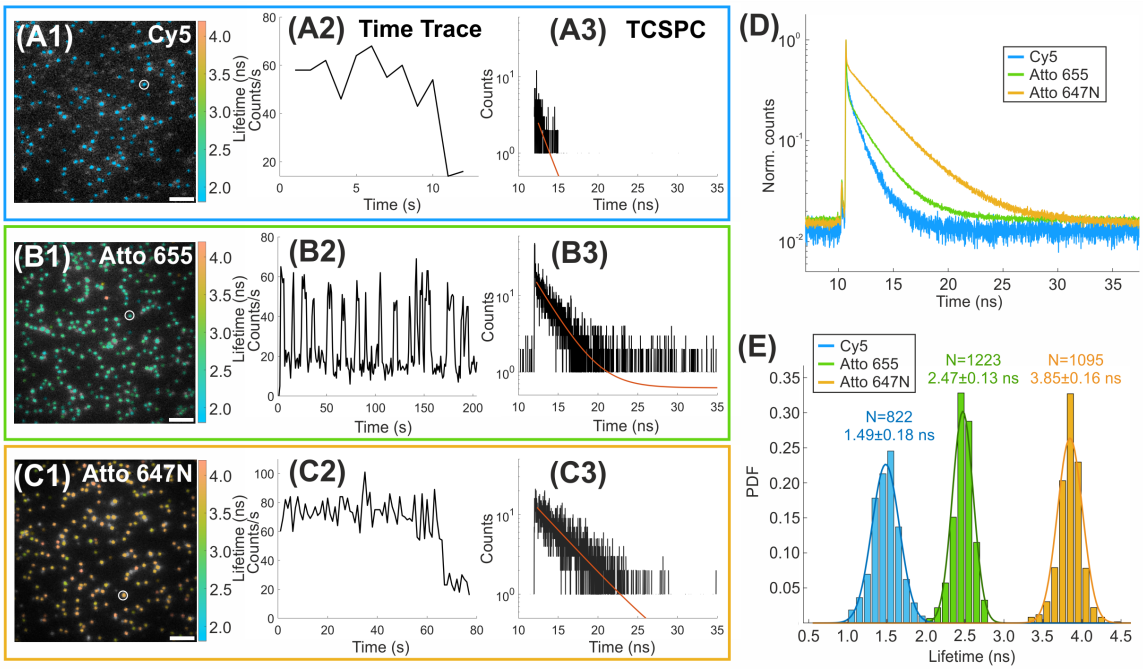

Figure 4.6: Lifetime imaging of surface-immobilised single molecules. Different types of fluorophores were imaged separately. The scale bars are 5 µm. Images of the following fluorophores are shown: (A1) Cy5, (B1) Atto 655, and (C1) Atto 647N. Colours represent lifetime values. White circles indicate molecules that were chosen for the exemplary intensity time traces (A2,B2,C2) and corresponding TCSPC curves (A3,B3,C3). (D) TCSPC curves obtained by adding all single-molecule data of the same type. (E) Probability density function (PDF) of lifetime values of each fluorophore type with the corresponding single-Gaussian fit. The average lifetime and standard deviation of the fit appear next to each peak, as well as the number of molecules used in each lifetime histogram. Adapted with permission from *J. Phys. Chem. A* 2020, 124, 17, 3494–3500. Copyright 2020 American Chemical Society.

tected from Cy5 molecules, 1759 photons from Atto 655 molecules, and 3242 photons from Atto 647N molecules before photobleaching. In our experimental conditions, photobleaching of Cy5 occurred within a few seconds, while the emission showed no blinking before bleaching. Atto 655 kept on emitting for hundreds of seconds before photobleaching, while exhibiting blinking as explained on the following page. Atto 647N showed the highest emission intensity and was, without any discernible blinking, stable for hundreds of seconds before photobleaching. The lifetime values of each detected single molecule were determined by fitting the corresponding TCSPC curve with an exponential function (figure 4.6 A3, B3, and C3). A cumulative TCSPC curve of all detected single molecules from each species is shown in figure 4.6 D. To reduce the statistical uncertainty, several (3-5) regions of interest were combined. The single-molecule lifetime histograms (figure 4.6 E) were fitted with a single Gaussian function, resulting in the following average lifetimes and standard deviations: Cy5 (1.49 ± 0.18) ns, Atto 655 (2.47 ± 0.13) ns, and Atto 647N (3.85 ± 0.16) ns. The lifetime values of DNA-bound fluorophores were higher than those of free fluorophores, due to the interaction between the fluorophores and the DNA.[148] The average lifetimes are similar (within half a standard deviation) to the ensemble surface measurements given in table 4.2.

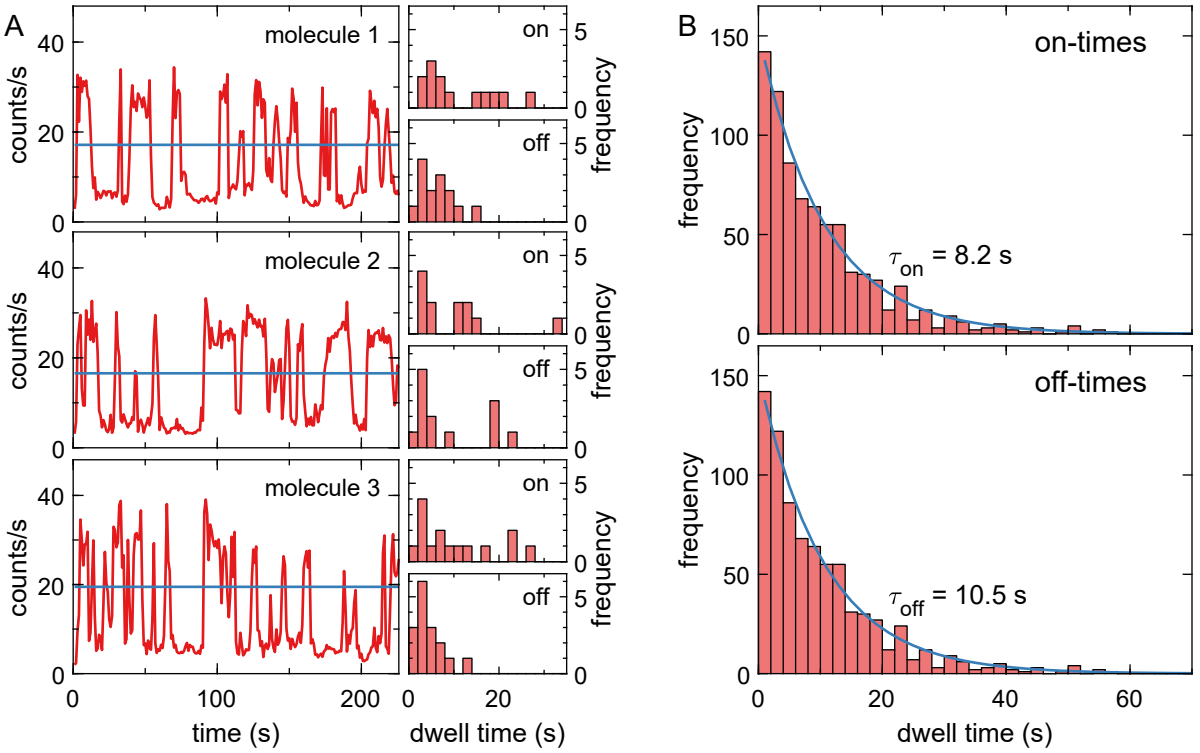

Figure 4.8: Analysis of the blinking behaviour of Atto 655 in oxygen depleted conditions (GLOX). (A) Exemplary intensity time traces of single molecules and corresponding dwell time histograms. Solid blue lines represent the threshold applied to the time traces. (B) Cumulative on- and off-dwell time histograms for 65 time traces with the corresponding single exponential fits (solid blue line). The values of the average on- and off-times from the fit are given in the plot.

Theoretical estimate of the width of the lifetime distribution

To judge how close the experimentally observed width of the lifetime histograms was to the theoretical shot-noise limit, we calculated a theoretical shot-noise limited distribution in the following way: For each molecule, we generated a Gaussian distribution of unit area, centred at the overall mean lifetime $\langle\tau\rangle$ and of a variance equal to $\langle\tau\rangle^2/N$, with N as the number of detected photons from the considered molecule. Subsequently, we added all of these Gaussians into one final theoretical lifetime distribution. The experimental and calculated distributions for the Atto 655 sample are shown in figure 4.7. The standard deviations of a Gaussian fit to each distribution yielded 0.06 ns for the shot noise limited distribution and 0.13 ns for the experimental distribution. The broadening of the experimental histogram is partially caused by uncorrelated background. Local molecule-environment interactions, affecting the lifetime, may be another contribution.

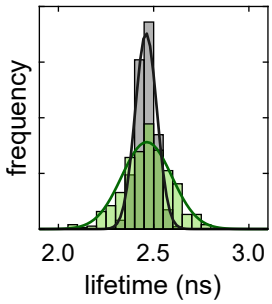

Figure 4.7: Contribution of shot noise to experimental lifetime distribution of Atto 655. Shot-noise limited (grey) and experimental (green) distribution.

Characterisation of Atto 655 blinking behaviour

Although the detection efficiency of the TCSPC camera is relatively low, we were able to capture blinking events of single Atto 655 fluorophores. The blinking behaviour was analysed with an on-/off-state detection algorithm, as shown in the exemplary time traces in figure 4.8 A. A mono-

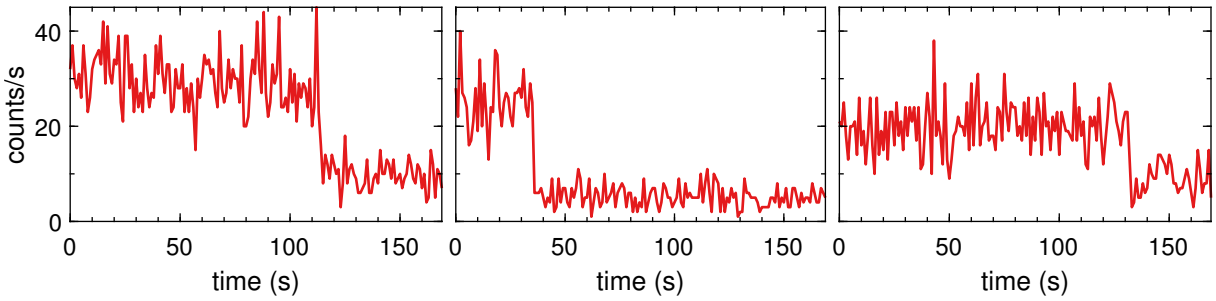

Figure 4.9: Exemplary intensity time traces for Atto 655 single molecules, in absence of GLOX in the buffer solution.

exponential fit of the combined histograms of 65 traces (figure 4.8 B) resulted in a characteristic on-time of 8.2 s and off-time of 10.5 s. Compared to literature values,[148] these are quite long on- and off-times for Atto 655, which may be explained by the oxygen-depleted environment in the imaging buffer containing GLOX and the low laser power used in our experiment. Atto 655 exhibits triplet states which are known to be quenched by oxygen in solution.[55] In a oxygen containing environment (without GLOX), Atto 655 exhibited fast blinking on the microseconds timescale, which is not detectable in the time traces (figure 4.9).[176]

4.3.3 *FLIM of single molecules in a mixed sample*

The distinct fluorescence lifetimes of our three fluorophores can be used to identify them in mixed samples. We demonstrate this by performing

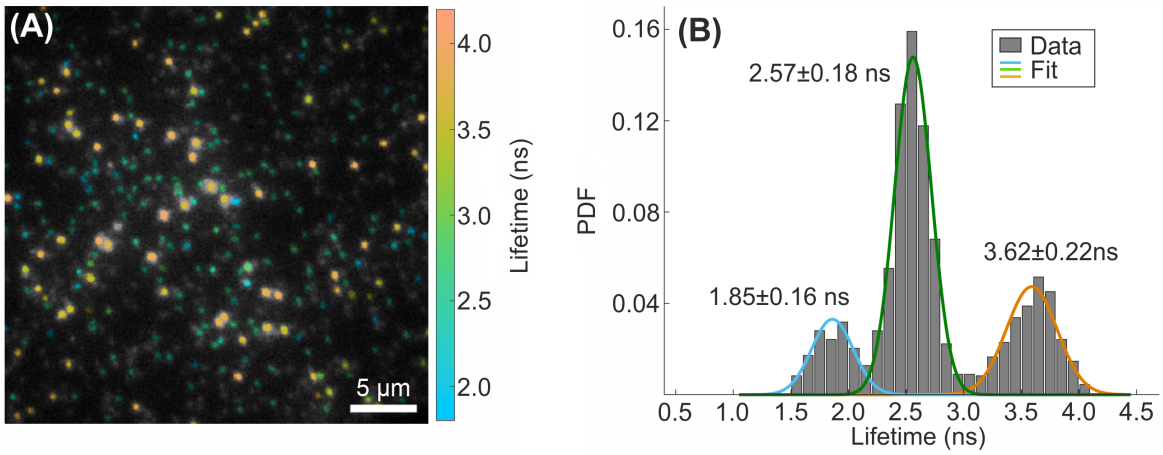

Figure 4.10: FLIM image of a mixture of Cy5, Atto 655, and Atto 647N fluorophores immobilised to the surface. (A) Exemplary lifetime image. (B) Lifetime histogram of the mixed sample and the corresponding three peak Gaussian fit. The different components of the Gaussian fit are shown in different colours. The lifetime histogram includes data from four images, in total 1573 molecules. The average lifetime values and the standard deviations of the fit are given next to each peak. Adapted with permission from *J. Phys. Chem. A* 2020, 124, 17, 3494–3500. Copyright 2020 American Chemical Society.

FLIM measurements on a sample containing all three fluorophores. To mimic a common bio-imaging situation with high labelling density, we prepared a sample with high surface coverage as shown in figure 4.10 A. For the samples with only one type fluorophores, the lifetime distributions for the three fluorophores (figure 4.6 E) were separated, which facilitates the identification of each molecule. In the mixed sample, however, the determination of exact lifetime values for each molecule was not trivial due to the frequently occurring partial overlap of neighbouring molecules. To minimise background and cross-talk between neighbouring molecules, we employed an on-/off-state detection algorithm and chose sufficiently small virtual pixels. The influence of the on-/off-state detection and pixel size are explained in detail on the next page. With these optimisations, we obtained a lifetime distribution as shown in figure 4.10 B. The peaks are well separated, making classification straightforward, however, compared to the pure samples, we find that the single-molecule lifetimes move closer to the overall average (figure 4.11 A). This is probably caused by remaining cross-talk between neighbouring molecules due to the relatively high density of fluorophores.

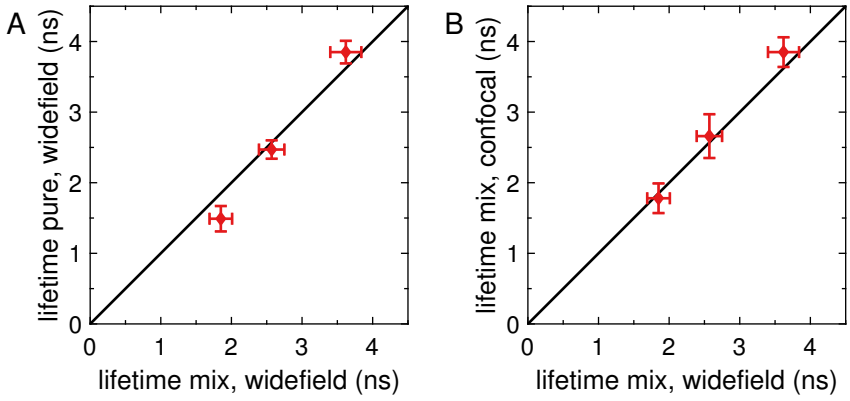

Figure 4.11: Comparison of the average lifetimes obtained with the TCSPC camera from the mixed fluorophores sample and (A) the pure samples or (B) the mixed sample measured with the TCSPC-CLSM. The error bars give the standard deviation of the distributions and the diagonal lines indicate equal lifetimes.

Comparison with TCSPC-CLSM

Due to less background and a smaller PSF, distinguishing the three fluorophores using a confocal microscope is less challenging and does not require an on-/off-state detection, as illustrated in the TCSPC-CLSM scan of surface-immobilised mixed fluorophores (figure 4.12).

As for the pure samples, we found an excellent agreement between the lifetime values obtained by both experimental approaches for the measurement of mixed sample (figure 4.11 B). However, it is evident that the width of the peaks from the TCSPC-CLSM measurements are broader than for the TCSPC camera. When we compared the number of photons acquired during the same time interval for both techniques, we

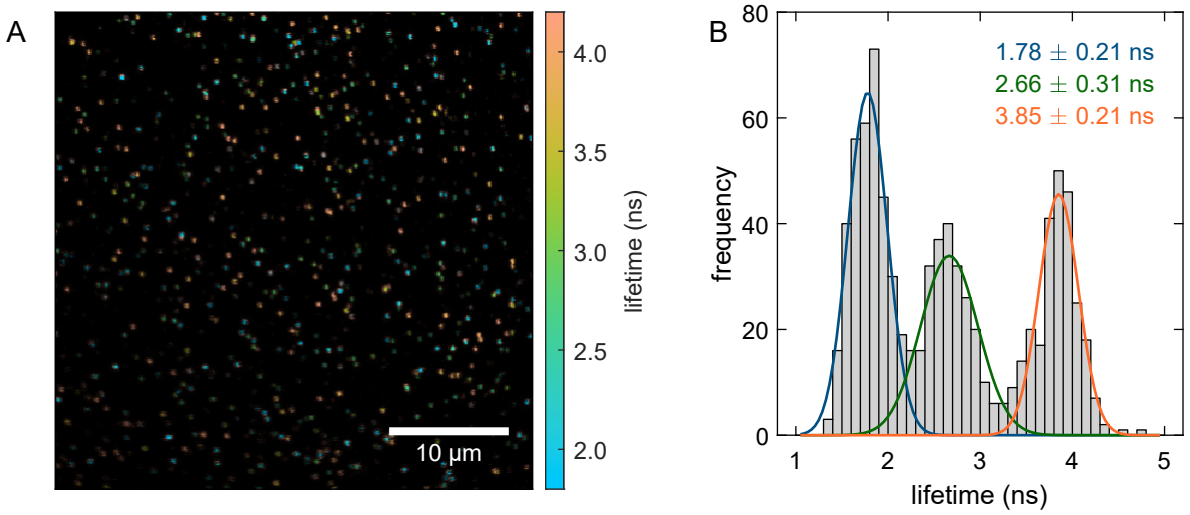

Figure 4.12: FLIM image, recorded with the TCSPC-CLSM setup, of a mixture of Cy5, Atto 655 and Atto 647N fluorophores immobilised to the surface. (A) Exemplary lifetime image. (B) Lifetime histogram combined from two areas. The solid lines indicate the components of a fit with the sum of three Gaussian distributions. Peak centres and standard deviations are given in the plot.

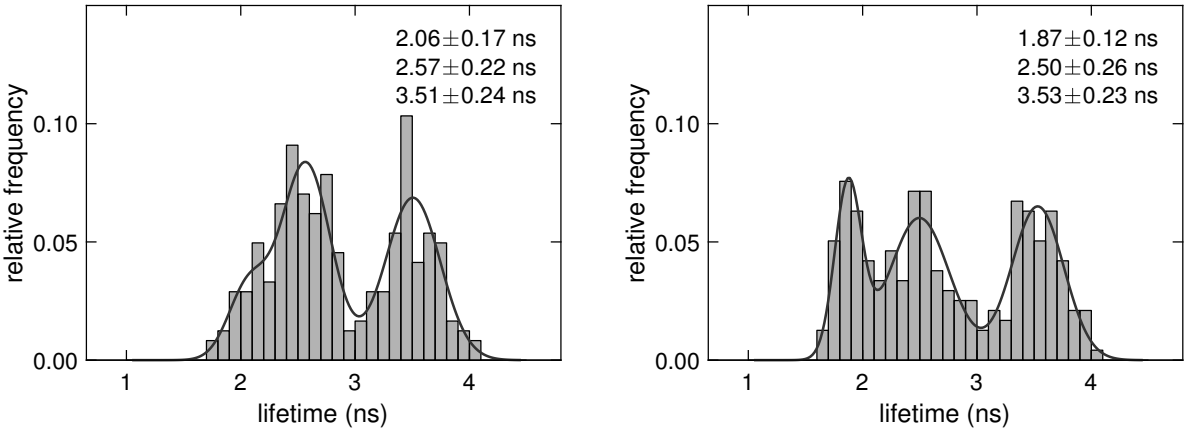

(a) without on-/off-state detection

(b) with on-/off-state detection

Figure 4.13: Improved peak separation in lifetime histograms by applying an on-/off-state detection algorithm. Lifetime histogram obtained from a single measurement of a mixed fluorophore sample without (a) and with (b) on-/off-state detection. The solid line represents a fit with the sum of three Gaussians. Centre and standard deviation of the Gaussians are given in the plot.

found that the TCSPC-CLSM setup registered five-fold less photons than the TCSPC camera, despite its low quantum efficiency. This might be an effect of the scanned acquisition in TCSPC-CLSM. The higher power density during the short time that the molecule is actually in the focus, might also increase the switching to dark triplet states.

Influence of the on-/off-state detection on the lifetime histograms

In order to verify the efficiency of the on-/off-state detection, we compared the lifetime histograms obtained with and without applying the

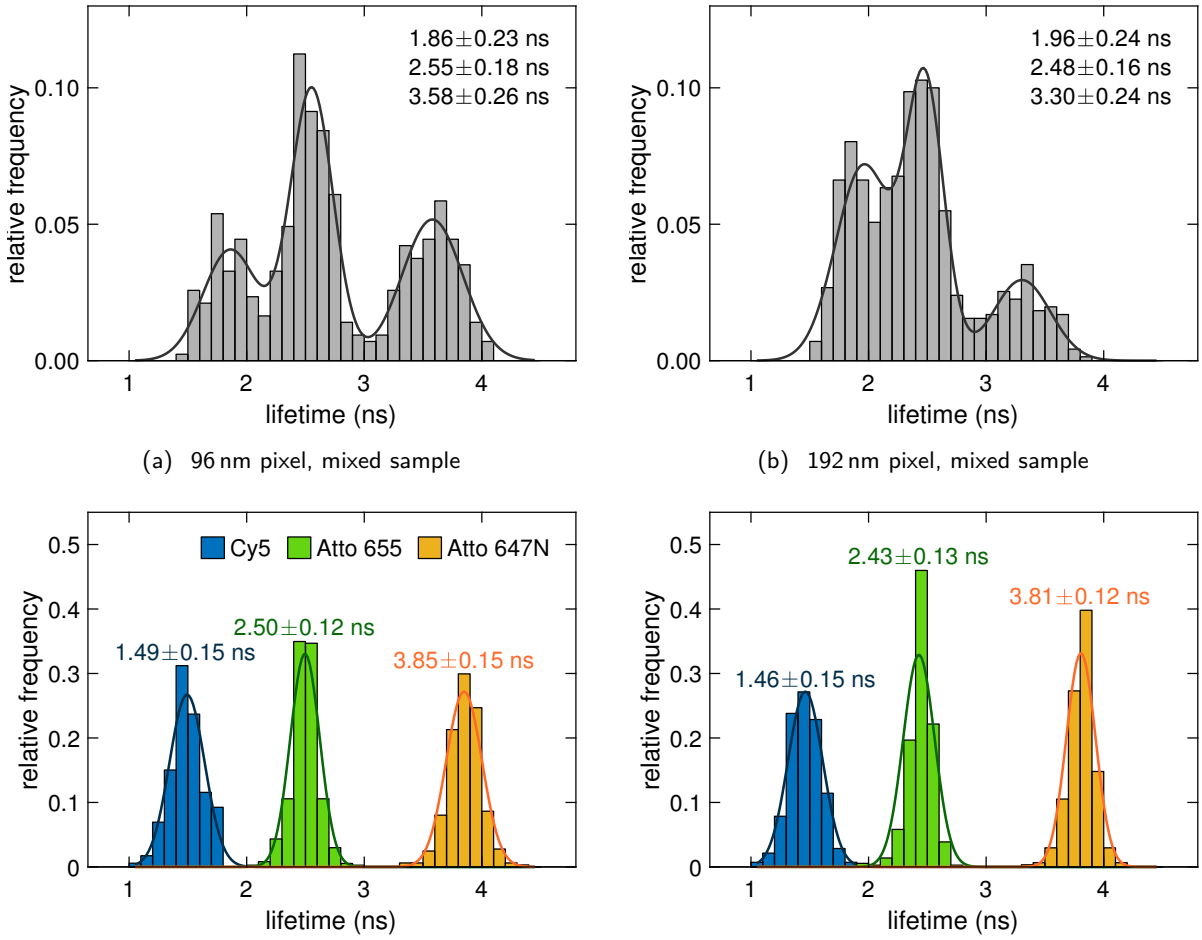

(a) 96 nm pixel, mixed sample

(b) 192 nm pixel, mixed sample

(c) 96 nm pixel, pure samples

(d) 192 nm pixel, pure samples

Figure 4.14: Influence of the virtual pixel size on the fitted single molecule lifetime for a mixed sample, (a) and (b), and pure Cy5, Atto 655, and Atto 647N samples, (c) and (d).

algorithm. As shown in figure 4.13, the on-/off-state detection algorithm substantially improves the peak separation. The algorithm reduces contributions from neighbouring molecules by rejecting photons arriving when the analysed fluorophore is in the off-state. This increases the signal to background ratio and was crucial for the correct determination of the lifetime of Cy5 which photobleached first.

Influence of the virtual pixel size on the lifetime histograms

When fluorophores with different lifetimes are densely distributed on a surface, cross-talk of emission from neighbouring molecules is unavoidable and can affect the determined lifetime values of individual molecules. We confirmed the influence of the pixel size on the cross-talk following way: lifetime images of mixed samples were divided into virtual pixels of two different sizes, 96 nm (same as for other samples) and 192 nm. For the larger pixel size, the side peaks in the lifetime histograms are shifted towards the centre, see figures 4.14(a) and 4.14(b). The pixel size had no effect on the lifetime histograms of the pure

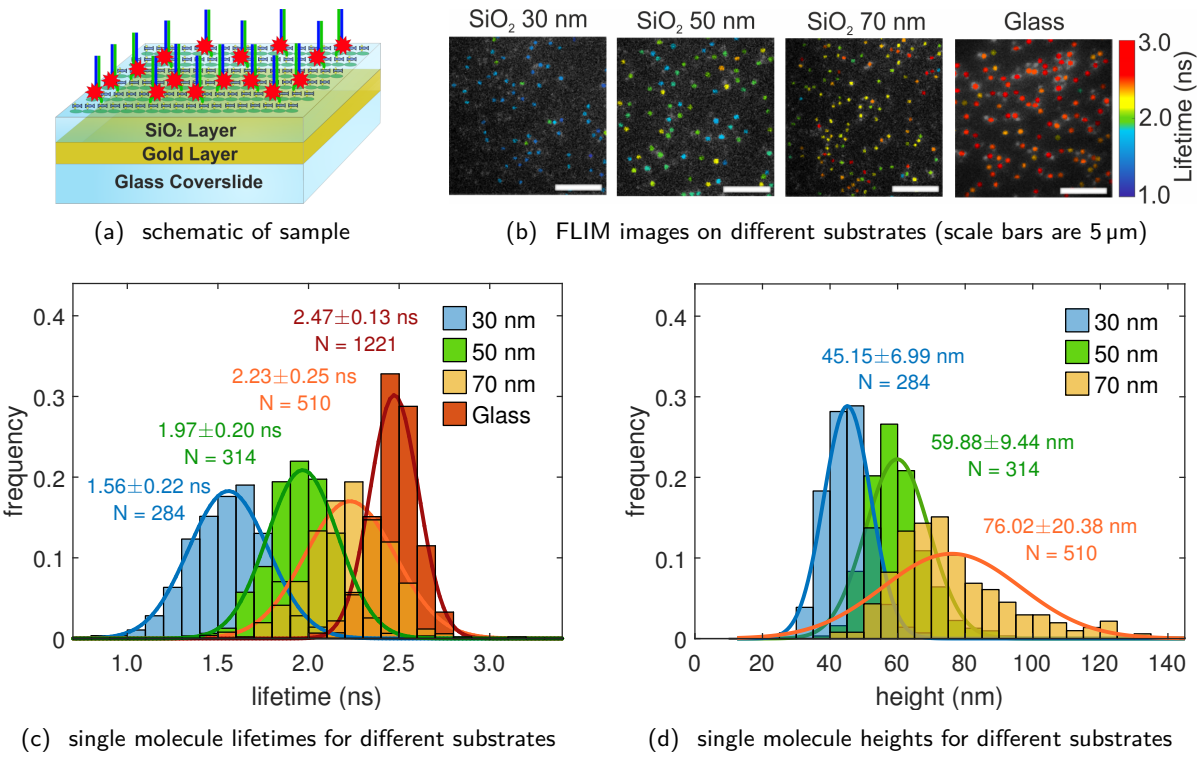

(a) schematic of sample

(b) FLIM images on different substrates (scale bars are 5 µm)

(c) single molecule lifetimes for different substrates

(d) single molecule heights for different substrates

Figure 4.15: Application of wide-field single-molecule FLIM to MIET. (a) MIET experiment design. A 10 nm gold layer and a spacer layer of SiO_2 were deposited on a cover glass. The labelled DNA-construct was immobilised on the spacer layer. (b) Exemplary FLIM images of Atto 655 fluorophores on top of a glass/gold/SiO_2 substrate for different SiO_2 layer thickness (30, 50 and 70 nm) and on a uncoated cover glass. (c) Lifetime histograms of Atto 655 fluorophores on different SiO_2 spacers and glass. The solid lines are a Gaussian fit. The lifetime histograms include data from several regions of interest. The number of molecules included in the histogram, as well as the average lifetime and standard deviation, are given next to each peak. (d) Histograms of axial positions (height values) of single molecules calculated with the MIET curve from their measured lifetime. The thickness of the BSA-biotin/neutravidin layer was assumed to be 12 nm, which adds to the SiO_2 spacer thickness. Gaussian distributions were fitted to each peak, and the average values, the standard deviations, and number of detected molecules are written next to each peak. For easier comparison, the fit results are summarised in table 4.3. Adapted with permission from *J. Phys. Chem. A* 2020, 124, 17, 3494–3500. Copyright 2020 American Chemical Society.

samples, see figures 4.14(c) and 4.14(d). Division into smaller virtual pixels could help to reduce cross-talk effects even further, but would also lead to lower photon numbers per pixel, thus increase noise and therefore decrease the localisation precision.

4.3.4 *Application of FLIM to Metal-Induced Energy Transfer (MIET)*

One attractive application of FLIM is MIET,[173] which employs the distance-dependent quenching of fluorophores in proximity to a thin metal layer. The strong and well-described distance dependence of this quenching can be used to determine the precise distance of a fluorescent molecule from the surface. When a thin gold film is used as quencher, the accuracy of this axial localisation can be as low as few a nanometres

for typical single-molecule photon numbers.[112, 113] The penetration depth of TIR excitation matches the range of the lifetime modulation by MIET. Therefore, it is advantageous to combine TIR illumination with MIET to reduce background from the bulk. This improves the signal-to-background ratio and hence the precision of the lifetime determination.

Table 4.3: Experimental and calculated lifetime and height values for the MIET experiment. The design height h_{design} contains the spacer and the BSA-biotin/neutravidin layer.

h_{design} (nm)	τ_{theory} (ns)	$\tau_{\text{experiment}}$ (ns)	$h_{\text{experiment}}$ (nm)
42	1.40	1.56 ± 0.22	45.15 ± 6.99
62	2.02	1.97 ± 0.20	59.88 ± 9.44
82	2.33	2.23 ± 0.25	76.02 ± 20.38
Glass	–	2.47 ± 0.13	–

To demonstrate the applicability of wide-field MIET measurements, we immobilised DNA-Atto 655 constructs on glass substrates that were coated with a thin gold film and topped with a SiO_2 spacer layer of well-defined thickness (figure 4.15(a)). Typical DNA-Atto 655 lifetime images with different SiO_2 spacer thicknesses are shown in figure 4.15(b). The obtained lifetime histograms are displayed in figure 4.15(c). Using the theoretical MIET curve (figure 4.16), the lifetimes were converted to heights above the surface as shown in figure 4.15(d). When assuming that the thickness of the BSA-biotin/neutravidin layer was ~12 nm,[113] we found excellent agreement between the MIET-derived height values of the single fluorophores and the height values deduced from the sample architecture, see table 4.3. From the standard deviation of the height distribution, we estimated the axial localisation precision to be ~10 nm. For the 70 nm spacer, the localisation precision was reduced to ~20 nm. The reduced precision was caused by the decreased slope of the MIET curve for heights above 70 nm.

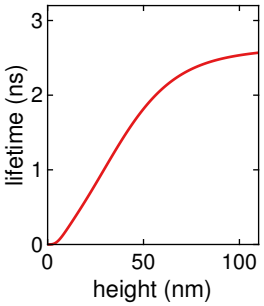

Figure 4.16: MIET curve for Atto 655 above a 10 nm gold layer.

4.4 DISCUSSION

In this work, we performed single-molecule FLIM using the novel TCSPC camera LINCam. Although the detection quantum yield of the camera is only a few percent for red light, we could clearly image single molecules and determine their fluorescent lifetimes. To the best of our knowledge, this is currently the only wide-field lifetime imaging system with a large field of view, single-molecule sensitivity, and sub-nanosecond precision in lifetime determination. We used the system to measure lifetimes of DNA-conjugated Cy5, Atto 655, and Atto 647N fluorophores and were able to determine the lifetime values of single fluorophores with experimental errors of less than 0.3 ns. Taking the low detection efficiency into account, this is an exceptionally high precision. Moreover, we could successfully differentiate between the different types of fluorophores in a mixed sample solely on the basis of their lifetime. We found that it is not only possible to identify single molecules, but also that their

obtained lifetimes matched the lifetimes of pure samples with only one species within experimental errors. We presented an implementation of an on-/off-state detection and dwell-time analysis, applied it to characterise the blinking behaviour of Atto 655, and demonstrated that the TCSPC camera is capable of capturing the blinking kinetics of single emitters. This makes the realisation of SMLM with TCSPC-based lifetime determination feasible.

In order to compare the performances of CLSM and the novel TCSPC camera LinCAM, we performed a measurement of a mixed fluorophores sample with a conventional TCSPC-CLSM and found a remarkable agreement with the lifetime values obtained with the TCSPC camera. Furthermore, solution measurements of the same sample with both systems yielded similar lifetimes. Compared to TCSPC-CLSM, the TCSPC camera has the advantage of a faster data acquisition for a large field of view. This advantage will be even more striking in the blue and green spectral regions, due to the higher detection efficiency of the camera.

Finally, we demonstrated the combination of single-molecule wide-field FLIM with MIET for the measurement of the axial position of single fluorophores with $\sim$10 nm accuracy. This is a first step towards three-dimensional SMLM by combining conventional lateral single molecule localisation with the axial localisation provided by MIET.

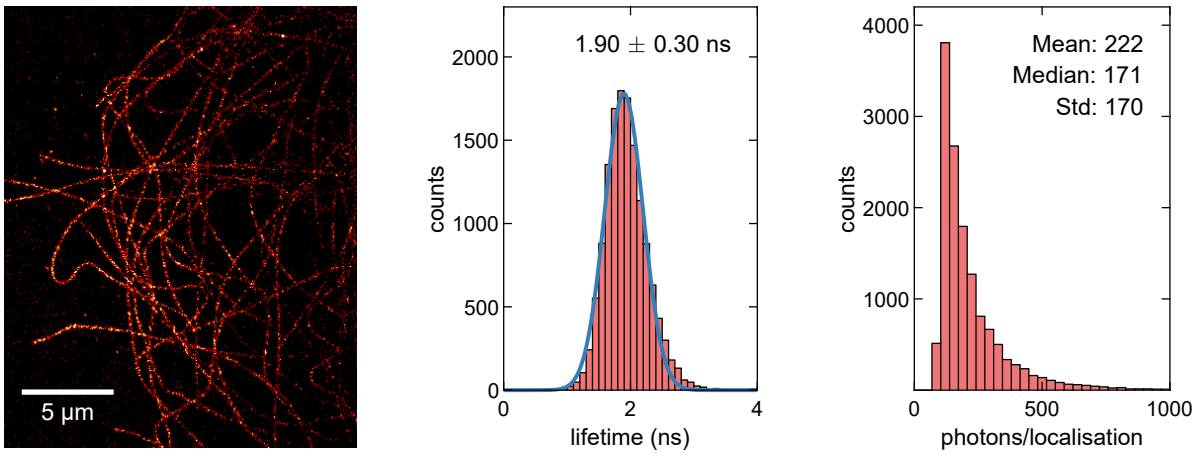

(a) reconstruction (b) lifetime histogram (c) number of photon histogram

Figure 4.17: Lifetime resolved dSTORM measurement with the TCSPC camera. (a) Super-resolved reconstruction of the localisation positions. (b) Lifetime and (c) number of photons histograms, based on individual single-molecule localisations. The sample was Alexa 647 labelled β-tubulin (COS-7) in D_2O with 10 mM MEA and was prepared by Dominic Helmerich as described in chapter 3.

4.5 OUTLOOK

Since the TCSPC camera utilises single photon detection, the frame rate is only limited by the photon count rate which makes it attractive for applications requiring high frame rates, for example lifetime-resolved wide-field SMLM, lifetime-resolved tracking, or parallel single molecule fluorescence correlation spectroscopy (FCS). In the following, two short examples are provided, giving a first impression how this could be implemented.

Lifetime-resolved wide-field SMLM

As indicated in the conclusion, it is promising to combine the TCSPC camera with SMLM and MIET to perform 3D super-resolution microscopy. Compared to the scanning confocal SMLM presented in chapter 3, the TCSPC camera is limited in count rate. Therefore, it is best suited for low localisation densities and fluorophores which can be switched at low excitation power. However, due to the wide-field detection, the field of view can be larger and it is straightforward to implement TIR-illumination, as demonstrated in this chapter. Figure 4.17 shows an example of a dSTORM measurement using the TCSPC camera. The lifetime distribution is broader than for the confocal measurement (*e. g.* compare figure 3.5(d)) due to the lower number of photons per localisation. This could likely be improved by switching to green or blue fluorophores. Nevertheless, this example showcases that the TCSPC camera is fast and sensitive enough to perform localisation-based super-resolution microscopy.

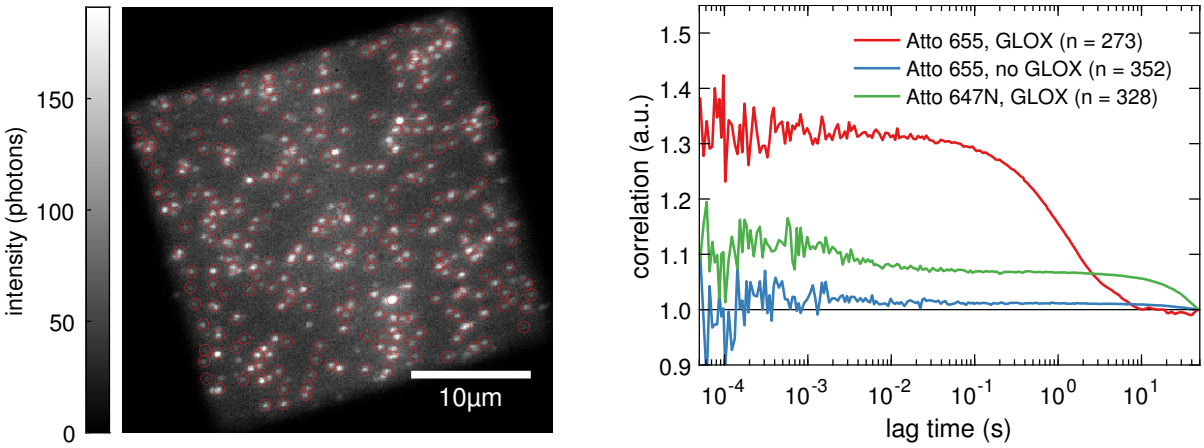

(a) Detected single molecules (Atto 655, GLOX)

(b) Correlation curves

Figure 4.18: Single molecule FCS with the TCSPC camera. (a) Detected single molecules and (b) summed single molecule correlation curve for Atto 655 with and without GLOX and Atto 647N. For easier comparison, the curves are normalised by their values at maximum lag time.

Parallel single molecule FCS

FCS of immobilised single molecules by scanning the surface is routinely used to observe transitions which are too slow to be observed in solution and too fast for a sensitive camera.[126] Since the TCSPC camera does not acquire the image in frames but records a continuous photon stream, the photon arrival times can be correlated on a molecule-by-molecule basis. Due to the parallel detection, this extends the continuously observable time range to multiple seconds, which would require extremely slow scanning on a confocal system and hence impractically long measurement durations.

Figure 4.18 shows an example of parallel single molecule FCS on immobilised Atto 655 and Atto 647N molecules. For this, the photons were correlated for each molecule separately and the correlations summed and normalised. As demonstrated in section 4.3.2, Atto 655 exhibits blinking on a timescale of several seconds in an oxygen depleted environment (with GLOX), visible as a strong decay of the correlation. For comparison, Atto 655 without GLOX results in a very flat correlation curve, indicating that almost no switching or bleaching occurs on the observed timescales. In contrast, the correlation curve of Atto 647N shows two decays, one weak decay on the millisecond timescale, probably linked to a triplet state, and one at tens of seconds caused by photo-bleaching.

This example demonstrates that wide-field single molecule FCS may be used to study dynamics ranging from milliseconds to tens of seconds within a single measurement. In some cases, the additional lifetime information may be valuable to disentangle different conformational states.[177]

5 TRACKNTRACE LIFETIME EDITION

In single-molecule microscopy, the acquired images cannot be interpreted directly but require demanding processing. The first step in processing usually is the detection of single molecules. For example, single-molecule localisation microscopy (SMLM) relies on the localisation of switching single molecules in a stack of many frames to reconstruct a super-resolved image. Wide-field single-molecule FRET, by contrast, employs the intensity time traces of the molecules.
There exists a wide variety of highly optimised software that is specialised on single molecule localisation.[178] However, none of them natively supports FLIM or TCSPC data. To facilitate single molecule localisation and lifetime fitting of TCSPC data, I extended the open-source framework TrackNTrace.[141] TrackNTrace features a plugin-based molecule detection, position refinement, and tracking, and has a visualiser to verify the analysis at each step and to examine the final results. In this chapter, the extended version, which supports TCSPC-based FLIM and single molecule lifetime fitting, is presented. With this version, the analysis, starting from the raw data to super-resolved FLIM images, is possible within one GUI-based app.

The TrackNTrace *Lifetime Edition* was published together with confocal lifetime-resolved SMLM (chapter 3) and is available on GitHub (`https://github.com/scstein/TrackNTrace`). A technical description can be found in the accompanying manual.

5.1 WHAT IS NEW?

TrackNTrace was designed to be extensible. Nevertheless, the raw data was previously limited to camera images and the import was therefore restricted to TIFF files. To support FLIM, the file import was generalised to file-type specific plugins, which have to return intensity images but can return additional data, *e. g.* lifetime images. In TCSPC-based FLIM, the arrival time of each photon relative to the excitation pulse is known. This information can be exploited for time gating, which excludes photons arriving outside of a defined time window. Time gating is useful to reduce the background from scattering or dark counts.

A TCSPC camera does not have an intrinsic frame rate, while for confocal SMLM (chapter 3) it was critical to combine multiple scans to one frame. For this reason, the option for frame binning was introduced, which controls the number of scans (confocal), time (TCSPC camera) or number of frames (camera) that are combined to one frame in the analysis.

The candidate detection, position refinement, and tracking plugins provided with the original version of TrackNTrace perform well on TCSPC-based data. After tracking, a postprocessing step was added, that can be utilised to extract the TCSPC data for each single molecule

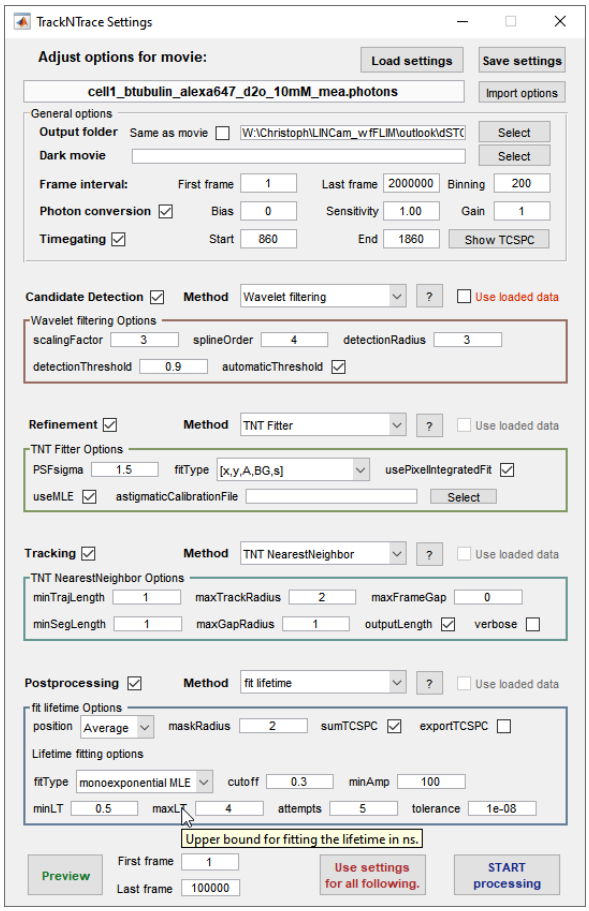

(a) Settings GUI

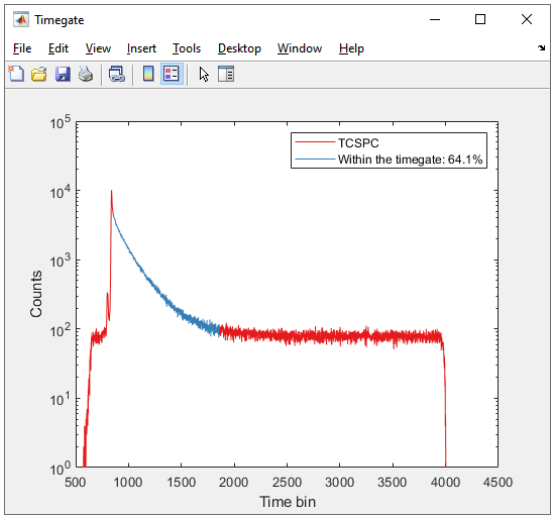

(b) Preview of timegating

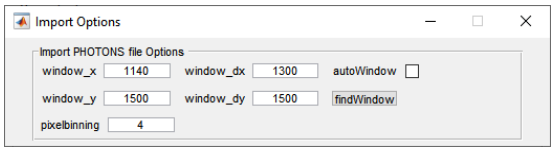

(c) Import options for TCSPC camera data

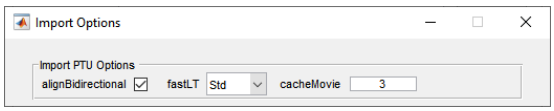

(d) Import options for TCSPC-CLSM data

Figure 5.1: In the TrackNTrace settings GUI (a) the plugins and parameters for analysis are set. All settings come with a tooltip for explanation. For TCSPC-based data, a timegate can be set and previewed (b). Each import plugin can has its own settings, *e. g.* setting the field of view, pixel size (c) or enabling correction of scanning artefacts (d).

and fit the corresponding lifetime. The extended settings GUI, including new options for frame binning, time gating, and the postprocessing step, is shown in figure 5.1(a).

The data visualiser was extended substantially: It supports FLIM images by encoding the lifetime as colour and the intensity as brightness. To avoid cross-talk between lifetime and intensity, dedicated, perceptionally uniform, isoluminant colourmaps were generated with *colorcet*.[179] An adaptive scalebar is available which uses the pixel size provided by the import plugin. The localisation data may be filtered based on any parameter. Sample drift can be corrected based on redundant cross-correlation (RCC).[143] And finally, the data may be reconstructed to create super-resolved (lifetime) images.

5.2 HOW DOES IS WORK?

The image processing starts with the file import by the import plugin. The generated or imported intensity images are passed to the candidate detection plugin to generate a list of possible localisations, which are subsequently enhanced to sub-pixel precision by the refinement plugin. These localisations can be linked to tracks in the next step. Based on the tracks, the postprocessing plugin extracts additional information, such as the lifetime. In the following, the details of file import and lifetime determination are explained.

5.2.1 *Import plugins*

The import plugins serve as interface between TrackNTrace and the raw data. All file-type specific processing is done by these plugins. In the plugin definition, the supported formats and whether the plugin supports FLIM and TCSPC are listed. Each import plugin may provide additional option as shown in figures 5.1(c) and 5.1(d). The existing support for TIFF files was transferred to a plugin, and plugins for PicoQuant's PTU format (TCSPC-CLSM) and Photonscore's PHOTONS format (TCSPC camera) were created. As TCSPC is generally based on a photon stream, these plugins may, in the future, easily be adapted to other TCSPC formats.

TCPSC-CLSM

In TCSPC-CLSM, the sample is scanned with the laser beam while the photon stream is recorded. In PicoQuant's PTU format, the time after synchronisation pulse and the number of pulses since the last overflow marker are recorded for each photon. Additionally, the stream includes overflow markers every 1024 (2^{10}) pulses, and markers when a frame or line starts or ends. Therefore, the photon stream always has to be read from the beginning, and the position of each photon needs to be calculated from the preceding number of lines and the time to the previous line start and next line stop markers.[117, 180] Because the raw photon stream does not allow random access and the processing can be time consuming, the converted photon stream (index), including position, frame, microtime (time to last pulse) and macrotime (number of pulses since start of measurement) are saved along with the raw data as a hdf5-based MAT-file which allows random access. The implementation can handle arbitrarily large raw data files, provided the data of a single frame fits into memory, by saving the already processed photons to the disk. This feature is important to enable processing of data from long dSTORM, and especially DNA-PAINT measurements. During the conversion, a correction of scanning artefact may be applied, as described on the next page.

To generate images, the photons from the chosen frame range and time gate are selected from the photon index and are accumulated in

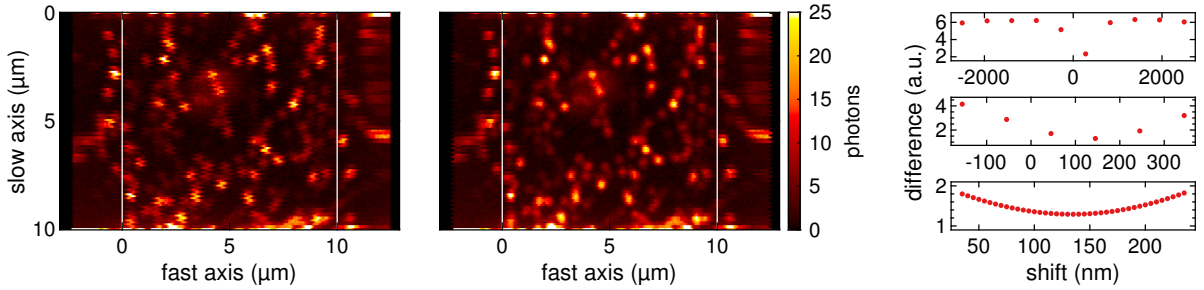

(a) uncorrected (b) shifted by 1.35 px (135 nm) (c) grid search

Figure 5.2: Correction of the shift in bidirectional measurements. (a) Uncorrected and (b) corrected intermediate image used for the correction. The white lines indicate the region included in the final images. (c) The shift is determined by a grid search with three iterations, which minimises the total squared difference between each line their adjacent lines.

`accumarry` *constructs a multidimensional array by accumulating values according to a subscript. All values with the same subscript are* e. g. *summed or averaged.*

a 3D array (x,y,t). This is implemented efficiently employing look-up tables and the MATLAB function `accumarry` and thus avoiding the much slower comparison of each element with bin edges found in histogram algorithms. For intensity images, the photons of each array element are summed, for lifetime images the standard deviation of the microtime is used as the estimator. If the photon index is too large to fit into memory or if the intermediate variables are too large, the photons are processed a few frames at a time. The resulting stack of intensity and lifetime images may be saved to a cache file (option cacheMovie) for further use, *e. g.* when visualising the results.

To allow for single-molecule lifetime determination, the plugin can extract the TCSPC histogram from specified regions of single frames. To parallelise this process, the TCSPC histograms from multiple areas are extracted simultaneously, using a mask with corresponding indices at the molecule positions.

Correction of scanning artefacts When acquiring an image with a CLSM, the area of interest is scanned line by line along the so called fast axis while advancing one step on the slow axis after each line. The lines can be scanned all in the same direction (monodirectional) or by alternating forward and reverse scans (bidirectional). Although monodirectional scanning is simpler to implement, it becomes inefficient at high scanning speeds due to the time it takes for the scanner to return to the starting position, which can be almost half of the measurement duration. Bidirectional scanning is more time-efficient but needs careful calibration to ensure that the positions in the forward and reverse scan match.

The laser scanner employed in this work (FLIMbee, PicoQuant) supports both modes, however, bidirectional scanning at high speeds produces a shift between forward and reverse scans which can be seen in figure 5.2(a). The shift depends, among others, on the scanning speed, and an internal calibration directly before the measurement. Therefore, the shift has to be corrected for each measurement individually.

The import plugin can correct the shift automatically. First, the shift is determined based on the position of the first 5 million photons or the photons of the first frame, whichever are more. Contrary to the previous position calculation, the position along the fast axis is not discretised and photons between the lines are not excluded but assigned to the nearest line. Next, an image with a pixel size of 5 nm along the fast axis is generated and smoothed with a moving average corresponding to the original pixel size along that direction. For this image, the shift between odd and even lines, which minimises the total squared difference between each line and their two adjacent lines, is determined with an iterative grid search with a final resolution of 5 nm. The image with minimal difference is depicted in figure 5.2(b) and the three iteration steps are illustrated in figure 5.2(c). The shift, converted into a time with the scanning speed, is used to offset the line start and stop markers accordingly, when generating the photon index. By performing the correction in the time domain, interpolation artefacts, and therefore a loss of resolution, are avoided.

Occasionally, some measurements additionally exhibit scanning artefacts caused by the scanner accelerating and decelerating close to the edges of the image. Correcting these artefacts would require a non-linear model and probably additional data.

TCSPC camera

The TCSPC camera (LINCam, Photonscore) records the position and arrival time (microtime, macrotime) of each photon and stores it in a PHOTONS file. Conveniently, the raw data contains an index of positions in the photon stream with millisecond resolution. Therefore, the generation of an index is not necessary and photons from an arbitrary time interval can be read directly using the photonscore toolbox.[181]

The image generation is performed similar as for TCSPC-CLSM. However, there are additional options to define field of view and pixel binning. In the experimental setup presented in chapter 4, the unbinned pixel size was ∼24 nm and only a small area of the sensor was illuminated due to the limited overall count rate. The field of view may be set automatically by the plugin based on the position of the first 10 million photons.

5.2.2 *TCSPC extraction and lifetime fitting*

For TCSPC extraction and lifetime fitting, a dedicated plugin was created for the novel post-processing step. First, the plugin extracts the TCSPC histogram of each localisation. For this, a mask containing the index of each molecule within a circle around the corresponding position is generated. The radius of the circle (option maskRadius) is defined relative to the PSF size. For each frame, this mask is passed to the import plugin which returns the TCSPC histograms. The localisation positions are either preserved, averaged over each track or refitted in a sum image of all frames of the track using the pixel-integrated Gaussian MLE fit

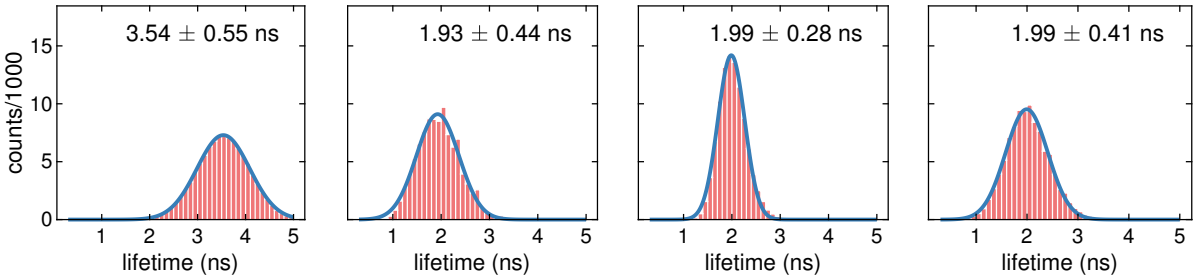

(a) standard deviation (b) distribution fit (c) MLE fit (d) correlation

Figure 5.3: Lifetime distribution obtained by applying different algorithms to 100 000 simulated TCSPC curves with a 2 ns monoexponential decay and, on average, 90 signal and 10 background photons. This example neglects any influence of the IRF and multi-exponential behaviour of some fluorophores.

from the TNT Fitter plugin. The TCSPC histograms of all localisation within one track may be summed or treated separately.

There are multiple options how to estimate the lifetime from the TCSPC histogram, differing in speed, accuracy and underlying assumptions. Figure 5.3 contains a comparison of the different algorithms for a simulated scenario with a low number of photons and 10 % uncorrelated background. To quickly estimate the lifetime, the standard deviation of the arrival times or an amplitude weighted mean of a least-square tail-fit with a distribution of multiple exponential decays may be employed. The standard deviation (figure 5.3(a)) and the least-square distribution fit (figure 5.3(b)) are biased due to the background and the low number of photons, respectively. For all tail-fits, the only the falling tail of TCSPC histogram, starting a defined time (option cutoff) after the maximum, is fitted. The position of the maximum is determined from a sum of all TCSPC histograms which have total photon number within the 25 – 75 % quantile. This filtering reliably excludes background localisations and localisation which might be affected by deadtime, *e. g.* in dSTORM before off-switching.

The third option is a monoexponential MLE tail-fit (figure 5.3(c)) which was implemented for approximately monoexponential single molecules, as observed in chapters 3 and 4. Lifetime, amplitude and background of the decay are fitted by minimising the negative log likelihood with a Nelder–Mead simplex algorithm. Contrary to a least-square fit, this ensures a bias-free estimation of the lifetime. The starting values are determined by the distribution tail-fit mentioned above, which is vital for a good performance. The plugin returns the final fit parameters and the reduced χ^2 which can, other than the likelihood, be compared for different localisations. The fit results are slightly improved by performing multiple fits with varying initial lifetime (option attempts) and reducing the termination tolerance (option tolerance).

A fit-free alternative (figure 5.3(c)) is to compute the correlation between the TCSPC histogram and a distribution of calculated monoexponential decays and select the lifetime corresponding to the decay with maximum correlation coefficient. This method is, by definition,

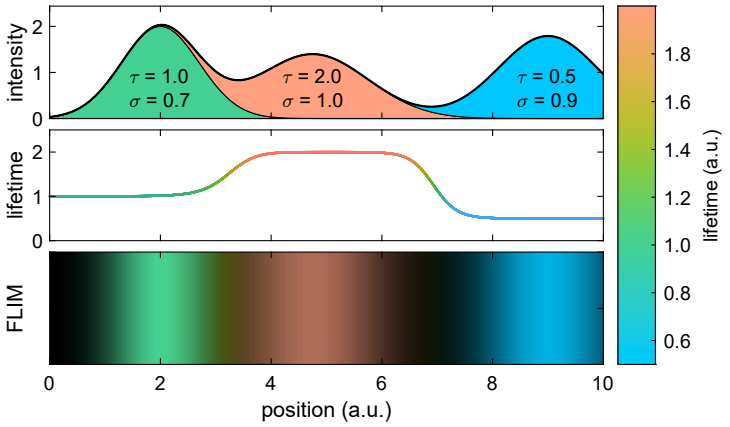

Figure 5.4: Illustration of the super-resolved FLIM image reconstruction for a simplified 1D example. Shown are three localisations with distinct lifetime τ and localisation precision σ. The reconstructed intensity is the sum of normalised Gaussians with standard deviation σ at the localisation positions. The lifetime is calculated as weighted local average of the corresponding localisation lifetimes. The FLIM image represents the intensity as brightness and the lifetime as colour.

insensitive to background and very fast since the correlation of all TCSPC histograms is calculated in parallel. The monoexponential MLE fit and the correlation recover both the correct average lifetime but the MLE fit yields a narrower distribution.

The plugin optionally saves the extracted TCSPC histograms (option exportTCSPC). This was employed for the Bayesian pattern matching described in section 3.2.9.

5.2.3 *Image reconstruction*

The reconstruction is performed directly by the visualiser. The default option draws a normalised, pixel-integrated Gaussian distribution at each localisation position. The standard deviation can either be fixed or set to the corresponding localisation precision, which is calculated from the amplitude and width of the fit to the PSF.[67] Additionally, an image can be reconstructed for any parameter, *e. g.* the localisation's lifetime for super-resolved FLIM images. For the parameter of choice, the local weighted average is calculated. As weight, the same Gaussian distributions is used. This is illustrated in figure 5.4 for the lifetime. Multichannel images are reconstructed by applying the corresponding filter for each channel separately.

5.3 EXAMPLES

TrackNTrace was used for data processing in chapter 3 and also for the demonstration of lifetime-resolved wide-field dSTORM in section 4.5. The following examples illustrate its versatility by revisiting previously shown data and analysing them with TrackNTrace exclusively.

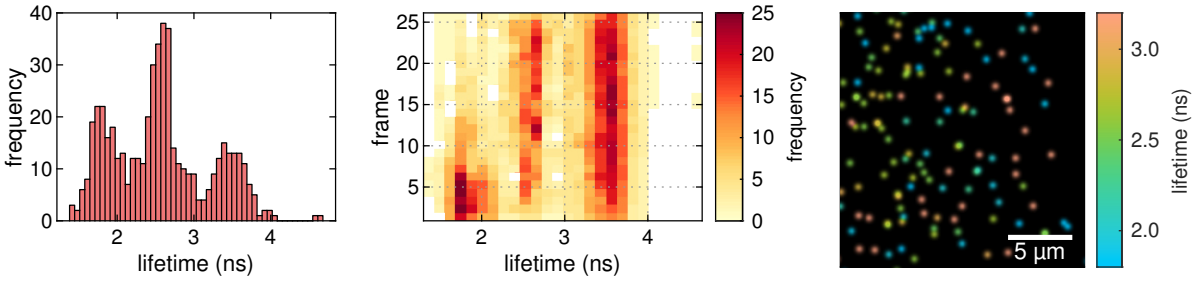

(a) lifetime distribution (b) frame-wise lifetime (c) reconstruction

Figure 5.5: Analysis of wide-field FLIM data from an immobilised mixture of three different fluorophores (Cy5, Atto 655, Atto 647N) with TrackNTrace. The lifetime distribution (a) has three distinct maxima, one for each fluorophore.The 2D histogram (b) shows the lifetime distribution for each frame. It can be seen that the fluorophores with short lifetime (Cy5) photobleached first. In (c), a reconstruction with a Gaussian PSF ($\sigma = 180\,\text{nm}$) is shown. For the analysis, the measurement was divided in 2 s frames and 120 nm pixels. The localisation and lifetime data was not filtered and the plots are generated by TrackNTrace.

5.3.1 *Wide-field single molecule FLIM*

In chapter 4, the single-molecule sensitivity of a novel TCSPC camera was verified and it was demonstrated, that an on-/off-state detection enhances the precision of the observed single-molecule lifetime (figure 4.13) by excluding the contribution of the background and neighbouring molecules when the molecule is either bleached or switched off. A similar result is achieved within TrackNTrace by dividing the measurement into frames, localising the fluorophores in each frame, and then merging localisations at the same position, employing the tracking plugin with gap closing. The lifetime fitting plugin accumulates the TCSPC histograms over all frames in which the molecule was detected and fits the single-molecule lifetimes. Even tough this analysis simpler than our approach in chapter 4, it retrieves a lifetime distribution with three distinct peaks (figure 5.5(a)) from data of a mixture of three fluorophores. The 2D histogram (figure 5.5(b)) reveals the change in the lifetime distribution over the course of the measurement. Fluorophores with a short lifetime (Cy5) are photobleached within the first frames, while Atto 655 and Atto 647N have a higher photostability.

5.3.2 *Lifetime-resolved confocal dSTORM*

The typical workflow for refining analysed measurements starts by filtering the localisations, *e. g.* based on the standard deviation σ and amplitude of the fitted Gaussian PSF. This is illustrated in figure 5.6. To determine suitable thresholds, the histogram and data-tip function, a legend containing all available information of a given localisation, are indispensable tools. If fluorophores are not switched off before the measurement, the localisations in the first frames need to be excluded. A typical filter and its effect on the reconstruction are shown

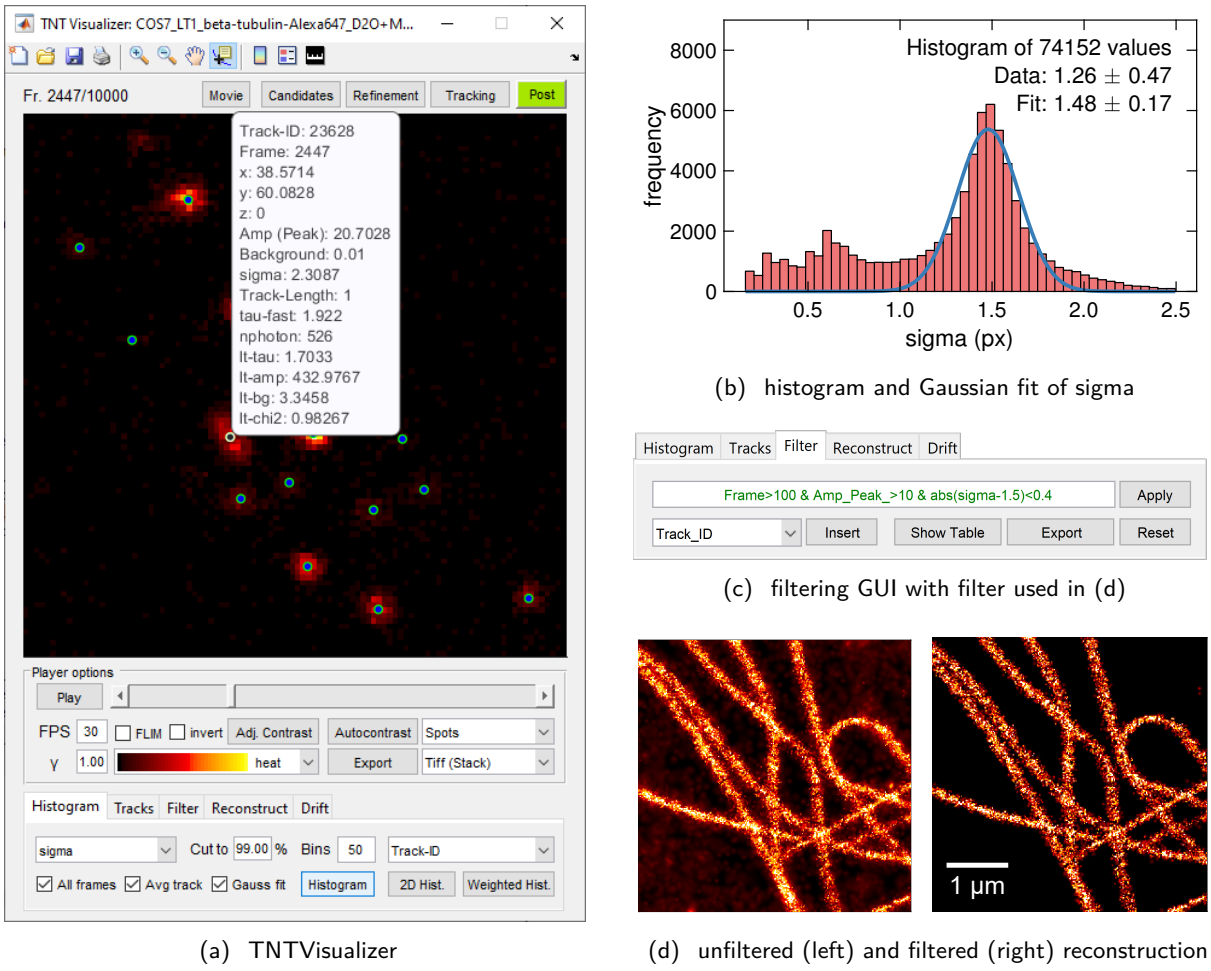

(a) TNTVisualizer

(b) histogram and Gaussian fit of sigma

(c) filtering GUI with filter used in (d)

(d) unfiltered (left) and filtered (right) reconstruction

Figure 5.6: Inspecting an analysed measurement of Alexa 647 labelled microtubules (COS-7) with the TNTVisualizer. (a) The data-tip shows the parameters of the selected localisation. In this case, the asymmetric shape and the larger fitted sigma indicate that the localisation seems to fall in between two adjacent molecules. (c) The histogram reveals that most localisations have a sigma close to 1.5 px. This enables to remove many multi-emitter and background localisations by filtering (c). The reconstruction of the filtered localisation (d) has much less artefacts at intersecting microtubules and virtually no background.

in figures 5.6(c) and 5.6(d), respectively. The reconstruction of the filtered localisations shows strongly reduced artefacts by accidental multi-emitter localisations at intersecting or neighbouring structures and less background compared to the unfiltered reconstruction.

Depending on the measurement duration and the mechanical stability of the microscope, drift correction may be necessary. For this, redundant cross-correlation (RCC) [143] was integrated into the visualiser. The sample drift can be calculated, plotted and corrected, while all input parameters of the algorithm are accessible in the GUI. Even though there are newer algorithms,[182] which can achieve a higher precision in some cases, RCC is widely used due to its simplicity and robustness.[127, 183, 184] Figure 5.7 shows an example of how the correction removes artefacts from sample drift. The colour-coded reconstructions are created by the same function as for super-resolved FLIM,

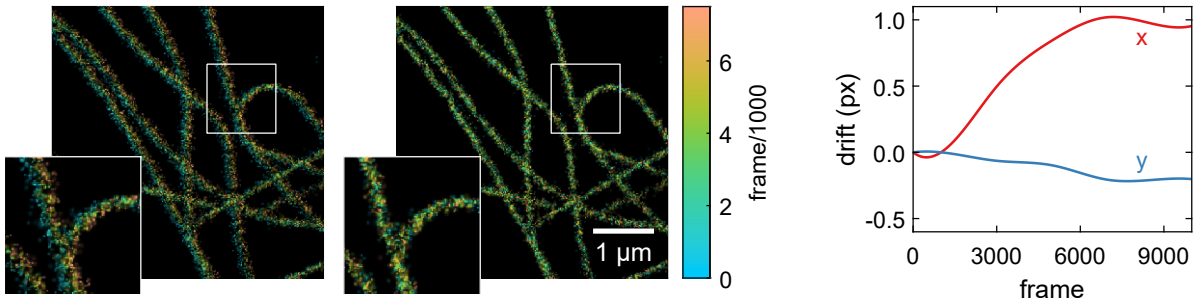

(a) before drift correction (b) after drift correction (c) drift calculated with RCC

Figure 5.7: Drift correction with RCC. The colour gradient in (a) across the microtubules in the horizontal direction indicates that there was sample drift during the measurement. This is corrected by calculating the drift with RCC and shifting each localisation accordingly. In this example the drift was calculated for segments of 2000 frames and interpolated.

however, by selecting the frame number of the localisation instead of its lifetime as parameter.

5.4 CONCLUSION

The TrackNTrace *Lifetime Edition* was essential for optimising the confocal SMLM measurements in chapter 3. It allowed for fast and systematic data evaluation and made inspecting the results straight forward. Moreover, it enables anyone with a suitable CLSM to analyse lifetime resolved SMLM measurements and achieve super-resolved FLIM without the need for any programming experience.

After the development had started, two noteworthy software packages were introduced: *SMAP* (Superresolution microscopy analysis platform),[183] which is also plugin-based and could have served as more modern basis for development, and *FLIMJ*,[185] an ImageJ plugin for analysis of TCSPC-data, which might be combined with ThunderSTORM.[138] Due to the plugin based architecture of TrackNTrace with a clear separation of different functions, a transfer of required functionalities to another software package is simple.

The presented version of the lifetime fitting plugin supports simple, but reliable options for tail-fitting of the TCSPC histogram. In future, this might be extended to include the IRF and potential solution contributions. In section 3.5, proof-of-concept experiments for the combination of MIET and SMLM for lifetime-based 3D localisation were presented. To facilitate the analysis of MIET-SMLM measurements, the conversion of the lifetime into an axial position may be integrated directly into the lifetime fitting plugin.

6 OTHER CONTRIBUTIONS

In this chapter, several other projects I have worked on are presented. They are related to fluorescence spectroscopy, but are not based on single molecule localisation.

Projects

6.1 DYNAMICS OF TETHERED POLYMERS AND POLYMER BRUSHES

Many brush-like structures are critical for biological processes. They take a variety of shapes, ranging from the actively-driven ciliated carpets on the micro scale to the endothelial glycocalyx layer covering the inner lumen of blood vessels on the nano scale.[186, 187] Also in material science, polymer brushes are employed for biomimetic and stimuli-responsive surfaces.[188, 189] In all of these cases, the interaction of the brush with the fluid environment is critical to the overall surface properties. To better understand these interactions on the level of single polymer chains, molecular dynamics simulations of a brush have been performed by Pastorino and Müller.[190] One remarkable result was a backflow of a physisorbed species inside the brush under shear flow. Aim of the presented project was to experimentally characterise the dynamic behaviour of tethered polymer chains, covering the transition from non-interacting single chains to a dense polymer brush.

This collaborative work was part of the SFB937 project A05 *Polymer brushes in motion*.

6.1.1 *Methods*

Tethered DNA-sample

Microfluidics Flow channels with a cross section of $500 \times 10\,\mu m$ were fabricated by soft-lithography of an optical glue (NOA81, Norland). This method was adapted from Bartolo et al. [191] to allow for a glass top and coated glass bottom design. The structure was moulded from an SU-8 master wafer with PDMS (SYLGARD 184, Dow Corning). The PDMS structure was inverted by moulding it again with PDMS. This PDMS master was cast with NOA81. The NOA81 was partially cured by UV illumination and transferred onto a gold coated cover glass. Holes for in and outlet were punched with a medical biopsy puncher ($\varnothing 1.5\,mm$, Integra Miltex). NOA81 ports were moulded and

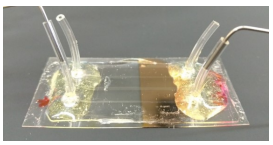

Figure 6.1: Microfluidic device for flow measurements.

Table 6.1: DNA sequences and modifications

name	5′ modification	sequence 5′ → 3′
fluorophore	Atto 647N	TGGATTAAAAAAAAAAAAAAAAAAAAAAAAAAAAAAAATGGATATTTTCTTCACAAACCAG TCCAAACTATCACAAACTTA
attachment 1	biotin	TTTAAGTTTGTGATAGTTTGGACTGGTTTGTGAAGAA
attachment 2	amine	TTTAAGTTTGTGATAGTTTGGACTGGTTTGTGAAGAA

partially cured using tubing and PDMS as template and transferred to the punched holes. The assembled device was completely cured using UV illumination. Finally, tubing (ID 0.51 mm, Tygon ND 100-80, Saint-Gobain) was glued to the ports with two component epoxy (5 Minute Epoxy, Devcon).

The structure and master wafer were originally designed and fabricated by Mira Prior for a different project.

DNA immobilisation The DNA-constructs were designed and prepared by Roman Tsukanov. The construct has a 10 base pair double stranded part and a 21 bases single stranded part. It was prepared by hybridising a short end-modified (Biotin or Amine) attachment strand with a longer fluorophore terminated strand. This was achieved by mixing equimolar amounts of both strands (1 µM final concentration) in PBS and annealing it at 94 °C for 5 min, followed by a cool-down to room temperature over 30 min. The sequences are listed in table 6.1. For the immobilisation of the resulting DNA-construct, two different approaches were used.

A BSA-NeutrAvidin based immobilisation, similar to the immobilisation in chapter 4, was adapted from Isbaner et al. [113] to the use in a microfluidic channel. First, 40 µL of a 1 mg/mL BSA-biotin (biotin labelled bovine serum albumin, Aldrich, A8549) solution in buffer A (10 mM Tris adjusted to pH 8.0, 1 mM EDTA, 100 mM NaCl) were flushed into the channel with a syringe and incubated for 40 min. The channel was washed with 80 µL of buffer A and subsequently filled with 40 µL 0.5 mg/mL NeutrAvidin (Thermo Scientific, 31000) solution in buffer A which was incubated for 20 min. The channel was washed with 80 µL of buffer A and 40 µL of the biotin-modified DNA-construct (2 nM) in imaging buffer (10 mM Tris adjusted to pH 8.0, 1 mM EDTA, 40 mM NaCl, 2 mM Trolox) were flushed in and incubated for 20 min. Finally, the channel was washed with 80 µL imaging buffer. All steps were performed at room temperature and flow was controlled with a syringe pump at a maximum flow rate of 2 µL/min.

The alternative immobilisation method was based on a silane-functionalisation of the surface. This approach is similar to Chrisey, Lee and O'Ferrall [192] and Oh et al. [193] but relies on different functional groups to ensure compatibility with the device fabrication. First, the gold coated glass cover slides were treated with air plasma (setting high, PDC-002, Harrick Plasma) for 20 s which was followed by incubation in (3-mercaptopropyl)-trimethoxy-silane (Aldrich, 175617) vapour at low pressure in a desiccator for 25 min (5 min evacuation

+ 20 min incubation with closed valve). Microfluidic channels were fabricated on top of the silane coated cover slides as described above. The annealed, amino-terminated DNA-construct was incubated with an equimolar amount of sulfo-GMBS (N-[γ-maleimidobutyryloxy]-sulfosuccinimide ester, Thermo Scientific, 22324) in a shaker at 30 °C for 150 min to introduce a maleimide modification. The channel was flushed with 15 µL maleimide-modified DNA-construct (500 nM in imaging buffer), followed by 60 µL imaging buffer both with constant a flow rate of 0.5 µL/min.

All DNA-samples were freshly prepared directly before the measurement. The flow during the measurement was generated with a computer controlled syringe pump (neMESYS 290 N, Cetoni) in combination with glass syringes (GASTIGHT 1000 Series, Hamilton).

Grafted polymer samples

The grafted polymer surfaces with varying density were prepared by Katharina Hendrich (Institute of Physical Chemistry, Georg-August-University Göttingen) and details on the synthesis can be found in her thesis.[194] The polymer was synthesised with a surface-initiated reversible addition-fragmentation chain transfer (SI-RAFT) polymerisation which allows for control of grafting density and polymer chain length. Briefly summarised, gold coated cover glasses were modified with an amine group and a RAFT-agent was bound to the amino group *via* an activated carboxyl group. The RAFT-agent concentration, reaction time, and temperature controlled the amount of RAFT-agent on the surface and therefore the final grafting density. The actual polymerisation was started by the addition of the monomer 2-(dimethylamino)ethyl methacrylate (DMAEMA), unbound RAFT-agent and a radical initiator. The molecular weight of the resulting polymer PDMAEMA was controlled by the reaction time. Finally, the RAFT agent was removed by an aminolysis which resulted in thiol groups at the chain ends. These thiol groups were exploited to attach maleimide modified Atto 655 fluorophores.

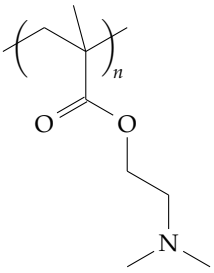

Figure 6.2: Chemical structure of PDMAEMA. The tertiary amine can be protonated at low pH resulting in a positive charge.

Data acquisition

All fluorescence measurements were carried out on a custom-built confocal microscopy setup equipped with a laser scanner and hardware for TCSPC detection which is described in detail in section 3.2.1. Additionally, the fluorescence emission was split after the pinhole with a non-polarising 50:50 beamsplitter and collected by two identical SPAD-detectors.

An overview measurement ($80 \times 80\,\mu m$) was acquired with a fast scan rate ($\sim 1\,m/s$). Subsequently, several smaller areas ($\sim 30 \times 30\,\mu m$) were scanned at a slow scan speed ($\sim 5 \times 10^{-4}\,m/s$). For densely labelled samples, each area was scanned up to five times. This was repeated at different positions on the sample.

Fluorescence lifetime The fluorescence lifetime was determined for each area by fitting the corresponding TCSPC histogram with a multi-exponential model. To exclude surface inhomogeneities like aggregates and contaminations, only photons from pixels with an intensity in the central 60 % were further analysed. The remaining pixels were partitioned into 10 groups and for each group the corresponding TCSPC histogram was accumulated and fitted. The tail of each TCSPC histogram, starting 0.5 ns after the maximum, was fitted with three exponential components. The decay times were fitted using a Nelder–Mead simplex algorithm to minimise the negative log-likelihood function, while the amplitudes of exponential components and background were determined with a non-negative constrained PIRLS (Poisson iteratively reweighted least squares) solver.[195] The initial lifetime values were set to 0.2, 1 and 3 ns. The fast decay component was necessary to account for scattering by the gold surface. The reported lifetimes (figures 6.5 and 6.8) are the amplitude weighted average of the second and third component.

thickness	material
30 nm	Si_2O
1 nm	Ti
10 nm	Au
2 nm	Ti
∞	glass

Table 6.2: Material stack used for the calculation of the MIET curve.

The resulting lifetimes were converted into a height above the surface with the corresponding MIET curve. The MIET curves were calculated using the specific sample geometry (table 6.2). A measurement from an area without metal coating was used to determine the free space lifetime of the fluorophore. For the polymer brush samples, the brush thickness, instead of the fluorophore height, was estimated from the lifetime by modelling the distribution of fluorophores as described in the Results & Discussion section.

Fluorescence correlation spectroscopy The correlation between the photon arrival times at the two detectors was calculated with an algorithm for single-photon time-correlation.[196] This analysis was performed for each scanned line of the measurement independently.

For the tethered DNA measurements, correlation curves of the lines were alternatingly dived into 10 groups and each group summed and normalised by dividing by the value at maximum lag time. The correlation curves were fitted with the sum of one $\propto \exp(-(t/\tau)^2)$, three $\propto \exp(-t/\tau)$ components, and a constant background. Here, t denotes the correlation lag time and τ the decay time of each component. The fitting was performed by minimising the χ^2 error with a Nelder–Mead simplex algorithm.

For the polymer brush measurements, the correlation curves of each area were summed, cropped ($t < 2 \times 10^{-5}$ s), normalised by dividing by the value at the maximum lag time and fitted with two exponential components and constant background as described above.

6.1.2 *Results & Discussion*

Tethered bio-polymers in flow

With an adsorption based strategy, a homogenous immobilisation of DNA-constructs inside a microfluidic channel was achieved. The DNA-

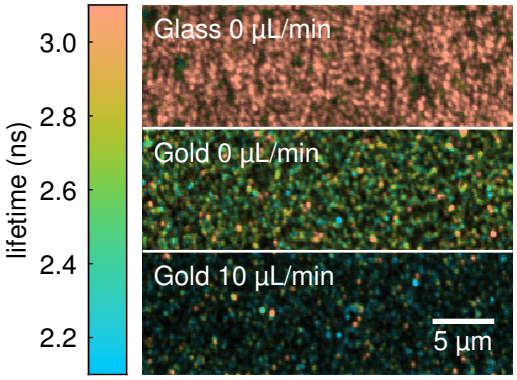

Figure 6.3: FLIM images of tethered DNA on glass or gold in a microfluidic channel.

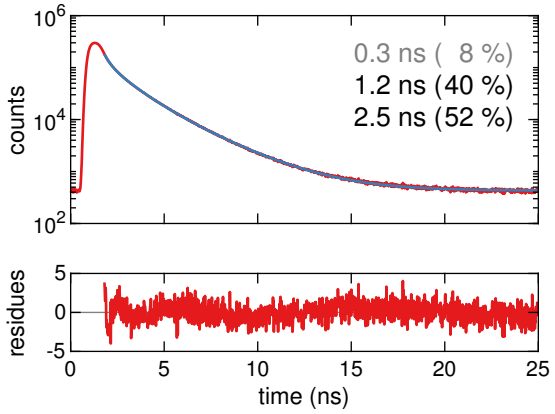

Figure 6.4: TCSPC histogram and lifetime fit for the sample on gold without flow.

constructs exposed a DNA single strand, terminated with a fluorophore, to the fluid and the microfluidic channel allows to apply a controlled flow field. The channel was fabricated from a UV curable optical glue. Opposed to the more common material PDMS, it is very rigid when cured and therefore does not deform when applying the high pressures which are required for high shear rates at the surface. Additionally, it may also be bonded to modified surfaces such as the synthetic polymer brush.

In figure 6.3, FLIM images of the sample surface can be seen. The quenching effect of the gold coating and a further lifetime reduction by the flow is directly apparent. To exclude aggregates or contaminations, only pixels with a brightness in the centre 60 % quantile were taken into account. The lifetime was determined from a MLE fit with three exponential components (figure 6.4). The short component, caused by scattering and auto-fluorescence, was present at all conditions. The further analysis is based on the the weighted average lifetime of the two long components.

The lifetime measurements at different flow rates (figure 6.5(a)) exhibit a systematic decrease in lifetime with increasing flow rates. Using the measurement on glass as reference for the unquenched dye, the MIET-curve (figure 6.5(b)) for a freely rotating dye was calculated. To convert the flow rate into the shear stress acting on the surface, the flow field was calculated numerically utilising the approach presented in section 6.2 and the shear rate at the surface was multiplied by the dynamic viscosity of water at 20 °C. The height of the chain end above the surface in dependence of the shear stress is shown in figure 6.5(c). The decrease in height can be interpreted as the chains being dragged along by the flow, bringing the chain end, on average, closer to the surface. It is evident that the curve saturates at approximately 17 nm, which is likely the thickness of the BSA-NeutrAvidin immobilisation layer. Spaeth, Brecht and Gauglitz [197] reported a thickness per BSA-NeutrAvidin layer of 18.75 nm for an alternating deposition of BSA and poly-streptavidin by ellipsometry. In earlier MIET experiments, the

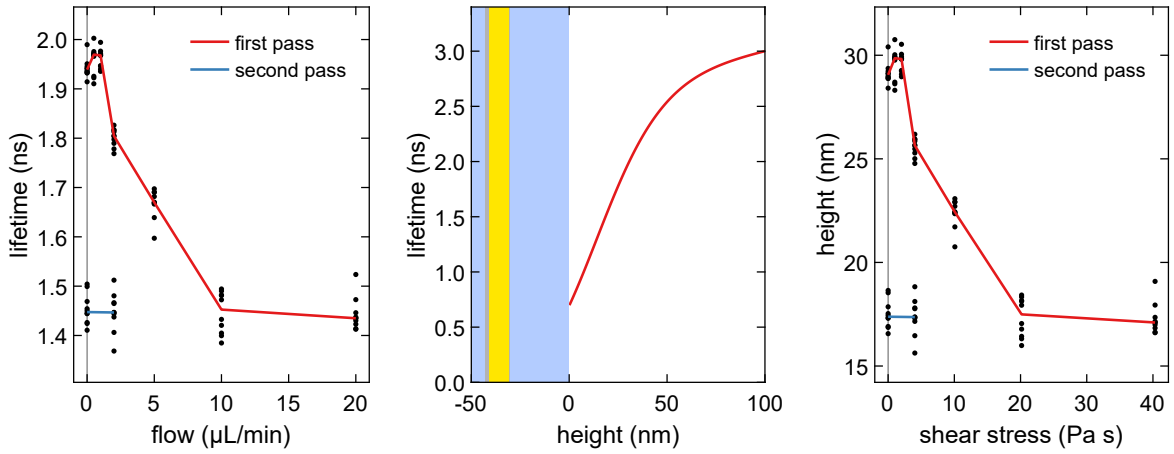

(a) flow dependant lifetime (b) MIET curve (c) shear dependant height

Figure 6.5: (a) Fitted lifetime for different flow rates. The flow rates were measured in increasing order (first pass) before starting again at 0 (second pass). For each measurement 10 different TCSPC histograms were fitted (black markers), the line connects the median values. (b) MIET curve for Atto 647N. (c) Height above the surface for different shear stresses. The height was calculated from the lifetimes using the MIET curve, the shear stress from the flow rate with the dynamic viscosity of water and a numerically calculated flow profile.

immobilisation layer thickness was estimated to be 15.8 nm.[109]

The flow rates were measured in increasing order (first pass), before starting again at zero flow. This second pass revealed that the sample was changed by the first pass. A possible explanation could be flow-induced sticking of the DNA or fluorophore.

As explained in section 2.3, MIET does not solely affect the fluorescence lifetime but also the brightness. A height fluctuation therefore leads to a lifetime and brightness fluctuation. To robustly determine a lifetime, several hundred photons are required, making it impossible to investigate phenomena on the sub-millisecond timescale. The brightness fluctuations however may be analysed using fluorescence correlation spectroscopy. To avoid artefacts by detector after-pulsing and to access timescales shorter than the electronic dead time, the cross-correlation between two detectors, receiving both half of the photons, was analysed.

Figure 6.6(a) shows the correlation curve of a measurement on gold. The strong decay on the millisecond timescale is caused by the scanning of the beam over the surface. As scanning is conceptually similar to a measurement in a constant flow, this decay can be described in the same way with a $\sim \exp(-(t/\tau_{\text{scan}})^2)$ term. The decay time of this component τ_{scan} is depends on the scanning speed and focus size. Its amplitude is approximately the reciprocal average fluorophore number in the focus. Since almost all DNA-constructs were labelled, the grafting density was estimated to be on the order of $10^{-4}/\text{nm}^2$ which excludes direct interactions between the chains.

The correlation curves were fitted with the sum of the scanning component and three exponential components. The decay times and amplitudes of the fit components are shown figure 6.6(b). The measure-

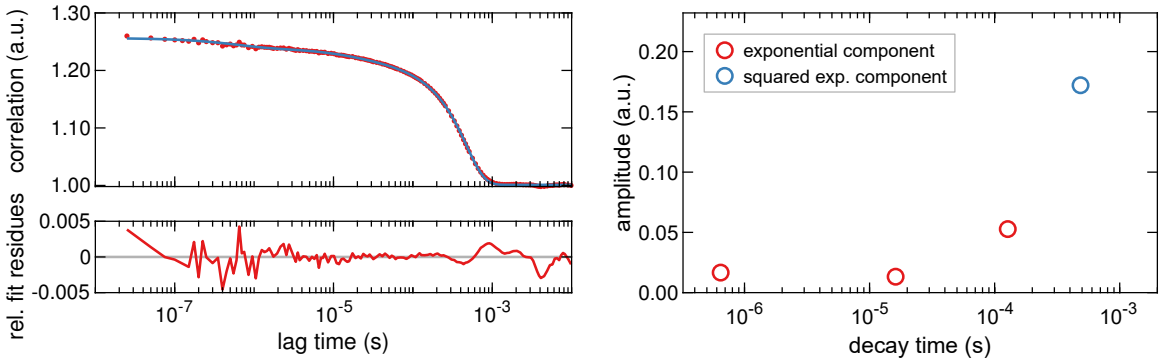

(a) FCS curve and fit

(b) fit components

Figure 6.6: (a) Correlation curve (red) and fit (blue) for tethered DNA sample on gold without flow. The fit is the sum of 3 exponential components (red) and one squared exponential component (blue) shown in (b).

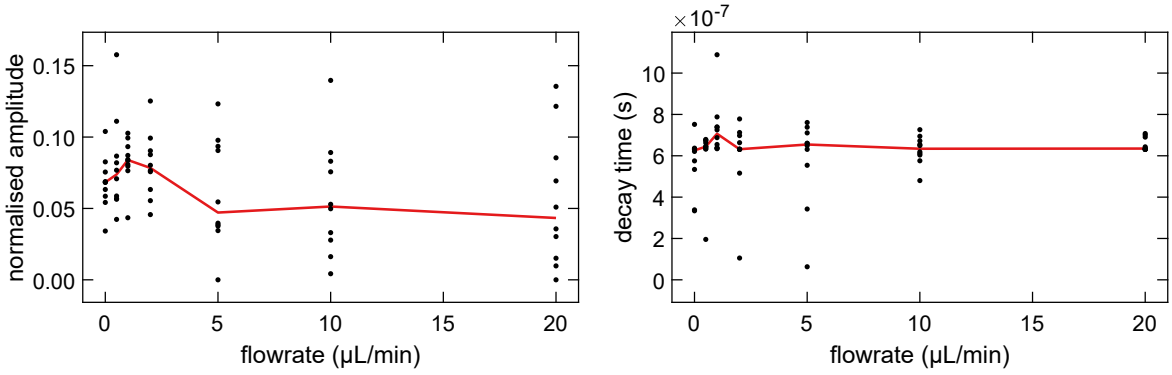

(a) amplitude fastest component

(b) decay time fastest component

Figure 6.7: Normalised amplitude (a) and decay time (b) of the fastest component from fits of the correlation curve at different flow rates. Each measurement was divided into 10 parts which were fitted independently (black marker), the line connects the median values.

ment buffer contained TROLOX, a common triplet quencher. Nevertheless, the decay on the 10^{-5} s timescale is likely caused by triplet state dynamics. The slower exponential component ($\sim 10^{-4}$ s) might be an artefact from the scanning or some slow interactions of the dye with the environment like transient sticking. The most interesting component is the fast component ($<10^{-6}$ s). At this timescale, the vertical diffusion is expected as shown by Brownian dynamics simulations by Mühle [198]. As forces exerted by the flow should influence the vertical motion of the chain end, it is expected to change the timescale and amplitude of this fastest component. The fit results of this component at different flow rates are shown in figure 6.7. The fit results vary substantially between the data from each flow rate. Therefore, no clear trend is apparent in the decay times. The amplitudes might decrease slightly with increasing flow rate. This is expected from a reduced range of vertical motion when the chain is close to the surface. However, it is not possible to disentangle this hydrodynamic effect from an increasing sticking fraction

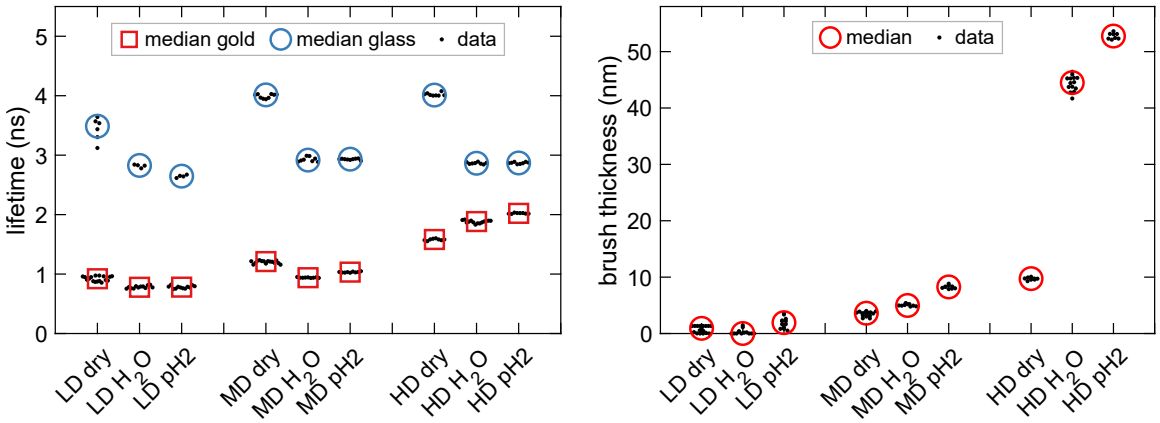

(a) average lifetime on glass and gold

(b) brush thickness

Figure 6.8: MIET measurements of three brush samples with low (LD), medium (MD) and high (HD) grafting densities under three conditions, dry and swollen with dH_2O at neutral and low pH. For each sample and condition at least eight areas were measured. (a) Weighted average lifetimes of a multi-exponential fit for all areas (black) and median values on gold (red) and glass (blue). (b) Brush thickness calculated from quenching using a molten (dry) or swollen brush model. See footnote in table 6.3 concerning LD sample.

of molecules.

In multiple attempts, including ones with exactly the same or completely fresh materials, the shown measurements could not be fully reproduced. With a silane based immobilisation instead of the BSA-NeutrAvidin immobilisation, a similar flow dependency of the lifetime, but again no clear effect on the correlation curve were observed.

Previously, other methods have employed energy transfer to measure the forces acting on surface tethered DNA using fluorescence. Basler et al. designed a FRET-sensor measuring small forces on a surface exerted by local air flow.[199] Quenching by a gold layer is also used by the commercial switchSENSE system (dynamic BIOSENSORS, Martinsried) which uses the intensity response to an applied voltage to determine hydrodynamic properties of the attached DNA and potentially bound proteins.

From single chains to polymer brushes

The tethered DNA samples investigated so far had a low grafting density, effectively preventing any interactions between the single chains. In this section, measurements where the grafting density was increased in three steps from weakly interacting to strong stretching of the polymer chains are presented. In the following, these samples are referred to as low (LD), medium (MD) and high (HD) grafting density. To adjust the grafting density, the pH-responsive polymer PDMAEMA was polymerised directly on the surface using a controlled radical polymerisation. The resulting grafting densities and molecular weights are provided in table 6.3. To avoid fluorophore-fluorophore interactions, only a small fraction of the chain ends was labelled with Atto 655.

The lifetimes, displayed in figure 6.8(a), were measured in the same

Table 6.3: Lifetimes and brush thickness for different densities and conditions. Given is the median and standard deviation of at least eight areas. The swelling ratio (SR) is the ratio between the dry and swollen brush thickness measured by MIET. The number-average molar masses $\overline{M}_n$, grafting densities σ and thickness values obtained by ellipsometry were provided by Katharina Hendrich.[194]

sample	$\overline{M}_n$	σ	condition	lifetime (ns)		thickness (nm)		SR
	(kg/mol)	(nm^{-2})		gold	glass	MIET	ellips.	
LD	13	0.09	dry	0.92 ± 0.04	3.49 ± 0.19	$0.9 \pm 0.6^*$	1.4	–
			H_2O	0.78 ± 0.02	2.83 ± 0.03	$0.0 \pm 0.5^*$	–	0.0^*
			pH2	0.78 ± 0.02	2.65 ± 0.02	1.9 ± 1.0	–	2.1^*
MD	23	0.19	dry	1.21 ± 0.02	4.01 ± 0.04	3.6 ± 0.4	5.2	–
			H_2O	0.94 ± 0.01	2.92 ± 0.04	5.0 ± 0.2	–	1.4
			pH2	1.03 ± 0.01	2.93 ± 0.01	8.3 ± 0.3	–	2.3
HD	25	0.39	dry	1.58 ± 0.02	4.01 ± 0.03	9.7 ± 0.2	12.0	–
			H_2O	1.88 ± 0.02	2.86 ± 0.02	44.5 ± 1.4	–	4.6
			pH2	2.02 ± 0.01	2.87 ± 0.01	52.8 ± 0.5	–	5.4

* For some of the areas, the resulting brush thickness value was at the lower bound (0 nm) of the reasonable fit range, therefore these values might not be reliable. This also applies to the swelling ratios calculated from the thickness.

fashion as described for the tethered DNA. It is evident that the lifetime on glass drastically changes after swelling the brush. Therefore, the conversion of lifetimes to heights relies on dedicated models. The quantum yield of the fluorophore changes after binding to the polymer and depends on the refractive index. To estimate the changed quantum yield QY, the empty cavity model was utilised:[108]

$$\mathrm{QY} = \mathrm{QY}_0 \cdot \frac{\tau}{\tau_0} \cdot \frac{n^5}{n_0^5} \cdot \frac{(2n_0^2+1)^2}{(2n^2+1)^2} \tag{6.1}$$

Here, τ denotes the free-space lifetime, n the refractive index of the embedding medium and the 0 subscripts indicate the refractive index and lifetime for the known quantum yield.[170]

For the dry brush, it was assumed that the fluorophore is at the top of the polymer layer but still embedded. The refractive index of the dry brush was measured by ellipsometry and fixed at 1.46 for further analysis. The polymer layer thickness was fitted by calculating the corresponding MIET-curve and comparing the calculated lifetime at the top of the brush layer to the measured values. Considering systematic errors, like the deviations in the distribution of chain ends and the quantum yield, the obtained thicknesses are similar to the values measured by ellipsometry, given in table 6.3.

A swollen brush in strong stretching conditions has a broad distribution of chain end heights (figure 6.9). To take this distribution into account, the brush thickness was varied until the expected lifetime matched the measured lifetime. The expected lifetime was calculated by converting the chain end height distribution into a lifetime distribution and averaging this lifetime distribution weighted with the corresponding brightness. The MIET-lifetime and brightness curves were calculated for the refractive index of water and were therefore independent of

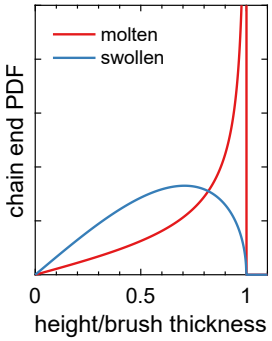

Figure 6.9: Theoretical chain end distribution in a molten/swollen polymer brush.[200]

the brush thickness. Figure 6.8(b) gives an overview of the obtained heights. It is apparent that swelling of the brush with water increases the thickness of the brush layer. Decreasing the pH to 2 further increases the thickness. This trend is expected, since the amino-groups in the polymer become protonated and thus positively charged, which leads to repulsive forces. These effects are reflected in the swelling ratios (SR in table 6.3): The swelling ratio is higher for a higher grafting density and for a low pH. This behaviour is well inline with literature; Thomas et al. [201] report swelling ratios between 2 and 4 and a similar pH dependence for much thicker brushes using atomic force microscopy.

The fitting of the lifetimes does not perform well for the low density brush. For both, the dry and swollen condition, the fits for some areas remained at the lower bound of 0 nm brush thickness. Therefore, some of the assumptions might not be valid: The chain end distribution assumes strong stretching, which is not given for weakly interacting chains (mushroom regime). Furthermore, for the dry brush, it is assumed that the fluorophore is not in contract with the cover glass surface or the air-brush interface. Both effects might occur and cause a change in quantum yield. An indication for a reduced quantum yield, is the slightly lower lifetime in dry conditions on glass compared to the denser brushes.

Dynamics of a swollen brush In a swollen polymer brush, the chains are dynamic and can diffuse. As for the tethered DNA sample, vertical diffusion of the chain ends above a gold surface is expected to cause brightness fluctuation due to the MIET effect. To analyse this diffusion, the signal from the measurements on gold was correlated. Unfortunately, some of the correlation curves (figure 6.10) contain artefacts close to scanning timescale (peak at $\sim 10^{-2}$ s), which might be caused by periodic laser power fluctuations or problems with the scanner. Therefore, only the short timescales, shown in figure 6.11(a), were analysed by fitting the correlation with a biexponential decay. As for the DNA-measurements, all correlation curves exhibit a decay close to $\sim 10^{-5}$ s which is likely caused by a triplet state. Only the correlations of the swollen brush decay substantially at the faster timescale which is reflected in the fits of the correlation (figure 6.11(b)): The fits from both swollen conditions have a clear fast component while it is close to zero in the dry condition. This indicates that the chain ends in the swollen brush undergo a vertical diffusion on a timescale of $\sim 5 \times 10^{-7}$ s, which is similar to the results obtained for tethered DNA. The charges on the chain at low pH are expected to increase the persistence length and could therefore affect the diffusion timescale. This effect is either to small too resolve or might also be compensated by the increased brush thickness.

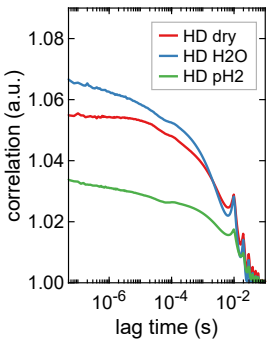

Figure 6.10: Full correlation curve of the polymer brush measurements.

So far, the correlation of the brush with high grafting density was discussed. The results from the medium density brush are similar but, due to a weaker signal, scatter more. The median of the fast decay time is with $\sim 2 \times 10^{-7}$ s slightly shorter. As the molecular weight of both brushes was similar, this indicates that the increased interactions in a

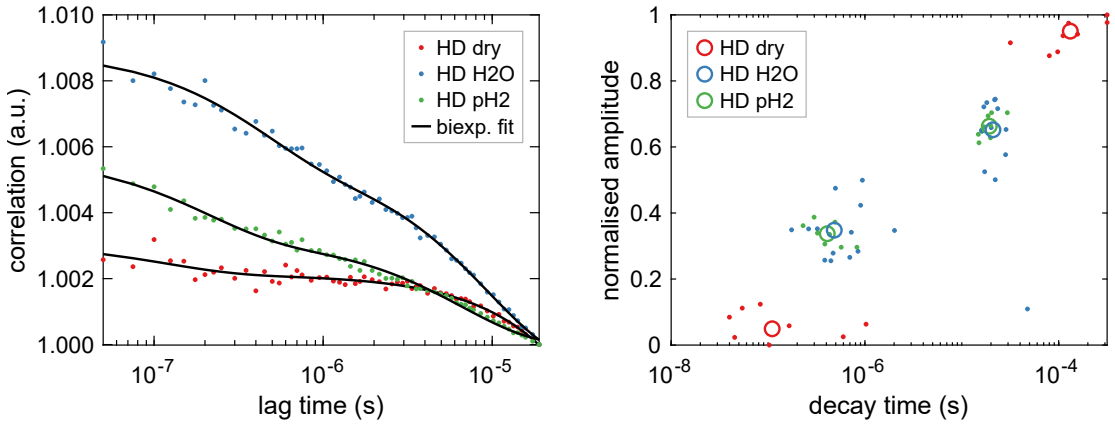

(a) correlation and biexponential fit

(b) amplitude and decay time of fit components

Figure 6.11: Correlation analysis of measurements of the high density brush on gold under three conditions, dry and swollen with dH_2O at neutral and low pH. For each condition at least eight areas were measured. (a) Summed correlation of all measured areas and biexponential fit. (b) Relative amplitude and decay time of the two exponential components for independent fits of all areas (dots). The circles mark the median of the fast and slow component for each condition.

denser brush slow down the diffusion of the chains. Because of the low density of fluorophores, the measurements from the low density brush did not contain enough signal for stable fits of the correlation. To quantify the diffusion and rigorously exclude any other origins of the fast component, modelling of the whole curve and a comparison with additional measurements of the same polymer but in bulk, not at the surface, are required.

6.1.3 *Conclusion*

Tethered single stranded DNA was investigated as a potential model system in the non-interacting regime of grafted polymer surfaces. The fabricated microfluidic devices proved to be a suitable platform to exert a controlled shear stress on the surface. Exploiting the high axial resolution of MIET, height changes of a few nanometres could be detected. The shear stress induced by the flow caused a gradual decrease of the average height of the chain ends. However, the DNA-sample did not recover from high flow rates, indicating a flow-induced change of the sample. This instability and the limited reproducibility make it unsuitable to study equilibrium phenomena such as interaction-free diffusion under shear conditions.

The MIET measurements of polymer brushes clearly show the dependence of the brush thickness on the grafting density which is in good agreement with ellipsometry measurements. Furthermore, the thickness change by swelling and the pH response of the brush were observed. Swollen brushes are a challenging sample for ellipsometry due to the small and gradually changing refractive index difference to the solvent. MIET, in combination with FCS, revealed the diffusion

dynamics of the brush. While no diffusion on the sub-microseconds timescale was observed in the dry state, the swollen brushes exhibited a correlation component at $\sim 5 \times 10^{-7}$ s which was attributed to vertical diffusion and which became faster for a less stretched brush.

Since a dense polymer brush is expected to be a more robust sample than tethered DNA, it would be of interest to study the flow effects on these synthetic polymer brushes. This project has demonstrated that MIET is a powerful tool in material science to measure the thickness of nanoscale structures and characterise their dynamics.

6.2 EFFICIENT CONVECTION-DIFFUSION MODELLING

Transport processes are ubiquitous in nature and their precise modelling is essential in many branches of engineering and natural science. A large variety of transport processes can be described as convection-diffusion problem. Important examples are the transport of molecular species in organisms, heat or charge transport in semiconductors, and material transport in microfluidics. In general, these problems can be solved numerically using finite-element methods.[202] However, these methods work in small time steps, often leading to accumulated numerical errors and infeasible computation times for dynamics on longer time scales.

For fluorescence correlation spectroscopy (FCS), solving the convection-diffusion equation is of particular importance, as FCS relies on an appropriate model. While analytic models for cases without flow (diffusion only) and with a uniform flow exist,[122, 125] the modelling in a non-uniform flow remains challenging. Diffusion in such a non-uniform flow is essential for studying shear-induced diffusion presented in the previous section. Therefore, we developed an efficient numerical approach to solve the convection-diffusion equation for laminar flow within a microfluidic channel of arbitrary cross-section.

This chapter briefly summarises the method and results presented in the following publications. The first article introduces the idea of spectral decomposition along the flow direction, while the second publication extends the approach to 3D.

Narain Karedla, Jan Christoph Thiele, Ingo Gregor, and Jörg Enderlein, 'Efficient solver for a special class of convection-diffusion problems', *Physics of Fluids* 2019, 31, 023606. 10.1063/1.5079965

Jan Christoph Thiele, Ingo Gregor, Narain Karedla, and Jörg Enderlein, 'Efficient modeling of three-dimensional convection-diffusion problems in stationary flows', *Physics of Fluids* 2020, 32, 112015. 10.1063/5.0024190

6.2.1 *Methods*

The convective-diffusive transport in a stationary laminar flow within a channel of constant cross-section is governed by the convection-diffusion equation

$$\frac{\partial c(\mathbf{r},t)}{\partial t} = D\Delta_\perp c(\mathbf{r},t) - u(x,y)\,\partial_z c(\mathbf{r},t) \tag{6.2}$$

with the local concentration $c(\mathbf{r},t)$ of the transported and diffusing quantity at position $\mathbf{r} = \{x,y,z\}$ and time t; D is the diffusion coefficient, $u(x,y)$ is the (x,y)-dependent flow in the z-direction (channel axis) and $\Delta_\perp = \partial_x^2 + \partial_y^2$ is the transverse part of the Laplace operator. The convective first order term, which makes this equation difficult to solve, can be eliminated by imposing periodic boundary conditions along z

and representing $c(\mathbf{r}, t)$ as Fourier series

$$c(\mathbf{r}, t) = \sum_{k=-K}^{K} \tilde{w}_k(\boldsymbol{\rho}, t) \exp\left(iq_k z - q_k^2 D t\right), \tag{6.3}$$

with discrete Fourier frequencies $q_k = 2\pi k/L$, where $2K+1$ is the number of summed frequency components and L the channel length. Here, the new functions $\tilde{w}_k(\boldsymbol{\rho}, t)$ is introduced that depend only on the transverse spatial coordinates $\boldsymbol{\rho} = \{x, y\}$ and time t. The Fourier decomposition separates the diffusion in a transverse and axial part. Inserting equation (6.3) into equation (6.2) yields

$$\frac{\partial \tilde{w}_k(\boldsymbol{\rho}, t)}{\partial t} = D\Delta_\perp \tilde{w}_k(\boldsymbol{\rho}, t) - iq_k u(\boldsymbol{\rho}) \tilde{w}_k(\boldsymbol{\rho}, t). \tag{6.4}$$

This equation does not contain a first order derivative and instead expresses the convection term as complex potential.

Next, the channel cross-section is discretised into N elements and the operators are converted to their corresponding discretised version, $D\Delta_\perp - iq_k u(\boldsymbol{\rho})$ becomes $D\hat{\boldsymbol{\Delta}}_\perp - iq_k \hat{\mathbf{U}}$ with the discretised Laplace operator $\hat{\boldsymbol{\Delta}}_\perp$ being a sparse and $\hat{\mathbf{U}}$ being a diagonal $N \times N$ matrix. The discretised form of $\tilde{w}_k(\boldsymbol{\rho}, t)$ is obtained by solving equation (6.4):

$$\tilde{\mathbf{w}}_k(t) = \exp\left[t\left(D\hat{\boldsymbol{\Delta}}_\perp - iq_k \hat{\mathbf{U}}\right)\right] \cdot \tilde{\mathbf{w}}_{k,0} \tag{6.5}$$

The exponent is understood as matrix exponentiation. For small N, *e. g.* when u only depends on one coordinate (2D problem), $\tilde{\mathbf{w}}_k(t)$ can be calculated for each k directly. This was shown in the first publication,[203] examples are presented in the Results section.

The initial values, $\tilde{\mathbf{w}}_{k,0}$, are determined by discretising and transforming the initial concentration distribution. For an isotropic Gaussian distribution with standard deviation σ centred at $\{x_0, y_0, z_0\}$, the initial values are

$$\tilde{\mathbf{w}}_{k,0} = \frac{1}{L} \exp\left(-iq_k z_0 - \frac{\sigma^2}{2} q_k^2 - \frac{(\mathbf{x} - x_0)^2 + (\mathbf{y} - y_0)^2}{2\sigma^2}\right) \tag{6.6}$$

where $\mathbf{x}$ and $\mathbf{y}$ denote the discretised N element coordinate vectors.

In a 3D geometry, N is, depending of the discretisation, on the order of 10^4 or higher, which makes the matrix exponentiation in equation (6.5) extremely time and memory consuming. To reduce the dimensions, the smallest M eigenvalues are determined so that

$$-D\hat{\boldsymbol{\Delta}}_\perp \cdot \psi_j = \lambda_j \psi_j, \tag{6.7}$$

with real-valued, non-negative eigenvalues λ_j and eigenvectors ψ_j. For sufficiently large M ($M \ll N$), the subspace spanned by ψ_j covers the full physics of the convection-diffusion problem well. By projecting $\hat{\mathbf{U}}$ into the eigenvalue subspace, equation (6.5) becomes

$$\tilde{\mathbf{w}}_k(t) = \hat{\boldsymbol{\Psi}} \cdot \exp\left[-t\left(\hat{\boldsymbol{\Lambda}} + iq_k \hat{\boldsymbol{\Psi}}^{\mathrm{T}} \cdot \hat{\mathbf{U}} \cdot \hat{\boldsymbol{\Psi}}\right)\right] \cdot \left(\hat{\boldsymbol{\Psi}}^{\mathrm{T}} \cdot \tilde{\mathbf{w}}_{k,0}\right), \tag{6.8}$$

where $\hat{\mathbf{\Lambda}}$ is a diagonal matrix with elements λ_j, and $\hat{\mathbf{\Psi}}$ is a $N \times M$ matrix with the eigenvectors $\boldsymbol{\psi}_j$ as columns so that

$$\hat{\mathbf{\Psi}}^{\mathrm{T}} \cdot \hat{\mathbf{\Psi}} = \hat{\mathbf{I}}_M. \tag{6.9}$$

Here, $\hat{\mathbf{I}}_M$ is the $M \times M$ identity matrix and the superscript T denotes matrix transposition. Thus, the exponentiated matrix is reduced from $N \times N$ to $M \times M$, resulting in an enormous computational advantage.

To further accelerate the calculation, the exponent in equation (6.8) is diagonalised so that

$$\hat{\mathbf{\Lambda}} + iq_k \hat{\mathbf{\Psi}}^{\mathrm{T}} \cdot \hat{\mathbf{U}} \cdot \hat{\mathbf{\Psi}} = \hat{\mathbf{S}}^{\mathrm{T}} \cdot \hat{\mathbf{D}} \cdot \hat{\mathbf{S}}, \tag{6.10}$$

where $\hat{\mathbf{S}}$ is an orthogonal matrix and $\hat{\mathbf{D}}$ is a diagonal matrix of the eigenvalues of $\hat{\mathbf{\Lambda}} + iq_k \hat{\mathbf{\Psi}}^{\mathrm{T}} \cdot \hat{\mathbf{U}} \cdot \hat{\mathbf{\Psi}}$. In the next step, the matrix exponential in equation (6.8) is computed by

$$\exp\left[-t\left(\hat{\mathbf{\Lambda}} + iq_k \hat{\mathbf{\Psi}}^{\mathrm{T}} \cdot \hat{\mathbf{U}} \cdot \hat{\mathbf{\Psi}}\right)\right] = \hat{\mathbf{S}}^{\mathrm{T}} \cdot \exp\left(-t\hat{\mathbf{D}}\right) \cdot \hat{\mathbf{S}}. \tag{6.11}$$

This approach is much faster than computing the direct matrix exponential, because the exponentiation of a diagonal matrix is the scalar exponent of its diagonal elements. The conversion in equation (6.11) comes at the cost of the diagonalisation but is, due to the time independence of $\hat{\mathbf{D}}$ and $\hat{\mathbf{S}}$, more efficient when multiple time values ($\gtrsim 5$) are calculated.

The flow $u(x, y)$ can be either set to a known flow field or, for pressure driven flow, calculated by solving the stationary Stokes equation [204]

$$\eta \Delta_\perp u(\boldsymbol{\rho}) = \partial_z p \tag{6.12}$$

with η, the viscosity of the solution, and $\partial_z p$, a constant axial pressure gradient.

When constructing the Laplace operator, different boundary conditions in the form $a\nabla_\perp c(\boldsymbol{\rho}, t) + bc(\boldsymbol{\rho}, t) = d$ with the fixed constants a, b and d may be implemented.[205] Commonly, a reflecting surface is assumed (no-flux, Neumann boundary condition) for the channel walls, so that at the wall $\nabla_\perp c(\boldsymbol{\rho}, t) = 0$. Alternatively, a perfectly absorbing surface may be defined by $c(\boldsymbol{\rho}, t) = 0$ (Dirichlet boundary condition), which is also used to implement the no-slip condition for the pressure driven flow.[206]

6.2.2 *Results*

Approaches on how to chose a sufficiently large number K for the Fourier series and the influence of number of eigenvalues N and mesh size are discussed in detail in our publications.[203, 207] Here, some of the computed results are presented to demonstrate the versatility of our method.

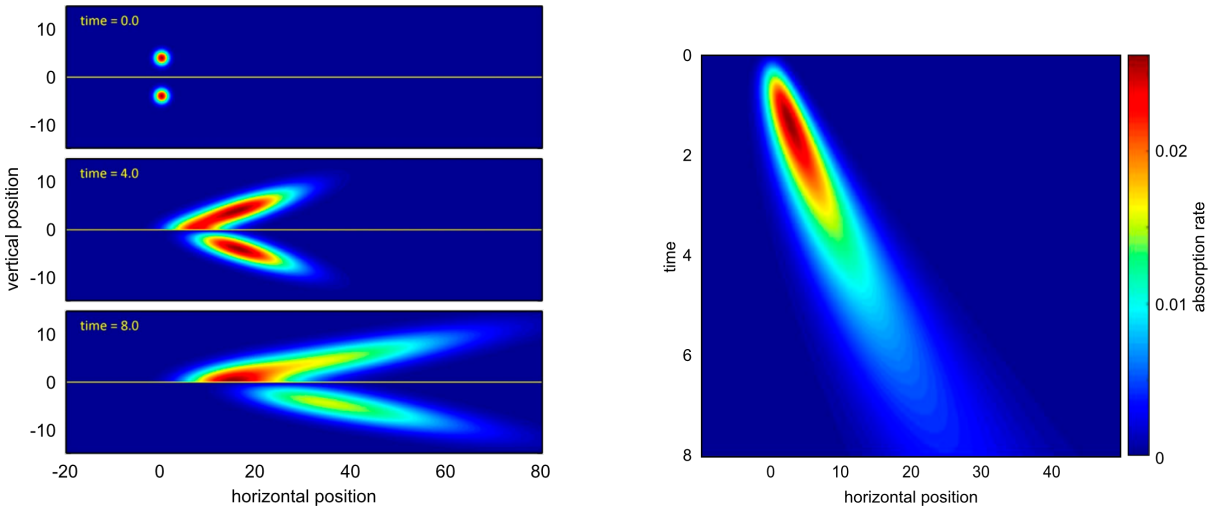

(a) temporal evolution of concentration (b) local absorption rate over time

Figure 6.12: Numerical results for the solution of the convection-diffusion equation for an initially (t = 0) Gaussian-distributed concentration. (a) The vertical axis is the y-axis and horizontal axis is the z-axis. Flow direction is from left to right, with the flow profile $u(y) = y$. The numerical value of the diffusion coefficient D set to 1. Upper half planes show the results for a reflecting surface and lower half planes for a perfectly absorbing surface. (b) Normalised absorption rate $\partial_y c(y = 0, z, t)$ as function of coordinate z and time t for the solution shown in the bottom half planes of (a). Reproduced from *Phys. Fluids* **31**, 023606 (2019) with the permission of AIP Publishing.

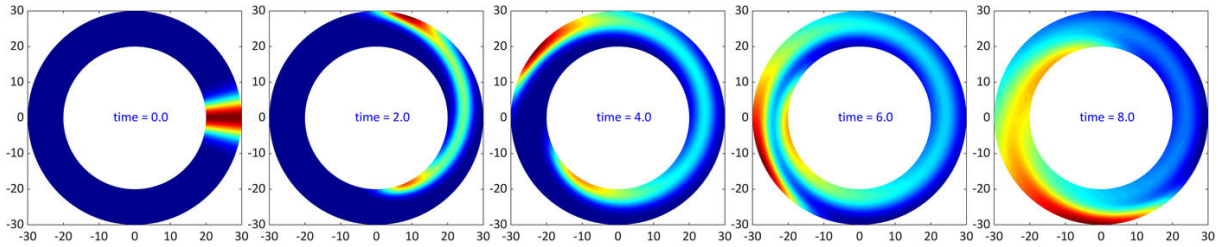

Figure 6.13: Numerical results for the solution of the convection-diffusion equation for a laminar Taylor-Couette flow between two cylinders with radius values $r_1 = 20$ and $r_2 = 30$. Both cylinders perform a full turn in 8 units of time, the inner cylinder clockwise and the outer cylinder counter-clockwise. The numerical value of the diffusion coefficient D is 2. Reproduced from *Phys. Fluids* **31**, 023606 (2019) with the permission of AIP Publishing.

Convection-diffusion in 2D

In a 2D shear flow ($u(y) = y$), the numerical solution of convective-diffusive transport next to a reflecting or absorbing surface at $y = 0$ was demonstrated. Figure 6.12 shows how the distribution from an initially Gaussian distribution evolved over time. For the absorbing surface, the absorption rate was calculated from the gradient at the surface.

Our method is not restricted to straight channels. It is applicable as long as the flow is laminar and can be transformed to a coordinate system where the flow is parallel to one of the axes and a Laplace operator can be found. In case of the Taylor-Couette flow between two counter-rotating cylinders, the flow is parallel to the angular coordinate ϕ in polar coordinates (r,ϕ). Here, the analytic flow field is known and

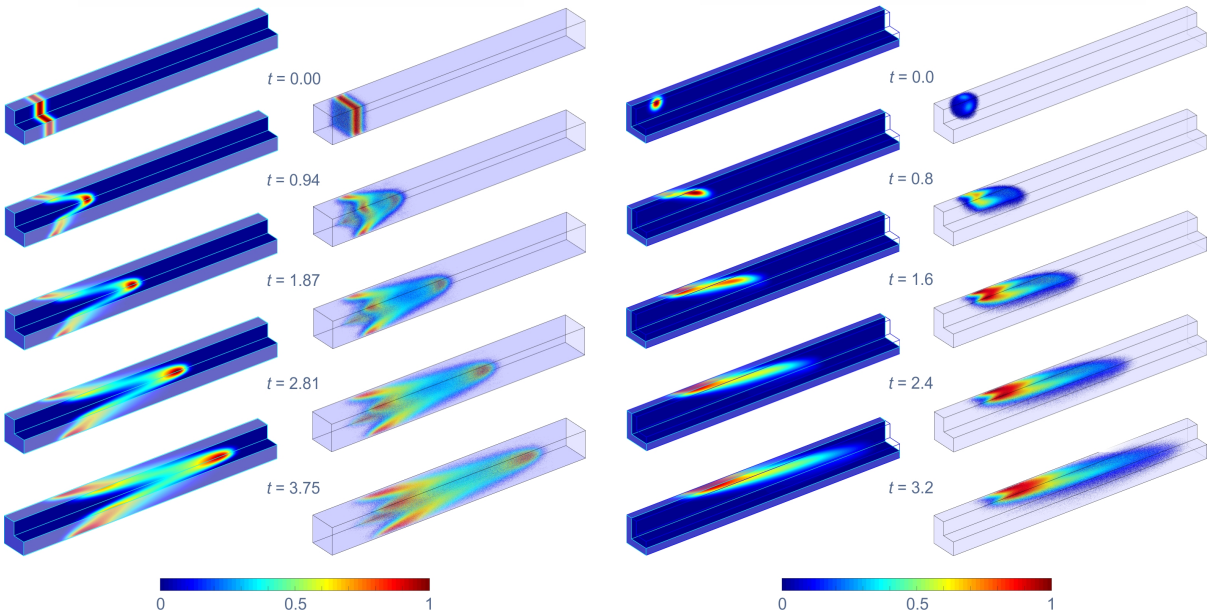

(a) temporal evolution in a square channel

(b) temporal evolution in an L-shaped channel

Figure 6.14: Numerical convection-diffusion calculation in 3D. (a) Temporal evolution of concentration distribution in a square channel, transported by the flow shown in figure 6.15(a) and dispersed by diffusion with the diffusion coefficient $D = 100\,\mu\text{m}^2/\text{s}$. Time t is given in seconds. The left panels show the concentrations on the surface of the channel and on the surface of a cut along its centre, the right panels present the concentration distribution as point clouds: 3×10^5 points are randomly distributed using the concentration distribution $c(\mathbf{r}, t)$ as probability distribution, and each point is coloured corresponding to the local concentration at its position. For each time t, colours are scaled from zero (blue) to maximum concentration (red). (b) Same as (a) but for an L-shaped channel with the flow shown in figure 6.15(a) and an isotropic Gaussian initial distribution centred at $(x_0, y_0, z_0) = (-25\,\mu\text{m}, -25\,\mu\text{m}, 100\,\mu\text{m})$ and with standard deviation $\sigma = 15\,\mu\text{m}$. Reproduced from *Phys. Fluids* **32**, 112015 (2020) with the permission of AIP Publishing.

the convection-diffusion equation becomes

$$\frac{\partial_t \left(\sqrt{r}c\right)}{\partial t} = \left[D\frac{\partial^2}{\partial r^2} + \frac{1}{r^2}\frac{\partial^2}{\partial \phi^2} + \frac{1}{4r^2} - \frac{u(r)}{r}\frac{\partial}{\partial \phi}\right]\left(\sqrt{r}c\right). \tag{6.13}$$

To solve this equation, it is treated as described in the methods section. $(1 + \cos\phi)^{100}$ was chosen as initial concentration distribution since it can be conveniently expressed as Fourier series with respect to ϕ. The numerical results for different integration times are shown in figure 6.13.

Convection-diffusion in 3D

To numerically solve the convection-diffusion equation in a 3D geometry, an eigenvalue decomposition was used to reduce the size of the problem. This approach is similar to the *strange eigenmodes* of the Laplace operator used by Liu and Haller.[208] The reduced problem can be solved in a few seconds per time point. In figure 6.14, the temporal evolution of a 1D Gaussian concentration distribution in a square and of a 3D Gaussian distribution in an L-shaped channel are shown.

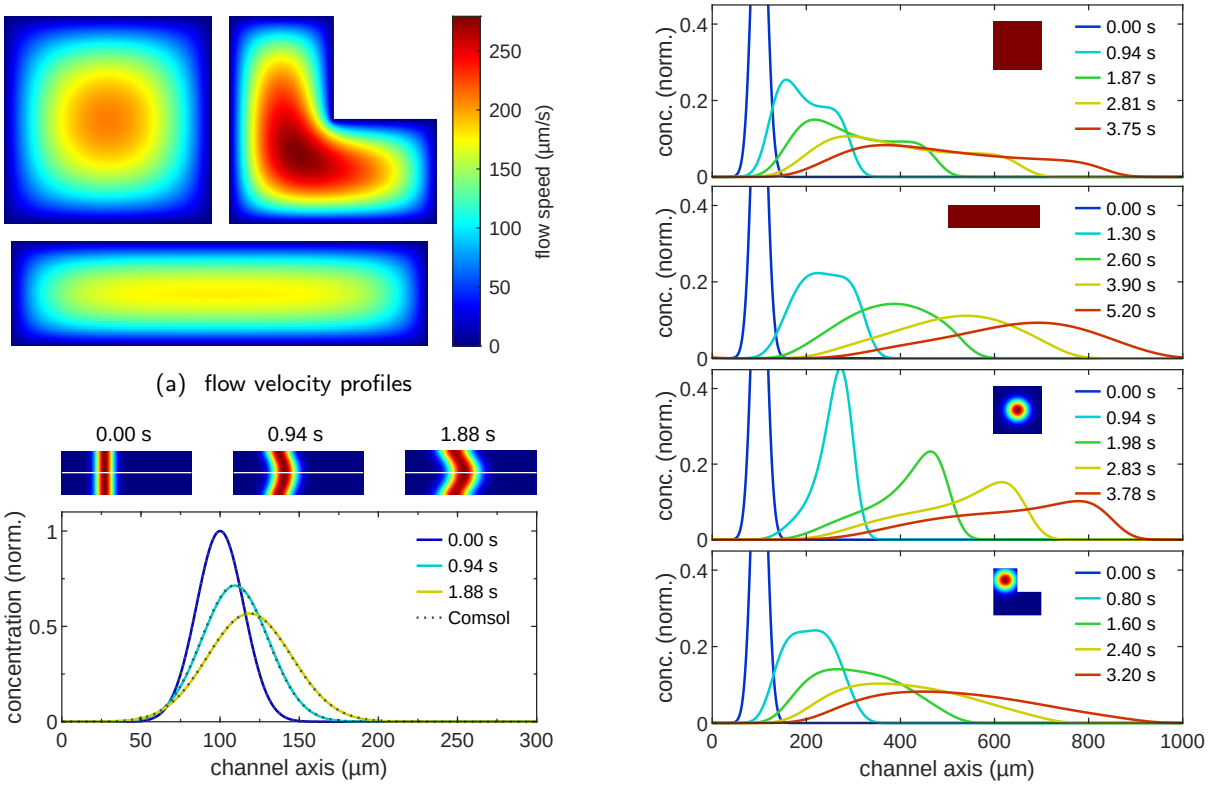

(a) flow velocity profiles

(b) comparison with COMSOL

(c) temporal evolution of the dispersion

Figure 6.15: (a) Flow velocity profiles calculated by solving equation (6.12) for different cross-sections. In all three calculations, the pressure gradient $\partial_z p$ was adjusted to yield a volume flow rate of $10^6\,\mu m^3/s$. The cross-sections are a $100 \times 100\,\mu m$ square, an L-shape, constructed by removing one quater of the square, and a $50 \times 200\,\mu m$ rectangle. (b) Comparison with the commercial finite-element partial differential equation solver COMSOL. Calculations were performed for a square channel using the diffusion coefficient $D = 100\,\mu m^2/s$ and a volume flow rate of $10^5\,\mu m^3/s$. The top panel shows cross-sections through the middle plane of the channel, where the results above the white mid line are obtained with COMSOL, and below with our method. The bottom panel compares the total concentration integrated over the channel cross-section. The dotted lines show the COMSOL results, and solid lines those of our method. The computation time with COMSOL was by more than three orders of magnitude longer than that for our method. (c) Dispersion of concentration for the flow as shown in (a). The concentration, averaged over the channel cross-section, is plotted as a function of position along the channel and time. The channel cross-section and initial concentration distribution are indicated in the insets and are from top to bottom: square channel with uniform lateral concentration (1D Gaussian distribution as shown in figure 6.14(a)), rectangular channel with uniform lateral concentration, square channel with isotropic 3D Gaussian distributed concentration, and L-shaped channel with isotropic 3D Gaussian distributed concentration (figure 6.14(b)).

Since the contribution of the omitted eigenvalues decreases over time and each result is calculated directly from the initial distribution, the results are increasingly exact for longer times. This is in contrast to sequential finite-element methods which calculate the solution in time steps and thus might accumulate numerical errors. We have compared our method with the commercial finite element modelling software COMSOL (Comsol Multiphysics GmbH, Göttingen, Germany). Besides a multiple order of magnitudes slower performance, the results for a square channel at short time scales and a low flow rate are indistinguishable from our method (figure 6.15(b)).

In time resolved microfluidc approaches, *e. g.* chromatographic or mixing induced experiments,[209] Taylor-Aris dispersion has to be considered to quantitatively describe the temporal evolution of the concentration distribution. How the dispersion evolves for different initial concentrations and channel geometries is shown in figure 6.15(c).

6.2.3 *Conclusion & outlook*

We presented an efficient numerical approach to solve the convection-diffusion equation for stationary, laminar flow within a channel of arbitrary but constant cross-section. Our method is multiple orders of magnitude faster than conventional finite-element methods while allowing for high spatial and arbitrary temporal resolution. To facilitate adaption to custom geometries, we have provided commented MATLAB routines with the publication.[207]

In the future, the method could be adapted to help analysing fluorescence correlation spectroscopy in a non-uniform flow, *e. g.* a shear flow close to a surface. Calculating the correlation curve in such conditions is challenging, since the temporal evolution of the distribution of the detected species needs to be determined with high resolution over a broad timescale. For non-uniform flow, this cannot be achieved analytically in general. To give a first example, the correlation curve for a diffusing molecule in a flow was calculated as follows: As the molecule detection probability function (MDF) a 3D anisotropic Gaussian was as used as simple approximation of a confocal focus. At time point $t = 0$, a molecule was detected, the probability distribution of the molecule position corresponds to the MDF, which was used as initial 'concentration'. The probability distribution at a time point $t > 0$ was computed and the detection probability calculated as overlap integral between the probability distribution of the molecule and the MDF. This was repeated for several time points t on a logarithmic time-axis.

The time-dependent detection probability corresponds to the correlation determined by FCS. In figure 6.16, the simulated correlation for two different focus positions is compared with a FCS model for uniform flow.[210] The flow is approximately uniform in the centre of the channel and the simulation therefore matches well to the analytic FCS model. At the surface however, the model deviates form the simulation due to the non-uniform flow.

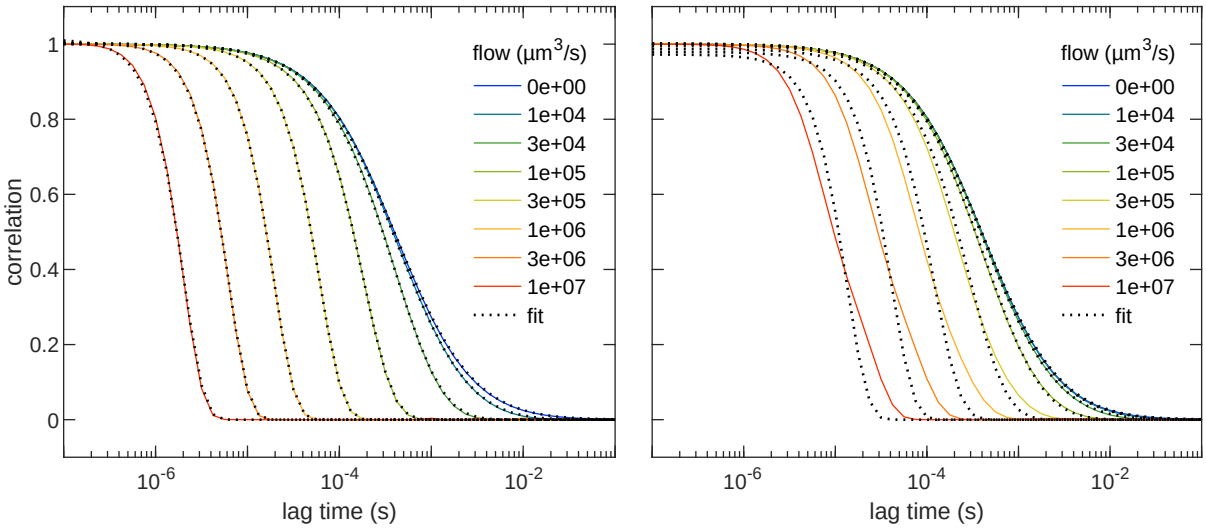

(a) focus in centre of channel

(b) focus at surface of channel

Figure 6.16: Simulated correlation curves in a $10 \times 10\,\mu m$ channel for different flow rates. In (a), the $\sigma = \{0.8, 0.2, 0.2\}$ µm Gaussian focus was placed in the centre of the channel, and in (b) at a yz-channel wall. The channel was discretised into 10 nm elements. The fits were performed with a model for uniform flow.[210] For no flow, the flow component was omitted, for all fits with flow, the diffusion coefficient was fixed to the value determined for no flow.

With some adaptions, *e. g.* extension to two-focus FCS,[211] different boundary conditions and adaptive discretisation for increased performance, this approach to simulate the correlation curve might be used to better quantify the interaction of flow with the surface, for example slip on super-hydrophobic surfaces [212] or drag exerted by polymer brushes.[213]

6.3 LIFETIME-BASED DNA MAPPING

The most specific method to identify microorganisms is to sequence their DNA and compare it to a database. However, often the sequence itself is not of interest. Optical DNA mapping instead enzymatically labels specific short sequences and analyses the thereby obtained barcode-like patterns in images of immobilised or confined DNA.[214] This method cannot extract an unknown sequence but the long-range pattern is often sufficient for matching with a database of candidates and has the considerable advantage of processing all DNA present in the sample in parallel.

Affinity based barcoding methods avoid the enzymatic labelling by exploiting temperature induced partial denaturation [217] or competitive binding.[218] Here, we propose a similar approach which does not need a precise temperature or concentration control by choosing a fluorophore with a lifetime that is sensitive to the local GC-content and the wide-field TCSPC camera introduced in chapter 4. This project is still work in progress. The sample preparation and measurements were performed by Arindam Ghosh and Oleksii Nevskyi. I developed the data analysis, briefly presented in the following.

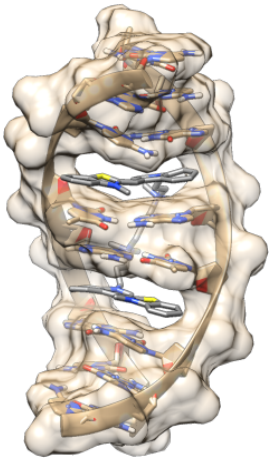

Figure 6.17: DNA intercalating fluorophore TOTO. PDB ID: 108D.[215, 216]

For demonstration purposes, λ-phage DNA was incubated it with the fluorophore YOYO-1 and immobilised on a silane coated surface. YOYO-1 is, like the structurally similar TOTO shown in figure 6.17, a bis-intercalating dye, which is in close contact to four adjacent base pairs. The binding strength and lifetime depend on the local fraction of GC base pairs.[219, 220] Figure 6.18(a) shows the lifetime in presence of different GC-fractions, measured with a short synthetic reference DNA. To generate lifetime profiles, a DNA strand was traced in the FLIM image (figure 6.18(b)), the trace was divided into segments and the TCSPC histograms were extracted for each segment. Since the TCSPC histograms were not monoexponential, the decay was fitted with six fixed exponential components which was more stable at low photon numbers than a biexponential fit with unconstrained lifetimes. To avoid

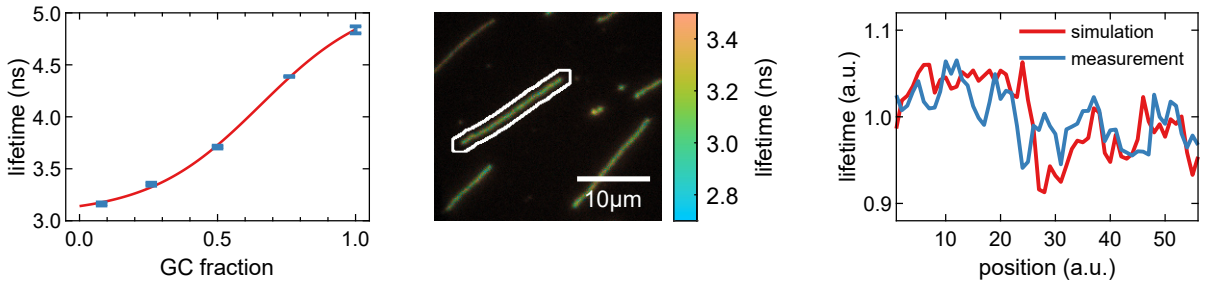

(a) GC sensing of YOYO-1 (b) immobilised λ-DNA (c) measured and simulated profile

Figure 6.18: (a) GC-dependence of the lifetime of YOYO-1 measured with short synthetic dsDNA. The red line represents a logistic fit. (b) Wide-field FLIM image of immobilised λ-DNA. (c) Lifetime profile of the highlighted strand and a simulated lifetime profile.

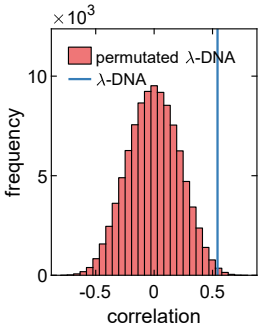

Figure 6.19: Correlation between measured profile and simulated λ-DNA profile (blue) and 10^5 simulated random profiles.

bias, the amplitudes were determined using PIRLS (Poisson iteratively reweighted least squares).[195] The lifetime was determined as amplitude weighted average of the six component lifetimes.

In figure 6.18(c), the measured lifetime profile is shown together with a profile simulated using the sequence of λ-DNA and the GC-lifetime dependence from (a). To verify the match, the correlation between both curves was calculated and compared to the correlation between the measured profile and 10^5 simulated random profiles. This comparison is shown in the histogram in figure 6.19. The correlation to the λ-DNA sequence was with 0.54 higher than to 99.6 % of the random profiles. To generate realistic random profiles and avoid an unnatural homogeneous distribution of the GC content, the λ-DNA sequence was divided into 15 segments of equal length which were permuted randomly.

The next steps are to include multiple DNA-sequences and to extended the analysis to allow for inhomogeneities in the stretching which probably will improve the matching. The presented results demonstrate, that lifetime-based DNA-mapping is a promising approach to identify a DNA sequence in a large database of known sequences. The direct labelling with a specific DNA-intercalating dye makes it potentially faster than enzymatic labelling strategies and simplifies the sample preparation.

7 CONCLUSION

Super-resolution microscopy has revolutionised fluorescence microscopy, especially in microbiology. It extends the accessible size range beyond the diffraction limit and makes nanoscale structures such as protein complexes optically observable. The unique advantage of fluorescence based techniques is their outstanding sensitivity and contrast. This combination, achieved by specific labelling, enables measurements inside cells and even living organisms. A fluorescence signal can convey more information than solely the position. Specifically, the fluorescence lifetime is characteristic for the probe and in some cases even sensitive to the local environment.

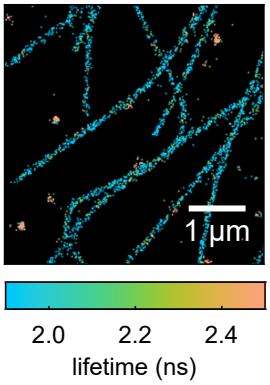

Figure 7.1: Super-resolved FLIM image of clathrin (Atto 655) and tubulin (Alexa 647) in a COS-7 cell.

In chapter 3, an approach to combine super-resolution and FLIM was introduced. It relies on single molecule localisation with confocal microscopy. By utilising a fast laser scanner, pulsed excitation, and single photon detection, the lifetime of each individual localisation was determined in dSTORM and DNA-PAINT measurements. We demonstrated that different fluorophores can be distinguished based on their lifetime. This allows classification of each localisation and hence multiplexing free of any chromatic aberration. We show that the classification is robust and can be applied to broad and overlapping lifetime distributions by employing Bayesian pattern matching of the full TCSPC-histogram.

Confocal SMLM offers more advantages than solely lifetime information: the confocal sectioning suppresses out-of-focus background signal and enables SMLM measurement in densely labelled 3D samples. The detection by single-photon sensitive detectors yields extremely low noise (no excess or read-out noise), and it is straight-forward to include spectral splitting which does not lead to chromatic aberration.

Single molecule sensitive FLIM with high lifetime resolution has so far only been achieved with confocal microscopy. In chapter 4, we demonstrate that with wide-field FLIM, employing a novel TCSPC camera, single molecules can be detected. By utilising deep-red fluorophores, we choose the spectral region with the lowest detection efficiency ($<5\,\%$). Nevertheless, three different deep-red fluorophores were distinguished based on their lifetime. In combination with MIET, individual fluorophores were localised with $\sim$10 nm axial precision. Wide-field FLIM offers a parallel detection over a large field of view, which makes it potentially faster, and has the advantage that TIR illumination can be easily implemented. TIR illumination reduces the background signal from solution in DNA-PAINT and is especially beneficial for MIET, since it restricts the excitation of the sample to the region influenced by the lifetime quenching.

The presented techniques can be easily implemented with commercial instruments, it is therefore important to make also the data analysis accessible. For this reason, I have extended the software TrackNTrace to cover the complete analysis, starting from the raw data to the lifetime fitting. The data visualiser provides a drift correction, filtering

of localisations, and reconstruction of super-resolved FLIM images. As demonstrated in chapter 5, the software supports data from a CLSM as well as the TCSPC camera.

We employed super-resolved FLIM for multiplexing, however it is also promising for other typical applications of FLIM. As mentioned earlier, FLIM can measure properties of the local environment of a fluorophore, *e. g.* order, viscosity, or tension of membranes. It is well known that bio-membranes can be organised on the nanoscale, therefore it would be exciting to map their properties with super-resolved FLIM. The additional lifetime information for each localisation does also pave the way for lifetime-based super-resolved FRET imaging, which can disentangle fast dynamics from stationary intermediate states.

By combining lifetime resolved SMLM with MIET, the lifetime information can be converted into an axial position, thus achieving 3D localisation. A first example, demonstrating its feasibility, was presented in section 3.5. The high axial precision could enable 3D super-resolved imaging with high and isotropic resolution, which is attractive for potential applications in structural biology.

BIBLIOGRAPHY

[1] R Hooke. *Micrographia, or, Some Physiological Descriptions of Minute Bodies Made by Magnifying Glasses: With Observations and Inquiries Thereupon*. Early English Books. London: Printed by Jo. Martyn and Ja. Allestry, 1665. 10 pp.

[2] E Abbe. 'Beiträge zur Theorie des Mikroskops und der mikroskopischen Wahrnehmung'. In: *Archiv für Mikroskopische Anatomie* 9.1 (1873), 413–468. DOI: 10.1007/BF02956173.

[3] A Köhler and M Rohr. 'Photomicrography with Ultra-Violet Light'. In: *J. Roy. Microsc. Soc.* 4.25 (1905), 513.

[4] AH Coons, HJ Creech, RN Jones and E Berliner. 'The Demonstration of Pneumococcal Antigen in Tissues by the Use of Fluorescent Antibody'. In: *The Journal of Immunology* 45.3 (1942), 159–170. ISSN: 0022-1767.

[5] F Roberts and J Young. 'The Flying-Spot Microscope'. In: *Proceedings of the IEE - Part IIIA: Television* 99.20 (1952), 747–757. DOI: 10.1049/pi-3a.1952.0090.

[6] M Minsky. 'Microscopy Apparatus'. U.S. pat. 3013467A. Minsky Marvin. 1961.

[7] M Minsky. 'Memoir on Inventing the Confocal Scanning Microscope'. In: *Scanning* 10.4 (1988), 128–138. DOI: 10.1002/sca.4950100403.

[8] P Davidovits and MD Egger. 'Scanning Laser Microscope'. In: *Nature* 223.5208 (1969), 831–831. DOI: 10.1038/223831a0.

[9] GJ Brakenhoff, HTM van der Voort, EA van Spronsen, WAM Linnemans and N Nanninga. 'Three-Dimensional Chromatin Distribution in Neuroblastoma Nuclei Shown by Confocal Scanning Laser Microscopy'. In: *Nature* 317.6039 (1985), 748–749. DOI: 10.1038/317748a0.

[10] JG White, WB Amos and M Fordham. 'An Evaluation of Confocal versus Conventional Imaging of Biological Structures by Fluorescence Light Microscopy.' In: *Journal of Cell Biology* 105.1 (1987), 41–48. DOI: 10.1083/jcb.105.1.41.

[11] D Magde, E Elson and WW Webb. 'Thermodynamic Fluctuations in a Reacting System—Measurement by Fluorescence Correlation Spectroscopy'. In: *Physical Review Letters* 29.11 (1972), 705–708. DOI: 10.1103/PhysRevLett.29.705.

[12] J Widengren, V Kudryavtsev, M Antonik, S Berger, M Gerken and CAM Seidel. 'Single-Molecule Detection and Identification of Multiple Species by Multiparameter Fluorescence Detection'. In: *Analytical Chemistry* 78.6 (2006), 2039–2050. DOI: 10.1021/ac0522759.

[13] B Rotman. 'Measurement of Activity of Single Molecules of β-D-Galactosidase'. In: *Proceedings of the National Academy of Sciences* 47.12 (1961), 1981–1991. DOI: 10.1073/pnas.47.12.1981.

[14] T Hirschfeld. 'Optical Microscopic Observation of Single Small Molecules'. In: *Applied Optics* 15.12 (1976), 2965–2966. DOI: 10.1364/AO.15.002965.

[15] WE Moerner and L Kador. 'Optical Detection and Spectroscopy of Single Molecules in a Solid'. In: *Physical Review Letters* 62.21 (1989), 2535–2538. DOI: 10.1103/PhysRevLett.62.2535.

[16] M Orrit and J Bernard. 'Single Pentacene Molecules Detected by Fluorescence Excitation in a P-Terphenyl Crystal'. In: *Physical Review Letters* 65.21 (1990), 2716–2719. DOI: 10.1103/PhysRevLett.65.2716.

[17] E Brooks Shera, NK Seitzinger, LM Davis, RA Keller and SA Soper. 'Detection of Single Fluorescent Molecules'. In: *Chemical Physics Letters* 174.6 (1990), 553–557. DOI: 10.1016/0009-2614(90)85485-U.

[18] PM Goodwin, ME Johnson, JC Martin, WP Ambrose, BL Marrone, JH Jett and RA Keller. 'Rapid Sizing of Individual Fluorescently Stained DNA Fragments by Flow Cytometry'. In: *Nucleic Acids Research* 21.4 (1993), 803–806. DOI: 10.1093/nar/21.4.803.

[19] R Rigler and U Mets. 'Diffusion of Single Molecules through a Gaussian Laser Beam'. In: *Laser Spectroscopy of Biomolecules*. Laser Spectroscopy of Biomolecules. Vol. 1921. International Society for Optics and Photonics, 1993, 239–248. DOI: 10.1117/12.146154.

[20] M Prummer, CG Hübner, B Sick, B Hecht, A Renn and UP Wild. 'Single-Molecule Identification by Spectrally and Time-Resolved Fluorescence Detection'. In: *Analytical Chemistry* 72.3 (2000), 443–447. DOI: 10.1021/ac991116k.

[21] J Enderlein and M Sauer. 'Optimal Algorithm for Single-Molecule Identification with Time-Correlated Single-Photon Counting'. In: *The Journal of Physical Chemistry A* 105.1 (2001), 48–53. DOI: 10.1021/jp002358n.

[22] JJ Macklin, JK Trautman, TD Harris and LE Brus. 'Imaging and Time-Resolved Spectroscopy of Single Molecules at an Interface'. In: *Science* 272.5259 (1996), 255–258. DOI: 10.1126/science.272.5259.255.

[23] T Funatsu, Y Harada, M Tokunaga, K Saito and T Yanagida. 'Imaging of Single Fluorescent Molecules and Individual ATP Turnovers by Single Myosin Molecules in Aqueous Solution'. In: *Nature* 374.6522 (1995), 555–559. DOI: 10.1038/374555a0.

[24] T Schmidt, GJ Schütz, W Baumgartner, HJ Gruber and H Schindler. 'Imaging of Single Molecule Diffusion'. In: *Proceedings of the National Academy of Sciences* 93.7 (1996), 2926–2929. DOI: 10.1073/pnas.93.7.2926.

[25] Y Sako, S Minoghchi and T Yanagida. 'Single-Molecule Imaging of EGFR Signalling on the Surface of Living Cells'. In: *Nature Cell Biology* 2.3 (2000), 168–172. DOI: 10.1038/35004044.

[26] E Betzig and RJ Chichester. 'Single Molecules Observed by Near-Field Scanning Optical Microscopy'. In: *Science* 262.5138 (1993), 1422–1425. DOI: 10.1126/science.262.5138.1422.

[27] TA Klar and SW Hell. 'Subdiffraction Resolution in Far-Field Fluorescence Microscopy'. In: *Optics Letters* 24.14 (1999), 954–956. DOI: 10.1364/OL.24.000954.

[28] MGL Gustafsson. 'Surpassing the Lateral Resolution Limit by a Factor of Two Using Structured Illumination Microscopy'. In: *Journal of Microscopy* 198.2 (2000), 82–87. DOI: 10.1046/j.1365-2818.2000.00710.x.

[29] E Betzig, GH Patterson, R Sougrat et al. 'Imaging Intracellular Fluorescent Proteins at Nanometer Resolution'. In: *Science* 313.5793 (2006), 1642–1645. DOI: 10.1126/science.1127344.

[30] ST Hess, TPK Girirajan and MD Mason. 'Ultra-High Resolution Imaging by Fluorescence Photoactivation Localization Microscopy'. In: *Biophysical Journal* 91.11 (2006), 4258–4272. DOI: 10.1529/biophysj.106.091116.

[31] MJ Rust, M Bates and X Zhuang. 'Sub-Diffraction-Limit Imaging by Stochastic Optical Reconstruction Microscopy (STORM)'. In: *Nature Methods* 3.10 (2006), 793–796. DOI: 10.1038/nmeth929.

[32] E Gaviola. 'Ein Fluorometer. Apparat zur Messung von Fluoreszenzabklingungszeiten'. In: *Zeitschrift für Physik* 42.11 (1927), 853–861. DOI: 10.1007/BF01776683.

[33] JR Lakowicz and KW Berndt. 'Lifetime-selective Fluorescence Imaging Using an RF Phase-sensitive Camera'. In: *Review of Scientific Instruments* 62.7 (1991), 1727–1734. DOI: 10.1063/1.1142413.

[34] TWJ Gadella, RM Clegg and TM Jovin. 'Fluorescence Lifetime Imaging Microscopy: Pixel-by-Pixel Analysis of Phase-Modulation Data'. In: *Bioimaging* 2.3 (1994), 139–159. DOI: 10.1002/1361-6374(199409)2:3<139::aid-bio4>3.0.co;2-t.

[35] JR Lakowicz, H Szmacinski, K Nowaczyk and ML Johnson. 'Fluorescence Lifetime Imaging of Free and Protein-Bound NADH'. In: *Proceedings of the National Academy of Sciences* 89.4 (1992), 1271–1275. DOI: 10.1073/pnas.89.4.1271.

[36] I Georgakoudi and KP Quinn. 'Optical Imaging Using Endogenous Contrast to Assess Metabolic State'. In: *Annual Review of Biomedical Engineering* 14.1 (2012), 351–367. DOI: 10.1146/annurev-bioeng-071811-150108.

[37] AS Klymchenko. 'Solvatochromic and Fluorogenic Dyes as Environment-Sensitive Probes: Design and Biological Applications'. In: *Accounts of Chemical Research* 50.2 (2017), 366–375. DOI: 10.1021/acs.accounts.6b00517.

[38] PIH Bastiaens and A Squire. 'Fluorescence Lifetime Imaging Microscopy: Spatial Resolution of Biochemical Processes in the Cell'. In: *Trends in Cell Biology* 9.2 (1999), 48–52. DOI: 10.1016/S0962-8924(98)01410-X.

[39] JC Thiele, DA Helmerich, N Oleksiievets, R Tsukanov, E Butkevich, M Sauer, O Nevskyi and J Enderlein. 'Confocal Fluorescence-Lifetime Single-Molecule Localization Microscopy'. In: *ACS Nano* 14.10 (2020), 14190–14200. DOI: 10.1021/acsnano.0c07322.

[40] LA Masullo, F Steiner, J Zähringer et al. 'Pulsed Interleaved MINFLUX'. In: *Nano Letters* (2020). DOI: 10.1021/acs.nanolett.0c04600.

[41] 'Introduction to Fluorescence'. In: *Principles of Fluorescence Spectroscopy*. Ed. by JR Lakowicz. Boston, MA: Springer US, 2006, 1–26. ISBN: 978-0-387-46312-4. DOI: 10.1007/978-0-387-46312-4_1.

[42] B Valeur. 'Molecular Fluorescence Principles and Applications'. In: *Molecular Fluorescence* (2001), 399. DOI: 10.1002/3527600248.

[43] PW Hawkes and JCH Spence, eds. *Science of Microscopy*. New York: Springer, 2007. 2 pp. ISBN: 978-0-387-25296-4.

[44] A Diaspro, ed. *Optical Fluorescence Microscopy*. Berlin, Heidelberg: Springer Berlin Heidelberg, 2011. ISBN: 978-3-642-15174-3. DOI: 10.1007/978-3-642-15175-0.

[45] J Vangindertael, R Camacho, W Sempels, H Mizuno, P Dedecker and KPF Janssen. 'An Introduction to Optical Super-Resolution Microscopy for the Adventurous Biologist'. In: *Methods and Applications in Fluorescence* 6.2 (2018), 022003. DOI: 10.1088/2050-6120/aaae0c.

[46] ThermoFisher. *Cy3 dye*. URL: https://www.thermofisher.com/de/de/home/life-science/cell-analysis/fluorophores/cy3-dye.html (visited on 28/10/2020).

[47] GB Airy. 'On the Diffraction of an Object-Glass with Circular Aperture'. In: *Transactions of the Cambridge Philosophical Society* 5 (1835), 283–291.

[48] M Born and E Wolf. *Principles of Optics*. Oxford: Pergamon Press, 1970. ISBN: 978-0-08-013987-6.

[49] B Zhang, J Zerubia and JC Olivo-Marin. 'Gaussian Approximations of Fluorescence Microscope Point-Spread Function Models'. In: *Applied Optics* 46.10 (2007), 1819–1829. DOI: 10.1364/AO.46.001819.

[50] SW Hell and J Wichmann. 'Breaking the Diffraction Resolution Limit by Stimulated Emission: Stimulated-Emission-Depletion Fluorescence Microscopy'. In: *Optics Letters* 19.11 (1994), 780–782. DOI: 10.1364/OL.19.000780.

[51] M Hofmann, C Eggeling, S Jakobs and SW Hell. 'Breaking the Diffraction Barrier in Fluorescence Microscopy at Low Light Intensities by Using Reversibly Photoswitchable Proteins'. In: *Proceedings of the National Academy of Sciences* 102.49 (2005), 17565–17569. DOI: 10.1073/pnas.0506010102.

[52] M Bossi, J Fölling, M Dyba, V Westphal and SW Hell. 'Breaking the Diffraction Resolution Barrier in Far-Field Microscopy by Molecular Optical Bistability'. In: *New Journal of Physics* 8.11 (2006), 275–275. DOI: 10.1088/1367-2630/8/11/275.

[53] KA Lidke, B Rieger, TM Jovin and R Heintzmann. 'Superresolution by Localization of Quantum Dots Using Blinking Statistics'. In: *Optics Express* 13.18 (2005), 7052. DOI: 10.1364/OPEX.13.007052.

[54] GT Dempsey, M Bates, WE Kowtoniuk, DR Liu, RY Tsien and X Zhuang. 'Photoswitching Mechanism of Cyanine Dyes'. In: *Journal of the American Chemical Society* 131.51 (2009), 18192–18193. DOI: 10.1021/ja904588g.

[55] S van de Linde, I Krstić, T Prisner, S Doose, M Heilemann and M Sauer. 'Photoinduced Formation of Reversible Dye Radicals and Their Impact on Super-Resolution Imaging'. In: *Photochemical & Photobiological Sciences* 10.4 (2011), 499–506. DOI: 10.1039/C0PP00317D.

[56] M Heilemann, S van de Linde, M Schüttpelz, R Kasper, B Seefeldt, A Mukherjee, P Tinnefeld and M Sauer. 'Subdiffraction-Resolution Fluorescence Imaging with Conventional Fluorescent Probes'. In: *Angewandte Chemie International Edition* 47.33 (2008), 6172–6176. DOI: 10.1002/anie.200802376.

[57] JC Vaughan, S Jia and X Zhuang. 'Ultrabright Photoactivatable Fluorophores Created by Reductive Caging'. In: *Nature Methods* 9.12 (2012), 1181–1184. DOI: 10.1038/nmeth.2214.

[58] K Nienhaus and GU Nienhaus. 'Fluorescent Proteins for Live-Cell Imaging with Super-Resolution'. In: *Chemical Society Reviews* 43.4 (2014), 1088–1106. DOI: 10.1039/C3CS60171D.

[59] Sn Uno, M Kamiya, T Yoshihara et al. 'A Spontaneously Blinking Fluorophore Based on Intramolecular Spirocyclization for Live-Cell Super-Resolution Imaging'. In: *Nature Chemistry* 6.8 (2014), 681–689. DOI: 10.1038/nchem.2002.

[60] PJ Macdonald, S Gayda, RA Haack, Q Ruan, RJ Himmelsbach and SY Tetin. 'Rhodamine-Derived Fluorescent Dye with Inherent Blinking Behavior for Super-Resolution Imaging'. In: *Analytical Chemistry* 90.15 (2018), 9165–9173. DOI: 10.1021/acs.analchem.8b01645.

[61] A Sharonov and RM Hochstrasser. 'Wide-Field Subdiffraction Imaging by Accumulated Binding of Diffusing Probes'. In: *Proceedings of the National Academy of Sciences* 103.50 (2006), 18911–18916. DOI: 10.1073/pnas.0609643104.

[62] G Giannone, E Hosy, F Levet et al. 'Dynamic Superresolution Imaging of Endogenous Proteins on Living Cells at Ultra-High Density'. In: *Biophysical Journal* 99.4 (2010), 1303–1310. DOI: 10.1016/j.bpj.2010.06.005.

[63] T Kiuchi, M Higuchi, A Takamura, M Maruoka and N Watanabe. 'Multitarget Super-Resolution Microscopy with High-Density Labeling by Exchangeable Probes'. In: *Nature Methods* 12.8 (8 2015), 743–746. DOI: 10.1038/nmeth.3466.

[64] C Oi, Z Gidden, L Holyoake, O Kantelberg, S Mochrie, MH Horrocks and L Regan. 'LIVE-PAINT Allows Super-Resolution Microscopy inside Living Cells Using Reversible Peptide-Protein Interactions'. In: *Communications Biology* 3.1 (2020), 1–10. DOI: 10.1038/s42003-020-01188-6.

[65] R Jungmann, C Steinhauer, M Scheible, A Kuzyk, P Tinnefeld and FC Simmel. 'Single-Molecule Kinetics and Super-Resolution Microscopy by Fluorescence Imaging of Transient Binding on DNA Origami'. In: *Nano Letters* 10.11 (2010), 4756–4761. DOI: 10.1021/nl103427w.

[66] KI Mortensen, LS Churchman, JA Spudich and H Flyvbjerg. 'Optimized Localization Analysis for Single-Molecule Tracking and Super-Resolution Microscopy'. In: *Nature Methods* 7.5 (2010), 377–381. DOI: 10.1038/nmeth.1447.

[67] B Rieger and S Stallinga. 'The Lateral and Axial Localization Uncertainty in Super-Resolution Light Microscopy'. In: *ChemPhysChem* 15.4 (2014), 664–670. DOI: 10.1002/cphc.201300711.

[68] CE Shannon. 'Communication in the Presence of Noise'. In: *Proceedings of the IRE* 37.1 (1949), 10–21. DOI: 10.1109/JRPROC.1949.232969.

[69] M Mikhaylova, BMC Cloin, K Finan et al. 'Resolving Bundled Microtubules Using Anti-Tubulin Nanobodies'. In: *Nature Communications* 6.1 (2015), 7933. DOI: 10.1038/ncomms8933.

[70] T Dertinger, R Colyer, G Iyer, S Weiss and J Enderlein. 'Fast, Background-Free, 3D Super-Resolution Optical Fluctuation Imaging (SOFI)'. In: *Proceedings of the National Academy of Sciences* 106.52 (2009), 22287–22292. DOI: 10.1073/pnas.0907866106.

[71] N Gustafsson, S Culley, G Ashdown, DM Owen, PM Pereira and R Henriques. 'Fast Live-Cell Conventional Fluorophore Nanoscopy with ImageJ through Super-Resolution Radial Fluctuations'. In: *Nature Communications* 7.1 (2016), 12471. DOI: 10.1038/ncomms12471.

[72] J Cnossen, T Hinsdale, RØ Thorsen et al. 'Localization Microscopy at Doubled Precision with Patterned Illumination'. In: *Nature Methods* 17.1 (2020), 59–63. DOI: 10.1038/s41592-019-0657-7.

[73] F Balzarotti, Y Eilers, KC Gwosch, AH Gynnå, V Westphal, FD Stefani, J Elf and SW Hell. 'Nanometer Resolution Imaging and Tracking of Fluorescent Molecules with Minimal Photon Fluxes'. In: *Science* 355.6325 (2017), 606–612. DOI: 10.1126/science.aak9913.

[74] F Chen, PW Tillberg and ES Boyden. 'Expansion Microscopy'. In: *Science* 347.6221 (2015), 543–548. DOI: 10.1126/science.1260088.

[75] D Gambarotto, FU Zwettler, M Le Guennec et al. 'Imaging Cellular Ultrastructures Using Expansion Microscopy (U-ExM)'. In: *Nature Methods* 16.1 (2019), 71–74. DOI: 10.1038/s41592-018-0238-1.

[76] FU Zwettler, S Reinhard, D Gambarotto, TDM Bell, V Hamel, P Guichard and M Sauer. 'Molecular Resolution Imaging by Post-Labeling Expansion Single-Molecule Localization Microscopy (Ex-SMLM)'. In: *Nature Communications* 11.1 (2020), 3388. DOI: 10.1038/s41467-020-17086-8.

[77] M Heilemann, S van de Linde, A Mukherjee and M Sauer. 'Super-Resolution Imaging with Small Organic Fluorophores'. In: *Angewandte Chemie International Edition* 48.37 (2009), 6903–6908. DOI: 10.1002/anie.200902073.

[78] M Erdelyi, E Rees, D Metcalf, GSK Schierle, L Dudas, J Sinko, AE Knight and CF Kaminski. 'Correcting Chromatic Offset in Multicolor Super-Resolution Localization Microscopy'. In: *Optics Express* 21.9 (2013), 10978–10988. DOI: 10.1364/OE.21.010978.

[79] M Bates, B Huang, GT Dempsey and X Zhuang. 'Multicolor Super-Resolution Imaging with Photo-Switchable Fluorescent Probes'. In: *Science* 317.5845 (2007), 1749–1753. DOI: 10.1126/science.1146598.

[80] M Bossi, J Fölling, VN Belov et al. 'Multicolor Far-Field Fluorescence Nanoscopy through Isolated Detection of Distinct Molecular Species'. In: *Nano Letters* 8.8 (2008), 2463–2468. DOI: 10.1021/nl801471d.

[81] A Lampe, V Haucke, SJ Sigrist, M Heilemann and J Schmoranzer. 'Multi-Colour Direct STORM with Red Emitting Carbocyanines'. In: *Biology of the Cell* 104.4 (2012), 229–237. DOI: 10.1111/boc.201100011.

[82] Z Zhang, SJ Kenny, M Hauser, W Li and K Xu. 'Ultrahigh-Throughput Single-Molecule Spectroscopy and Spectrally Resolved Super-Resolution Microscopy'. In: *Nature Methods* 12.10 (2015), 935–938. DOI: 10.1038/nmeth.3528.

[83] FR Winter, M Loidolt, V Westphal, AN Butkevich, C Gregor, SJ Sahl and SW Hell. 'Multicolour Nanoscopy of Fixed and Living Cells with a Single STED Beam and Hyperspectral Detection'. In: *Scientific Reports* 7.1 (2017), 46492. DOI: 10.1038/srep46492.

[84] KC Gwosch, JK Pape, F Balzarotti, P Hoess, J Ellenberg, J Ries and SW Hell. 'MINFLUX Nanoscopy Delivers 3D Multicolor Nanometer Resolution in Cells'. In: *Nature Methods* 17.2 (2020), 217–224. DOI: 10.1038/s41592-019-0688-0.

[85] SC Sidenstein, E D'Este, MJ Böhm, JG Danzl, VN Belov and SW Hell. 'Multicolour Multilevel STED Nanoscopy of Actin/Spectrin Organization at Synapses'. In: *Scientific Reports* 6.1 (2016), 26725. DOI: 10.1038/srep26725.

[86] R Jungmann, MS Avendaño, JB Woehrstein, M Dai, WM Shih and P Yin. 'Multiplexed 3D Cellular Super-Resolution Imaging with DNA-PAINT and Exchange-PAINT'. In: *Nature Methods* 11.3 (2014), 313–318. DOI: 10.1038/nmeth.2835.

[87] OK Wade, JB Woehrstein, PC Nickels et al. '124-Color Super-Resolution Imaging by Engineering DNA-PAINT Blinking Kinetics'. In: *Nano Letters* 19.4 (2019), 2641–2646. DOI: 10.1021/acs.nanolett.9b00508.

[88] MA Lauterbach. 'Finding, Defining and Breaking the Diffraction Barrier in Microscopy – a Historical Perspective'. In: *Optical Nanoscopy* 1.1 (2012), 8. DOI: 10.1186/2192-2853-1-8.

[89] B Huang, W Wang, M Bates and X Zhuang. 'Three-Dimensional Super-Resolution Imaging by Stochastic Optical Reconstruction Microscopy'. In: *Science* 319.5864 (2008), 810–813. DOI: 10.1126/science.1153529.

[90] SRP Pavani, MA Thompson, JS Biteen, SJ Lord, N Liu, RJ Twieg, R Piestun and WE Moerner. 'Three-Dimensional, Single-Molecule Fluorescence Imaging beyond the Diffraction Limit by Using a Double-Helix Point Spread Function'. In: *Proceedings of the National Academy of Sciences* 106.9 (2009), 2995–2999. DOI: 10.1073/pnas.0900245106.

[91] Y Shechtman, LE Weiss, AS Backer, SJ Sahl and WE Moerner. 'Precise Three-Dimensional Scan-Free Multiple-Particle Tracking over Large Axial Ranges with Tetrapod Point Spread Functions'. In: *Nano Letters* 15.6 (2015), 4194–4199. DOI: 10.1021/acs.nanolett.5b01396.

[92] P Prabhat, S Ram, ES Ward and RJ Ober. 'Simultaneous Imaging of Different Focal Planes in Fluorescence Microscopy for the Study of Cellular Dynamics in Three Dimensions'. In: *IEEE Transactions on NanoBioscience* 3.4 (2004), 237–242. DOI: 10.1109/TNB.2004.837899.

[93] MF Juette, TJ Gould, MD Lessard, MJ Mlodzianoski, BS Nagpure, BT Bennett, ST Hess and J Bewersdorf. 'Three-Dimensional Sub–100 Nm Resolution Fluorescence Microscopy of Thick Samples'. In: *Nature Methods* 5.6 (2008), 527–529. DOI: 10.1038/nmeth.1211.

[94] A von Diezmann, Y Shechtman and WE Moerner. 'Three-Dimensional Localization of Single Molecules for Super-Resolution Imaging and Single-Particle Tracking'. In: *Chemical Reviews* 117.11 (2017), 7244–7275. DOI: 10.1021/acs.chemrev.6b00629.

[95] P Bon, J Linarès-Loyez, M Feyeux, K Alessandri, B Lounis, P Nassoy and L Cognet. 'Self-Interference 3D Super-Resolution Microscopy for Deep Tissue Investigations'. In: *Nature Methods* 15.6 (2018), 449–454. DOI: 10.1038/s41592-018-0005-3.

[96] G Shtengel, JA Galbraith, CG Galbraith et al. 'Interferometric Fluorescent Super-Resolution Microscopy Resolves 3D Cellular Ultrastructure'. In: *Proceedings of the National Academy of Sciences* 106.9 (2009), 3125–3130. DOI: 10.1073/pnas.0813131106.

[97] D Aquino, A Schönle, C Geisler et al. 'Two-Color Nanoscopy of Three-Dimensional Volumes by 4Pi Detection of Stochastically Switched Fluorophores'. In: *Nature Methods* 8.4 (2011), 353–359. DOI: 10.1038/nmeth.1583.

[98] R Schmidt, CA Wurm, S Jakobs, J Engelhardt, A Egner and SW Hell. 'Spherical Nanosized Focal Spot Unravels the Interior of Cells'. In: *Nature Methods* 5.6 (2008), 539–544. DOI: 10.1038/nmeth.1214.

[99] M Cardoso Dos Santos, R Déturche, C Vézy and R Jaffiol. 'Topography of Cells Revealed by Variable-Angle Total Internal Reflection Fluorescence Microscopy'. In: *Biophysical Journal* 111.6 (2016), 1316–1327. DOI: 10.1016/j.bpj.2016.06.043.

[100] T Ruckstuhl, J Enderlein, S Jung and S Seeger. 'Forbidden Light Detection from Single Molecules'. In: *Analytical Chemistry* 72.9 (2000), 2117–2123. DOI: 10.1021/ac991358k.

[101] J Deschamps, M Mund and J Ries. '3D Superresolution Microscopy by Supercritical Angle Detection'. In: *Optics Express* 22.23 (2014), 29081–29091. DOI: 10.1364/OE.22.029081.

[102] N Bourg, C Mayet, G Dupuis, T Barroca, P Bon, S Lécart, E Fort and S Lévêque-Fort. 'Direct Optical Nanoscopy with Axially Localized Detection'. In: *Nature Photonics* 9.9 (2015), 587–593. DOI: 10.1038/nphoton.2015.132.

[103] TA Klar, S Jakobs, M Dyba, A Egner and SW Hell. 'Fluorescence Microscopy with Diffraction Resolution Barrier Broken by Stimulated Emission'. In: *Proceedings of the National Academy of Sciences* 97.15 (2000), 8206–8210. DOI: 10.1073/pnas.97.15.8206.

[104] T Förster. 'Zwischenmolekulare Energiewanderung und Fluoreszenz'. In: *Annalen der Physik* 437.1-2 (1948), 55–75. DOI: 10.1002/andp.19484370105.

[105] KH Drexhage. 'Influence of a Dielectric Interface on Fluorescence Decay Time'. In: *Journal of Luminescence* 1-2 (1970), 693–701. DOI: 10.1016/0022-2313(70)90082-7.

[106] L Langguth, R Fleury, A Alù and AF Koenderink. 'Drexhage's Experiment for Sound'. In: *Physical Review Letters* 116.22 (2016), 224301. DOI: 10.1103/PhysRevLett.116.224301.

[107] N Karedla. *Single-Molecule Metal-Induced Energy Transfer: From Basics to Applications*. Springer Theses. Springer International Publishing, 2017. ISBN: 978-3-319-60536-4. DOI: 10.1007/978-3-319-60537-1.

[108] DTHW Ruhlandt. 'Modeling Electrodynamics in the Vicinity of Metal Nanostructures'. Doctoral dissertation. Göttingen: Georg-August-Universität Göttingen, 2019. DOI: 11858/00-1735-0000-002E-E5BF-2.

[109] S Isbaner. 'Extending Resolution in All Directions: Image Scanning Microscopy and Metal-Induced Energy Transfer'. Doctoral dissertation. Göttingen: Georg-August-Universität Göttingen, 2019. DOI: 11858/00-1735-0000-002E-E5D6-C.

[110] AI Chizhik, J Rother, I Gregor, A Janshoff and J Enderlein. 'Metal-Induced Energy Transfer for Live Cell Nanoscopy'. In: *Nature Photonics* 8.2 (2014), 124–127. DOI: 10.1038/nphoton.2013.345.

[111] AM Chizhik, C Wollnik, D Ruhlandt et al. 'Dual-Color Metal-Induced and Förster Resonance Energy Transfer for Cell Nanoscopy'. In: *Molecular Biology of the Cell* 29.7 (2018), 846–851. DOI: 10.1091/mbc.E17-05-0314.

[112] N Karedla, AI Chizhik, I Gregor, AM Chizhik, O Schulz and J Enderlein. 'Single-Molecule Metal-Induced Energy Transfer (smMIET): Resolving Nanometer Distances at the Single-Molecule Level'. In: *ChemPhysChem* 15.4 (2014), 705–711. DOI: 10.1002/cphc.201300760.

[113] S Isbaner, N Karedla, I Kaminska et al. 'Axial Colocalization of Single Molecules with Nanometer Accuracy Using Metal-Induced Energy Transfer'. In: *Nano Letters* 18.4 (2018), 2616–2622. DOI: 10.1021/acs.nanolett.8b00425.

[114] A Ghosh, A Sharma, AI Chizhik et al. 'Graphene-Based Metal-Induced Energy Transfer for Sub-Nanometre Optical Localization'. In: *Nature Photonics* 13.12 (2019), 860–865. DOI: 10.1038/s41566-019-0510-7.

[115] I Kaminska, J Bohlen, S Rocchetti, F Selbach, GP Acuna and P Tinnefeld. 'Distance Dependence of Single-Molecule Energy Transfer to Graphene Measured with DNA Origami Nanopositioners'. In: *Nano Letters* 19.7 (2019), 4257–4262. DOI: 10.1021/acs.nanolett.9b00172.

[116] JR Lakowicz, H Cherek, B Maliwal and E Gratton. 'Frequency-Domain Phase-Modulation Fluorometry: Resolution of Complex Decays of Fluorescence Intensity and Anisotropy'. In: *Journal of Luminescence* 31-32 (1984), 699–702. DOI: 10.1016/0022-2313(84)90100-5.

[117] M Wahl, HJ Rahn, I Gregor, R Erdmann and J Enderlein. 'Dead-Time Optimized Time-Correlated Photon Counting Instrument with Synchronized, Independent Timing Channels'. In: *Review of Scientific Instruments* 78.3 (2007), 033106. DOI: 10.1063/1.2715948.

[118] M Maus, M Cotlet, J Hofkens, T Gensch, FC De Schryver, J Schaffer and CAM Seidel. 'An Experimental Comparison of the Maximum Likelihood Estimation and Nonlinear Least-Squares Fluorescence Lifetime Analysis of Single Molecules'. In: *Analytical Chemistry* 73.9 (2001), 2078–2086. DOI: 10.1021/ac000877g.

[119] S Kalinin, A Valeri, M Antonik, S Felekyan and CAM Seidel. 'Detection of Structural Dynamics by FRET: A Photon Distribution and Fluorescence Lifetime Analysis of Systems with Multiple States'. In: *The Journal of Physical Chemistry B* 114.23 (2010), 7983–7995. DOI: 10.1021/jp102156t.

[120] T Nakabayashi and N Ohta. 'Sensing of Intracellular Environments by Fluorescence Lifetime Imaging of Exogenous Fluorophores'. In: *Analytical Sciences* 31.4 (2015), 275–285. DOI: 10.2116/analsci.31.275.

[121] R Datta, TM Heaster, JT Sharick, AA Gillette and MC Skala. 'Fluorescence Lifetime Imaging Microscopy: Fundamentals and Advances in Instrumentation, Analysis, and Applications'. In: *Journal of Biomedical Optics* 25.7 (2020), 071203. DOI: 10.1117/1.JBO.25.7.071203.

[122] M Eigen and R Rigler. 'Sorting Single Molecules: Application to Diagnostics and Evolutionary Biotechnology'. In: *Proceedings of the National Academy of Sciences* 91.13 (1994), 5740–5747. DOI: 10.1073/pnas.91.13.5740.

[123] T Torres and M Levitus. 'Measuring Conformational Dynamics: A New FCS-FRET Approach'. In: *The Journal of Physical Chemistry B* 111.25 (2007), 7392–7400. DOI: 10.1021/jp070659s.

[124] H Neuweiler, A Schulz, M Böhmer, J Enderlein and M Sauer. 'Measurement of Submicrosecond Intramolecular Contact Formation in Peptides at the Single-Molecule Level'. In: *Journal of the American Chemical Society* 125.18 (2003), 5324–5330. DOI: 10.1021/ja034040p.

[125] D Magde, WW Webb and EL Elson. 'Fluorescence Correlation Spectroscopy. III. Uniform Translation and Laminar Flow'. In: *Biopolymers* 17.2 (1978), 361–376. DOI: 10.1002/bip.1978.360170208.

[126] H Bi, Y Yin, B Pan, G Li and XS Zhao. 'Scanning Single-Molecule Fluorescence Correlation Spectroscopy Enables Kinetics Study of DNA Hairpin Folding with a Time Window from Microseconds to Seconds'. In: *The Journal of Physical Chemistry Letters* 7.10 (2016), 1865–1871. DOI: 10.1021/acs.jpclett.6b00720.

[127] J Schnitzbauer, MT Strauss, T Schlichthaerle, F Schueder and R Jungmann. 'Super-Resolution Microscopy with DNA-PAINT'. In: *Nature Protocols* 12.6 (2017), 1198–1228. DOI: 10.1038/nprot.2017.024.

[128] F Schueder, J Lara-Gutiérrez, BJ Beliveau et al. 'Multiplexed 3D Super-Resolution Imaging of Whole Cells Using Spinning Disk Confocal Microscopy and DNA-PAINT'. In: *Nature Communications* 8.1 (2017), 2090. DOI: 10.1038/s41467-017-02028-8.

[129] J Lee, Y Miyanaga, M Ueda and S Hohng. 'Video-Rate Confocal Microscopy for Single-Molecule Imaging in Live Cells and Superresolution Fluorescence Imaging'. In: *Biophysical Journal* 103.8 (2012), 1691–1697. DOI: 10.1016/j.bpj.2012.09.014.

[130] W Vandenberg, M Leutenegger, T Lasser, J Hofkens and P Dedecker. 'Diffraction-Unlimited Imaging: From Pretty Pictures to Hard Numbers'. In: *Cell and Tissue Research* 360.1 (2015), 151–178. DOI: 10.1007/s00441-014-2109-0.

[131] D Llères, AP Bailly, A Perrin, DG Norman, DP Xirodimas and R Feil. 'Quantitative FLIM-FRET Microscopy to Monitor Nanoscale Chromatin Compaction In Vivo Reveals Structural Roles of Condensin Complexes'. In: *Cell Reports* 18.7 (2017), 1791–1803. DOI: 10.1016/j.celrep.2017.01.043.

[132] AJ Bowman, BB Klopfer, T Juffmann and MA Kasevich. 'Electro-Optic Imaging Enables Efficient Wide-Field Fluorescence Lifetime Microscopy'. In: *Nature Communications* 10.1 (2019), 4561. DOI: 10.1038/s41467-019-12535-5.

[133] N Oleksiievets, JC Thiele, A Weber, I Gregor, O Nevskyi, S Isbaner, R Tsukanov and J Enderlein. 'Wide-Field Fluorescence Lifetime Imaging of Single Molecules'. In: *The Journal of Physical Chemistry A* 124.17 (2020), 3494–3500. DOI: 10.1021/acs.jpca.0c01513.

[134] M Zhao, Y Li and L Peng. 'Parallel Excitation-Emission Multiplexed Fluorescence Lifetime Confocal Microscopy for Live Cell Imaging'. In: *Optics Express* 22.9 (2014), 10221–10232. DOI: 10.1364/OE.22.010221.

[135] M Sauer and M Heilemann. 'Single-Molecule Localization Microscopy in Eukaryotes'. In: *Chemical Reviews* 117.11 (2017), 7478–7509. DOI: 10.1021/acs.chemrev.6b00667.

[136] E Hershko, LE Weiss, T Michaeli and Y Shechtman. 'Multicolor Localization Microscopy and Point-Spread-Function Engineering by Deep Learning'. In: *Optics Express* 27.5 (2019), 6158–6183. DOI: 10.1364/OE.27.006158.

[137] PA Gómez-García, ET Garbacik, JJ Otterstrom, MF Garcia-Parajo and M Lakadamyali. 'Excitation-Multiplexed Multicolor Superresolution Imaging with Fm-STORM and Fm-DNA-PAINT'. In: *Proceedings of the National Academy of Sciences* 115.51 (2018), 12991–12996. DOI: 10.1073/pnas.1804725115.

[138] M Ovesný, P Křížek, J Borkovec, Z Švindrych and GM Hagen. 'ThunderSTORM: A Comprehensive ImageJ Plug-in for PALM and STORM Data Analysis and Super-Resolution Imaging'. In: *Bioinformatics* 30.16 (2014), 2389–2390. DOI: 10.1093/bioinformatics/btu202.

[139] T Schlichthaerle, AS Eklund, F Schueder et al. 'Site-Specific Labeling of Affimers for DNA-PAINT Microscopy'. In: *Angewandte Chemie International Edition* 57.34 (2018), 11060–11063. DOI: 10.1002/anie.201804020.

[140] S Sograte-Idrissi, N Oleksiievets, S Isbaner, M Eggert-Martinez, J Enderlein, R Tsukanov and F Opazo. 'Nanobody Detection of Standard Fluorescent Proteins Enables Multi-Target DNA-PAINT with High Resolution and Minimal Displacement Errors'. In: *Cells* 8.1 (2019), 48. DOI: 10.3390/cells8010048.

[141] SC Stein and J Thiart. 'TrackNTrace: A Simple and Extendable Open-Source Framework for Developing Single-Molecule Localization and Tracking Algorithms'. In: *Scientific Reports* 6.1 (2016), 37947. DOI: 10.1038/srep37947.

[142] 'Statistical Models and Inference'. In: *Practical Bayesian Inference: A Primer for Physical Scientists*. Ed. by CAL Bailer-Jones. Cambridge: Cambridge University Press, 2017, 55–75. ISBN: 978-1-107-19211-9. DOI: 10.1017/9781108123891.004.

[143] Y Wang, J Schnitzbauer, Z Hu, X Li, Y Cheng, ZL Huang and B Huang. 'Localization Events-Based Sample Drift Correction for Localization Microscopy with Redundant Cross-Correlation Algorithm'. In: *Optics Express* 22.13 (2014), 15982–15991. DOI: 10.1364/OE.22.015982.

[144] GT Dempsey, JC Vaughan, KH Chen, M Bates and X Zhuang. 'Evaluation of Fluorophores for Optimal Performance in Localization-Based Super-Resolution Imaging'. In: *Nature Methods* 8.12 (2011), 1027–1036. DOI: 10.1038/nmeth.1768.

[145] T Niehörster, A Löschberger, I Gregor et al. 'Multi-Target Spectrally Resolved Fluorescence Lifetime Imaging Microscopy'. In: *Nature Methods* 13.3 (2016), 257–262. DOI: 10.1038/nmeth.3740.

[146] S Culley, D Albrecht, C Jacobs, PM Pereira, C Leterrier, J Mercer and R Henriques. 'Quantitative Mapping and Minimization of Super-Resolution Optical Imaging Artifacts'. In: *Nature Methods* 15.4 (2018), 263–266. DOI: 10.1038/nmeth.4605.

[147] T Quan, S Zeng and Z Huang. 'Localization Capability and Limitation of Electron-Multiplying Charge-Coupled, Scientific Complementary Metal-Oxide Semiconductor, and Charge-Coupled Devices for Superresolution Imaging'. In: *Journal of Biomedical Optics* 15.6 (2010), 066005. DOI: 10.1117/1.3505017.

[148] J Vogelsang, T Cordes and P Tinnefeld. 'Single-Molecule Photophysics of Oxazines on DNA and Its Application in a FRET Switch'. In: *Photochemical & Photobiological Sciences* 8.4 (2009), 486–496. DOI: 10.1039/B822318C.

[149] K Klehs, C Spahn, U Endesfelder, SF Lee, A Fürstenberg and M Heilemann. 'Increasing the Brightness of Cyanine Fluorophores for Single-Molecule and Superresolution Imaging'. In: *ChemPhysChem* 15.4 (2014), 637–641. DOI: 10.1002/cphc.201300874.

[150] SF Lee, Q Vérolet and A Fürstenberg. 'Improved Super-Resolution Microscopy with Oxazine Fluorophores in Heavy Water'. In: *Angewandte Chemie International Edition* 52.34 (2013), 8948–8951. DOI: 10.1002/anie.201302341.

[151] V Buschmann, KD Weston and M Sauer. 'Spectroscopic Study and Evaluation of Red-Absorbing Fluorescent Dyes'. In: *Bioconjugate Chemistry* 14.1 (2003), 195–204. DOI: 10.1021/bc025600x.

[152] NS Deußner-Helfmann, A Auer, MT Strauss, S Malkusch, MS Dietz, HD Barth, R Jungmann and M Heilemann. 'Correlative Single-Molecule FRET and DNA-PAINT Imaging'. In: *Nano Letters* 18.7 (2018), 4626–4630. DOI: 10.1021/acs.nanolett.8b02185.

[153] TWJ Gadella, TM Jovin and RM Clegg. 'Fluorescence Lifetime Imaging Microscopy (FLIM): Spatial Resolution of Microstructures on the Nanosecond Time Scale'. In: *Biophysical Chemistry* 48.2 (1993), 221–239. DOI: 10.1016/0301-4622(93)85012-7.

[154] EB van Munster and TWJ Gadella. 'Fluorescence Lifetime Imaging Microscopy (FLIM)'. In: *Microscopy Techniques*. Ed. by J Rietdorf. Advances in Biochemical Engineering. Berlin, Heidelberg: Springer, 2005, 143–175. ISBN: 978-3-540-31545-2. DOI: 10.1007/b102213.

[155] A Periasmay and RN Day, eds. *Molecular Imaging*. Methods in Physiology. Oxford ; New York: Oxford University Press, 2005. 312 pp. ISBN: 978-0-19-517720-6. DOI: 10.1016/B978-0-19-517720-6.X5006-8.

[156] AK Woźniak, GF Schröder, H Grubmüller, CAM Seidel and F Oesterhelt. 'Single-Molecule FRET Measures Bends and Kinks in DNA'. In: *Proceedings of the National Academy of Sciences* 105.47 (2008), 18337–18342. DOI: 10.1073/pnas.0800977105.

[157] DV O'Connor and D Phillips. *Time-Correlated Single Photon Counting*. London: Academic Press, 1984. 298 pp. ISBN: 978-0-12-524140-3. DOI: 10.1016/B978-0-12-524140-3.X5001-1.

[158] CY Dong, T French, PTC So, C Buehler, KM Berland and E Gratton. 'Fluorescence-Lifetime Imaging Techniques for Microscopy'. In: *Methods in Cell Biology*. Ed. by L Wilson and P Matsudaira. Vol. 72. Academic Press, 2003, 431–464. DOI: 10.1016/S0091-679X(03)72021-4.

[159] H Chen, G Holst and E Gratton. 'Modulated CMOS Camera for Fluorescence Lifetime Microscopy'. In: *Microscopy Research and Technique* 78.12 (2015), 1075–1081. DOI: 10.1002/jemt.22587.

[160] C Niclass, C Favi, T Kluter, M Gersbach and E Charbon. 'A 128×128 Single-Photon Image Sensor With Column-Level 10-Bit Time-to-Digital Converter Array'. In: *IEEE Journal of Solid-State Circuits* 43.12 (2008), 2977–2989. DOI: 10.1109/JSSC.2008.2006445.

[161] C Veerappan, J Richardson, R Walker et al. 'A 160×128 Single-Photon Image Sensor with on-Pixel 55ps 10b Time-to-Digital Converter'. In: *2011 IEEE International Solid-State Circuits Conference*. 2011 IEEE International Solid-State Circuits Conference. 2011, 312–314. DOI: 10.1109/ISSCC.2011.5746333.

[162] H Sparks, F Görlitz, DJ Kelly et al. 'Characterisation of New Gated Optical Image Intensifiers for Fluorescence Lifetime Imaging'. In: *Review of Scientific Instruments* 88.1 (2017), 013707. DOI: 10.1063/1.4973917.

[163] X Michalet, OHW Siegmund, JV Vallerga, P Jelinsky, JE Millaud and S Weiss. 'Photon-Counting H33D Detector for Biological Fluorescence Imaging'. In: *Nuclear Instruments and Methods in Physics Research Section A: Accelerators, Spectrometers, Detectors and Associated Equipment*. Proceedings of the 4th International Conference on New Developments in Photodetection 567.1 (2006), 133–136. DOI: 10.1016/j.nima.2006.05.155.

[164] Y Prokazov, E Turbin, A Weber, R Hartig and W Zuschratter. 'Position Sensitive Detector for Fluorescence Lifetime Imaging'. In: *Journal of Instrumentation* 9.12 (2014), C12015–C12015. DOI: 10.1088/1748-0221/9/12/C12015.

[165] A Ulku, A Ardelean, M Antolovic, S Weiss, E Charbon, C Bruschini and X Michalet. 'Wide-Field Time-Gated SPAD Imager for Phasor-Based FLIM Applications'. In: *Methods and Applications in Fluorescence* 8.2 (2020), 024002. DOI: 10.1088/2050-6120/ab6ed7.

[166] R Hartig, Y Prokazov, E Turbin and W Zuschratter. 'Wide-Field Fluorescence Lifetime Imaging with Multi-Anode Detectors'. In: *Fluorescence Spectroscopy and Microscopy: Methods and Protocols*. Ed. by Y Engelborghs and AJ Visser. Methods in Molecular Biology. Totowa, NJ: Humana Press, 2014, 457–480. ISBN: 978-1-62703-649-8. DOI: 10.1007/978-1-62703-649-8_20.

[167] Photonscore. *LINCam*. 2019. URL: https://www.photonscore.de/lincam (visited on 14/09/2020).

[168] ThermoFisher. *Cy5 dye*. URL: https://www.thermofisher.com/de/de/home/life-science/cell-analysis/fluorophores/cy5-dye.html (visited on 11/09/2020).

[169] ATTO-TEC. *ATTO 655*. URL: https://www.atto-tec.com/product_info.php?info=p115_atto-655.html (visited on 11/09/2020).

[170] ATTO-TEC. *ATTO 647N*. URL: https://www.atto-tec.com/product_info.php?info=p114_atto-647n.html (visited on 11/09/2020).

[171] T Baronsky, D Ruhlandt, BR Brückner et al. 'Cell–Substrate Dynamics of the Epithelial-to-Mesenchymal Transition'. In: *Nano Letters* 17.5 (2017), 3320–3326. DOI: 10.1021/acs.nanolett.7b01558.

[172] AM Chizhik, D Ruhlandt, J Pfaff, N Karedla, AI Chizhik, I Gregor, RH Kehlenbach and J Enderlein. 'Three-Dimensional Reconstruction of Nuclear Envelope Architecture Using Dual-Color Metal-Induced Energy Transfer Imaging'. In: *ACS Nano* 11.12 (2017), 11839–11846. DOI: 10.1021/acsnano.7b04671.

[173] I Gregor, A Chizhik, N Karedla and J Enderlein. 'Metal-Induced Energy Transfer'. In: *Nanophotonics* 8.10 (2019), 1689–1699. DOI: 10.1515/nanoph-2019-0201.

[174] M Heilemann, DP Herten, R Heintzmann et al. 'High-Resolution Colocalization of Single Dye Molecules by Fluorescence Lifetime Imaging Microscopy'. In: *Analytical Chemistry* 74.14 (2002), 3511–3517. DOI: 10.1021/ac025576g.

[175] J Enderlein, DL Robbins, WP Ambrose and RA Keller. 'Molecular Shot Noise, Burst Size Distribution, and Single-Molecule Detection in Fluid Flow: Effects of Multiple Occupancy'. In: *The Journal of Physical Chemistry A* 102.30 (1998), 6089–6094. DOI: 10.1021/jp9708299.

[176] J Vogelsang, T Cordes, C Forthmann, C Steinhauer and P Tinnefeld. 'Controlling the Fluorescence of Ordinary Oxazine Dyes for Single-Molecule Switching and Superresolution Microscopy'. In: *Proceedings of the National Academy of Sciences* 106.20 (2009), 8107–8112. DOI: 10.1073/pnas.0811875106.

[177] A Ghosh, S Isbaner, M Veiga-Gutiérrez, I Gregor, J Enderlein and N Karedla. 'Quantifying Microsecond Transition Times Using Fluorescence Lifetime Correlation Spectroscopy'. In: *The Journal of Physical Chemistry Letters* 8.24 (2017), 6022–6028. DOI: 10.1021/acs.jpclett.7b02707.

[178] D Sage, H Kirshner, T Pengo, N Stuurman, J Min, S Manley and M Unser. 'Quantitative Evaluation of Software Packages for Single-Molecule Localization Microscopy'. In: *Nature Methods* 12.8 (2015), 717–724. DOI: 10.1038/nmeth.3442.

[179] P Kovesi. *Good Colour Maps: How to Design Them*. 2015. arXiv: 1509.03700 [cs]. URL: http://arxiv.org/abs/1509.03700 (visited on 30/09/2020).

[180] M Wahl and S Orthaus-Müller. *Time Tagged Time-Resolved Fluorescence Data Collection in Life Sciences*. Technical Note. PicoQuant, 2014, 10.

[181] Photonscore. *Photonscore Toolbox*. 2019. URL: https://www.photonscore.de/docs/matlab/ (visited on 02/10/2020).

[182] A Elmokadem and J Yu. 'Optimal Drift Correction for Superresolution Localization Microscopy with Bayesian Inference'. In: *Biophysical Journal* 109.9 (2015), 1772–1780. DOI: 10.1016/j.bpj.2015.09.017.

[183] J Ries. 'SMAP: A Modular Super-Resolution Microscopy Analysis Platform for SMLM Data'. In: *Nature Methods* 17.9 (2020), 870–872. DOI: 10.1038/s41592-020-0938-1.

[184] S Shah, A Dubey and J Reif. 'ExTemp: A Computational and Image-Processing Suite for Extracting Temporal Barcodes'. In: *Journal of Open Source Software* 5.46 (2020), 2026. DOI: 10.21105/joss.02026.

[185] D Gao, PR Barber, JV Chacko, MAK Sagar, CT Rueden, AR Grislis, MC Hiner and KW Eliceiri. 'FLIMJ: An Open-Source ImageJ Toolkit for Fluorescence Lifetime Image Data Analysis'. In: *bioRxiv* (2020), 2020.08.17.253625. DOI: 10.1101/2020.08.17.253625.

[186] S Weinbaum, JM Tarbell and ER Damiano. 'The Structure and Function of the Endothelial Glycocalyx Layer'. In: *Annual Review of Biomedical Engineering* 9.1 (2007), 121–167. DOI: 10.1146/annurev.bioeng.9.060906.151959.

[187] JR Blake and MA Sleigh. 'Mechanics of Ciliary Locomotion'. In: *Biological Reviews* 49.1 (1974), 85–125. DOI: 10.1111/j.1469-185x.1974.tb01299.x.

[188] N Srinivasan, M Bhagawati, B Ananthanarayanan and S Kumar. 'Stimuli-Sensitive Intrinsically Disordered Protein Brushes'. In: *Nature Communications* 5.1 (2014), 5145. DOI: 10.1038/ncomms6145.

[189] L Ionov, S Minko, M Stamm, JF Gohy, R Jérôme and A Scholl. 'Reversible Chemical Patterning on Stimuli-Responsive Polymer Film: Environment-Responsive Lithography'. In: *Journal of the American Chemical Society* 125.27 (2003), 8302–8306. DOI: 10.1021/ja035560n.

[190] C Pastorino and M Müller. 'Mixed Brush of Chemically and Physically Adsorbed Polymers under Shear: Inverse Transport of the Physisorbed Species'. In: *The Journal of Chemical Physics* 140.1 (2014), 014901. DOI: 10.1063/1.4851195.

[191] D Bartolo, G Degré, P Nghe and V Studer. 'Microfluidic Stickers'. In: *Lab on a Chip* 8.2 (2008), 274–279. DOI: 10.1039/B712368J.

[192] LA Chrisey, GU Lee and CE O'Ferrall. 'Covalent Attachment of Synthetic DNA to Self-Assembled Monolayer Films'. In: *Nucleic Acids Research* 24.15 (1996), 3031–3039. DOI: 10.1093/nar/24.15.3031.

[193] SJ Oh, SJ Cho, CO Kim and JW Park. 'Characteristics of DNA Microarrays Fabricated on Various Aminosilane Layers'. In: *Langmuir* 18.5 (2002), 1764–1769. DOI: 10.1021/la0113522.

[194] K Hendrich. 'Smart RAFT-Polymer Surfaces: Exploring Their Self-Assembly and Dynamics on the Nanoscale'. Doctoral dissertation. Göttingen: Georg-August-Universität Göttingen, 2020. DOI: 21.11130/00-1735-0000-0005-134A-3.

[195] LE Peterson. 'PIRLS: Poisson Iteratively Reweighted Least Squares Computer Program for Additive, Multiplicative, Power, and Non-Linear Models'. In: *Journal of Statistical Software* 2.1 (1997), 1–28. DOI: 10.18637/jss.v002.i05.

[196] M Wahl, I Gregor, M Patting and J Enderlein. 'Fast Calculation of Fluorescence Correlation Data with Asynchronous Time-Correlated Single-Photon Counting'. In: *Optics Express* 11.26 (2003), 3583–3591. DOI: 10.1364/OE.11.003583.

[197] K Spaeth, A Brecht and G Gauglitz. 'Studies on the Biotin–Avidin Multilayer Adsorption by Spectroscopic Ellipsometry'. In: *Journal of Colloid and Interface Science* 196.2 (1997), 128–135. DOI: 10.1006/jcis.1997.5200.

[198] S Mühle. 'Nanoscale Brownian Dynamics of Semiflexible Biopolymers'. Doctoral dissertation. Göttingen: Georg-August-Universität Göttingen, 2020. DOI: 21.11130/00-1735-0000-0005-1433-B.

[199] D Basler, W Leis, B Görlach, AJ Meixner and F Schleifenbaum. 'How Molecular Mechanics Can Measure Nanoscopic Flow'. In: *The Journal of Physical Chemistry C* 116.27 (2012), 14694–14700. DOI: 10.1021/jp3037654.

[200] ST Milner. 'Strongly Stretched Polymer Brushes'. In: *Journal of Polymer Science Part B: Polymer Physics* 32.16 (1994), 2743–2755. DOI: 10.1002/polb.1994.090321620.

[201] M Thomas, M Gajda, C Amiri Naini, S Franzka, M Ulbricht and N Hartmann. 'Poly(N,N-Dimethylaminoethyl Methacrylate) Brushes: pH-Dependent Switching Kinetics of a Surface-Grafted Thermoresponsive Polyelectrolyte'. In: *Langmuir* 31.49 (2015), 13426–13432. DOI: 10.1021/acs.langmuir.5b03448.

[202] D Erickson. 'Towards Numerical Prototyping of Labs-on-Chip: Modeling for Integrated Microfluidic Devices'. In: *Microfluidics and Nanofluidics* 1.4 (2005), 301–318. DOI: 10.1007/s10404-005-0041-z.

[203] N Karedla, JC Thiele, I Gregor and J Enderlein. 'Efficient Solver for a Special Class of Convection-Diffusion Problems'. In: *Physics of Fluids* 31.2 (2019), 023606. DOI: 10.1063/1.5079965.

[204] H Bruus. *Theoretical Microfluidics*. Oxford Master Series in Physics 18. Oxford ; New York: Oxford University Press, 2008. 346 pp. ISBN: 978-0-19-923508-7.

[205] CB Moler. 'Finite Difference Methods'. In: *Numerical Computing with MATLAB*. Revised reprint. Philadelphia, Pa: Society for Industrial & Applied Mathematics, 2011. ISBN: 978-0-89871-660-3.

[206] PA Markowich. *Applied Partial Differential Equations: A Visual Approach*. Berlin ; New York: Springer, 2007. 206 pp. ISBN: 978-3-540-34645-6.

[207] JC Thiele, I Gregor, N Karedla and J Enderlein. 'Efficient Modeling of Three-Dimensional Convection–Diffusion Problems in Stationary Flows'. In: *Physics of Fluids* 32.11 (2020), 112015. DOI: 10.1063/5.0024190.

[208] W Liu and G Haller. 'Strange Eigenmodes and Decay of Variance in the Mixing of Diffusive Tracers'. In: *Physica D: Nonlinear Phenomena* 188.1 (2004), 1–39. DOI: 10.1016/S0167-2789(03)00287-2.

[209] B Wunderlich, D Nettels and B Schuler. 'Taylor Dispersion and the Position-to-Time Conversion in Microfluidic Mixing Devices'. In: *Lab on a Chip* 14.1 (2013), 219–228. DOI: 10.1039/C3LC51002F.

[210] M Gösch, H Blom, J Holm, T Heino and R Rigler. 'Hydrodynamic Flow Profiling in Microchannel Structures by Single Molecule Fluorescence Correlation Spectroscopy'. In: *Analytical Chemistry* 72.14 (2000), 3260–3265. DOI: 10.1021/ac991448p.

[211] TJ Arbour and J Enderlein. 'Application of Dual-Focus Fluorescence Correlation Spectroscopy to Microfluidic Flow-Velocity Measurement'. In: *Lab on a Chip* 10.10 (2010), 1286–1292. DOI: 10.1039/B924594D.

[212] D Schäffel, K Koynov, D Vollmer, HJ Butt and C Schönecker. 'Local Flow Field and Slip Length of Superhydrophobic Surfaces'. In: *Physical Review Letters* 116.13 (2016), 134501. DOI: 10.1103/PhysRevLett.116.134501.

[213] L Lanotte, S Guido, C Misbah, P Peyla and L Bureau. 'Flow Reduction in Microchannels Coated with a Polymer Brush'. In: *Langmuir* 28.38 (2012), 13758–13764. DOI: 10.1021/la302171a.

[214] V Müller and F Westerlund. 'Optical DNA Mapping in Nanofluidic Devices: Principles and Applications'. In: *Lab on a Chip* 17.4 (2017), 579–590. DOI: 10.1039/C6LC01439A.

[215] HP Spielmann, DE Wemmer and JP Jacobsen. 'Solution Structure of a DNA Complex with the Fluorescent Bis-Intercalator TOTO Determined by NMR Spectroscopy'. In: *Biochemistry* 34.27 (1995), 8542–8553. DOI: 10.1021/bi00027a004.

[216] EF Pettersen, TD Goddard, CC Huang, GS Couch, DM Greenblatt, EC Meng and TE Ferrin. 'UCSF Chimera—A Visualization System for Exploratory Research and Analysis'. In: *Journal of Computational Chemistry* 25.13 (2004), 1605–1612. DOI: 10.1002/jcc.20084.

[217] W Reisner, NB Larsen, A Silahtaroglu, A Kristensen, N Tommerup, JO Tegenfeldt and H Flyvbjerg. 'Single-Molecule Denaturation Mapping of DNA in Nanofluidic Channels'. In: *Proceedings of the National Academy of Sciences* 107.30 (2010), 13294–13299. DOI: 10.1073/pnas.1007081107.

[218] AN Nilsson, G Emilsson, LK Nyberg et al. 'Competitive Binding-Based Optical DNA Mapping for Fast Identification of Bacteria - Multi-Ligand Transfer Matrix Theory and Experimental Applications on Escherichia Coli'. In: *Nucleic Acids Research* 42.15 (2014), e118–e118. DOI: 10.1093/nar/gku556.

[219] BP Bowen, J Enderlein and NW Woodbury. 'Single-Molecule Fluorescence Spectroscopy of TOTO on Poly-AT and Poly-GC DNA'. In: *Photochemistry and Photobiology* 78.6 (2003), 576–581. DOI: 10.1562/0031-8655(2003)0780576sfsoto2.0.co2.

[220] PF Østergaard, M Matteucci, W Reisner and R Taboryski. 'DNA Barcoding via Counterstaining with AT/GC Sensitive Ligands in Injection-Molded All-Polymer Nanochannel Devices'. In: *Analyst* 138.4 (2013), 1249–1255. DOI: 10.1039/C2AN36522G.

LIST OF ACRONYMS

CCD	charge-coupled device
CLSM	confocal laser-scanning microscopy
DNA	deoxyribonucleic acid
dSTORM	direct stochastic optical reconstruction microscopy
emCCD	electron-multiplying CCD
FCS	fluorescence correlation spectroscopy
FL-SMLM	fluorescence-lifetime SMLM
FLIM	fluorescence-lifetime imaging microscopy
FRC	Fourier ring correlation
FRET	Förster resonance energy transfer
FWHM	full width at half maximum
GLOX	oxygen scavenger buffer based on glucose oxidase
GUI	graphical user interface
IRF	instrument response function
ISM	image scanning microscopy
MCP	micro-channel plates
MEA	β-mercaptoethylamine
MIET	metal-induced energy transfer
MINFLUX	no acronym, but expresses concept to minimise photon flux
MLE	maximum likelihood estimator
NSOM	near-field scanning optical microscopy
PAINT	points accumulation for imaging in nanoscale topography
PALM	photoactivated localisation microscopy
PDMAEMA	poly 2-(dimethylamino)ethyl methacrylate
PDMS	polydimethylsiloxane
PET	photoinduced electron transfer
PIRLS	Poisson iteratively reweighted least squares
PSF	point spread function

QY	quantum yield
RCC	redundant cross-correlation
SAF	supercritical angle fluorescence
SIM	structured illumination microscopy
SMLM	single-molecule localisation microscopy
SOFI	super-resolution optical fluctuation imaging
SPAD	single-photon avalanche-diode
SRRF	super-resolution radial fluctuations
STED	stimulated emission depletion
STORM	stochastic optical reconstruction microscopy
TCSPC	time-correlated single-photon counting
TIR	total internal reflection

ACKNOWLEDGEMENTS

None of the work presented in this thesis would have been possible without the generous support of numerous people.

First of all, I want to thank Jörg Enderlein, not only for the supervision and guidance, but even more for the confidence and freedom he granted. This created the most motivating and enjoyable work environment. Our discussions always encouraged me not to seek the easiest but the best solution.

I would like to thank my thesis committee, Prof. Thomas Burg and Prof. Marcus Müller, for their valuable input, their time for discussions, and for being approachable. Their encouragement made it easier to move on when experiments kept failing.

I am grateful for our collaboration with Markus Sauer and his group, which still keeps pushing the limits of our techniques, and I am amazed by Domininc's sample preparation (and packaging) skills. Even tough we have never met in person, I always enjoyed the discussions and virtual meetings.

I would like to thank Katharina for her meticulous preparation of countless polymer brush samples, and her contagious enthusiasm. I would also like to thank Marcus Müller and Claudio Pastorino for the discussion of the polymer brush experiments, and sharing their theoretical insights.

I am grateful to Sebastian, Narain, and Arindam for introducing me into the world of single molecules and sharing their expertise. I thank Roman, Nazar, and especially Oleksii for the productive collaboration in the lab, stimulating discussions and endless data analysis challenges.

Everyone in the Enderlein group has been very supportive and welcoming. Many thanks to all my former and present colleagues: Aditya, Akshita, Alexey, Anna, Arindam, Daja, Hongje, Ingo, Jan, Narain, Nazar, Niels, Oleksii, Roman, Sebastian, Shun, Simon, Soheil, Steffen, Subhabrata, and Tao. The fruitful discussions, joint breaks, and their suggestions and support created a extraordinary and productive atmosphere.

I thank Thomas Geiling and Regina Wunderlich for the IT and administrative support.

I thank Antje Erdmann and Frauke Bergmann from the IMRPS-PBCS office for a smooth organisation, answering countless questions, and the good cooperation during my time as student representative.

I want to thank my family, especially my parents, for their continuos support and encouragement throughout my entire education.

Last but not least, I am incredibly thankful to (the only) Anna for critical proof-reading, endless discussions, patience, support, and so much more.